# NAVAL POSTGRADUATE SCHOOL
# Monterey, California

# THESIS

**SEASONAL VARIABILITY OF EXTRATROPICAL NORTH PACIFIC WIND STRESS, EKMAN PUMPING AND SVERDRUP TRANSPORT**

by

Christopher S. Moore

December 2001

| | |
|---|---|
| Thesis Advisor: | Curtis A. Collins |
| Co-Advisor: | Frank B. Schwing |

**Approved for public release; distribution is unlimited**

THIS PAGE INTENTIONALLY LEFT BLANK

| REPORT DOCUMENTATION PAGE | Form Approved OMB No. 0704-0188 |
|---|---|

Public reporting burden for this collection of information is estimated to average 1 hour per response, including the time for reviewing instruction, searching existing data sources, gathering and maintaining the data needed, and completing and reviewing the collection of information. Send comments regarding this burden estimate or any other aspect of this collection of information, including suggestions for reducing this burden, to Washington headquarters Services, Directorate for Information Operations and Reports, 1215 Jefferson Davis Highway, Suite 1204, Arlington, VA 22202-4302, and to the Office of Management and Budget, Paperwork Reduction Project (0704-0188) Washington DC 20503.

| 1. AGENCY USE ONLY *(Leave blank)* | 2. REPORT DATE<br>December 2001 | 3. REPORT TYPE AND DATES COVERED<br>Master's Thesis |
|---|---|---|

| | |
|---|---|
| **4. TITLE AND SUBTITLE**: Seasonal Variability of Extratropical North Pacific Wind Stress, Ekman Pumping and Sverdrup Transport | **5. FUNDING NUMBERS** |
| **6. AUTHOR(S)** Christopher S. Moore | |
| **7. PERFORMING ORGANIZATION NAME(S) AND ADDRESS(ES)**<br>Naval Postgraduate School<br>Monterey, CA 93943-5000 | **8. PERFORMING ORGANIZATION REPORT NUMBER** |
| **9. SPONSORING /MONITORING AGENCY NAME(S) AND ADDRESS(ES)**<br>National Oceanic and Atmospheric Administration<br>National Marine Fisheries Service/Pacific Fisheries Environmental Laboratory<br>1352 Lighthouse Avenue<br>Pacific Grove, CA 93950-2097<br><br>National Oceanic and Atmospheric Administration<br>National Marine Fisheries Service/Santa Cruz Laboratory<br>110 Shaffer Road<br>Santa Cruz, CA 95060 | **10. SPONSORING/MONITORING AGENCY REPORT NUMBER** |

**11. SUPPLEMENTARY NOTES** The views expressed in this thesis are those of the author and do not reflect the official policy or position of the Department of Defense or the U.S. Government.

| 12a. DISTRIBUTION / AVAILABILITY STATEMENT | 12b. DISTRIBUTION CODE |
|---|---|
| Approved for public release; distribution is unlimited | |

**13. ABSTRACT *(maximum 200 words)***

The annual cycle of the North Pacific wind stress, Ekman pumping and Sverdrup transport is investigated by means of empirical orthogonal function (EOF) analysis techniques. Fifty-two years of National Centers for Environmental Prediction (NCEP, formerly "NMC") and the National Center for Atmospheric Research (NCAR) Reanalysis daily averaged surface wind components covering the extratropical North Pacific are used to calculate daily averaged wind stress components. These wind stress components are averaged to 624 monthly mean fields from which monthly mean Ekman pumping and Sverdrup transport fields are derived. Each data field has the long-term annual mean and linear trend removed at each grid point before EOF analysis. The first three modes are considered to be physically significant based on the plot of the log eigenvalue against its root. The first principal components of each field are highly coherent, have most of their spectral energy at the annual cycle, and are nearly in phase. The second mode of these fields show significant spectral energy at the semiannual cycle. The third mode has more complex spatial variability than the first and second mode. The annual cycle is best described by the first EOF mode which is composed of two seasons (winter and summer) that last for five months each separated by two rapid (approximately one month) transition periods (spring and fall). The annual cycle is complex and certain geographical regions are seasonal "hot spots" that add to the complexity. Relationships are derived between the various modes to help explain seasonal movement of the Ekman pumping zero isotach and seasonal variations in Sverdrup transport. The annual variability can reasonably be described using only the first three EOF modes.

| 14. SUBJECT TERMS | 15. NUMBER OF PAGES |
|---|---|
| North Pacific Wind Stress, Ekman Pumping, Sverdrup Transport, Empirical Orthogonal Function (EOF), Isotach and Seasonal Variations | 117 |
| | 16. PRICE CODE |

| 17. SECURITY CLASSIFICATION OF REPORT | 18. SECURITY CLASSIFICATION OF THIS PAGE | 19. SECURITY CLASSIFICATION OF ABSTRACT | 20. LIMITATION OF ABSTRACT |
|---|---|---|---|
| Unclassified | Unclassified | Unclassified | UL |

NSN 7540-01-280-5500

Standard Form 298 (Rev. 2-89)
Prescribed by ANSI Std. 239-18

THIS PAGE INTENTIONALLY LEFT BLANK

**Approved for public release; distribution is unlimited**

# SEASONAL VARIABILITY OF EXTRATROPICAL NORTH PACIFIC WIND STRESS, EKMAN PUMPING AND SVERDRUP TRANSPORT

Christopher S. Moore
LCDR, National Oceanic and Atmospheric Administration
B.S., Virginia Tech, 1983

Submitted in partial fulfillment of the
requirements for the degree of

**MASTER OF SCIENCE IN PHYSICAL OCEANOGRAPHY**

from the

**NAVAL POSTGRADUATE SCHOOL**
**December 2001**

Author: _____
Christopher S. Moore

Approved by: _____
Curtis A. Collins, Thesis Advisor

_____
Frank B. Schwing, Co-Advisor

_____
Mary L. Batteen, Chairman
Department of Oceanography

THIS PAGE INTENTIONALLY LEFT BLANK

# ABSTRACT

The annual cycle of the North Pacific wind stress, Ekman pumping and Sverdrup transport is investigated by means of empirical orthogonal function (EOF) analysis techniques. Fifty-two years of National Centers for Environmental Prediction (NCEP, formerly "NMC") and the National Center for Atmospheric Research (NCAR) Reanalysis daily averaged surface wind components covering the extratropical North Pacific are used to calculate daily averaged wind stress components. These wind stress components are averaged to 624 monthly mean fields from which monthly mean Ekman pumping and Sverdrup transport fields are derived. Each data field has the long-term annual mean and linear trend removed at each grid point before EOF analysis. The first three modes are considered to be physically significant based on the plot of the log eigenvalue against its root. The first principal components of each field are highly coherent, have most of their spectral energy at the annual cycle, and are nearly in phase. The second mode of these fields show significant spectral energy at the semiannual cycle. The third mode has more complex spatial variability than the first and second mode. The annual cycle is best described by the first EOF mode which is composed of two seasons (winter and summer) that last for five months each separated by two rapid (approximately one month) transition periods (spring and fall). The annual cycle is complex and certain geographical regions are seasonal "hot spots" that add to the complexity. Relationships are derived between the various modes to help explain seasonal movement of the Ekman pumping zero isotach and seasonal variations in Sverdrup transport. The annual variability can reasonably be described using only the first three EOF modes.

THIS PAGE INTENTIONALLY LEFT BLANK

# TABLE OF CONTENTS


I. INTRODUCTION ..... 1

II. DATA AND METHODS ..... 3
- A. DYNAMICAL CALCULATIONS ..... 3
- B. ANNUAL MEAN FIELDS ..... 5
- C. EOF ANALYSIS ..... 8

III. RESULTS ..... 13
- A. STATISTICAL ANALYSIS ..... 13
- B. EOF MODE 1 ..... 17
- C. EOF MODE 2 ..... 22
- D. EOF MODE 3 ..... 25

IV. DISCUSSION ..... 31
- A. WIND STRESS ..... 32
- B. EKMAN PUMPING ..... 40
- C. SVERDRUP TRANSPORT ..... 46
- D. INTERANNUAL VARIABILITY ..... 51

APPENDIX A. VARIANCE ..... 53

APPENDIX B. LONG-TERM MONTHLY MEAN PRINCIPAL COMPONENTS ..... 55

APPENDIX C. MAGNITUDE AND ROTATION ANGLE ..... 57

APPENDIX D. $M_{4-10}^{\tau,w,\psi}$ ..... 59

APPENDIX E. WIND STRESS MONTHLY MEANS ..... 75

APPENDIX F. EKMAN PUMPING MONTHLY MEAN ..... 79

APPENDIX G. SVERDRUP TRANSPORT MONTHLY MEANS ..... 83

APPENDIX H. COMPLEX EMPIRICAL ORTHOGONAL FUNCTION (EOF) MATLAB PROGRAM ..... 87

LIST OF REFERENCES ..... 93

INITIAL DISTRIBUTION LIST ..... 97

THIS PAGE INTENTIONALLY LEFT BLANK

# LIST OF FIGURES


Figure 1. Grid Spacing Nomenclature Figure. The Variables $I$ And $J$ Represent Column and Row Position, Respectively, in the Data Matrix. $\phi$ and $\lambda$ Denote Geographic Latitude and Longitude Respectively. .....4

Figure 2. Mean Fields Computed for the Period 1948-1999. (a) Wind Stress. Scaling Vector is 0.25 Pa. (b) Ekman Pumping. The Contour Interval is 5 cm day$^{-1}$. Zero Isotach is Bold. Upwelling Regions are Shaded. (c) Sverdrup Transport. The Streamline Interval is 10 Sv (1 Sv $\equiv$ $10^6$ m$^3$ s$^{-1}$). Arrowheads Indicate the Direction of the Transport. Zero is Bold. Positive Values are Dashed Lines and Negative Values are Solid Lines. .....6

Figure 3. Standard Deviation of the Mean Fields Computed for the Period 1948-1999. (a) Wind Stress. Scaling Vector is .07 Pa. (b) Ekman Pumping. Contour Interval is 5 cm day$^{-1}$. (c) Sverdrup Transport. The Streamline Interval 5 Sv (1 Sv $\equiv$ $10^6$ m$^3$ s$^{-1}$). .....7

Figure 4. Scree Test Plot of $\lambda_k^{\tau}$ (Solid Line), $\lambda_k^{w}/10^4$ (Solid Bold Line) and $\lambda_k^{\psi}/10^{16}$ (Broken Bold Line) for k=(1,2,…10) versus Eigenvalue Root Number. .....13

Figure 5. Log EigenValue (LEV) Graph for the Data Fields as Labeled. The First Three Eigenvalues are Designated by Triangles.....14

Figure 6. Power Spectra of $PC_1^X$ (Thin Solid Line), $PC_2^X$ (Broken Line), and $PC_3^X$ (Bold Solid line) for (a) $\mathrm{Re}\left(PC_k^{\tau}\right)$, (b) $\mathrm{Re}\left(PC_k^{w}\right)$ and (c) $\mathrm{Re}\left(PC_k^{\psi}\right)$ for the Entire Time Series. Each time Series has been Weighted by its Variance. .....16

Figure 7. Coherence Function Estimate for the Entire Monthly Averaged Time Series (1948-1999) of $\mathrm{Re}\left(PC_1^{\tau}\right)$ and $PC_1^{w}$ (Solid Line), $\mathrm{Re}\left(PC_1^{\tau}\right)$ and $PC_1^{\psi}$ (Broken Line), $PC_1^{w}$ And $PC_1^{\psi}$ (Broken Dotted Line). .....17

Figure 8. Seasonal Time Series of $PC_{1\overline{m}}^X$. (a) *rotation angle* $\left(PC_{1\overline{m}}^{\tau}\right)$ is the Solid Line and *magnitude* $\left(PC_{1\overline{m}}^{\tau}\right)$ is the Broken Line (b) $\mathrm{Re}\left(PC_{1\overline{m}}^{\tau}\right)$ is the Solid Line and $\mathrm{Im}\left(PC_{1\overline{m}}^{\tau}\right)$ is the Broken Line. (c) $PC_{1\overline{m}}^{w}$ (D) $PC_{1\overline{m}}^{\psi}$. Shaded Region is $\pm 1\sigma$. .....21

Figure 9. Eigenvector ($E_1^X$) Plots. (a) $E_1^{\tau}$. Scaling Vector is 0.25 Pa. (b) $E_1^{w}$. Contour Interval is 100 cm Day$^{-1}$. (c) $E_1^{\psi}$. Solid Lines Indicate Negative Values. Arrowheads Indicate Direction of Transport. Zero is Denoted by the Bold Line.....22

Figure 10. Coherence Function Estimate for the Entire Monthly Averaged Time Series (1948-1999) of $\mathrm{Re}\left(PC_2^{\tau}\right)$ and $PC_2^{w}$ (Solid Line), $\mathrm{Re}\left(PC_2^{\tau}\right)$ and $PC_2^{\psi}$ (Broken Line), $PC_2^{w}$ and $PC_2^{\psi}$ (Broken Dotted Line). .....23

Figure 11. Seasonal Time Series of $PC^{X}_{2\overline{m}}$. (a) $rotationangle\left(PC^{\tau}_{2\overline{m}}\right)$ is the *Solid Line* and $magnitude\left(PC^{\tau}_{2\overline{m}}\right)$ is the *Broken Line* (b) $\mathrm{Re}\left(PC^{\tau}_{2\overline{m}}\right)$ is the *Solid Line* and in $\mathrm{Im}\left(PC^{\tau}_{2\overline{m}}\right)$ is the *Broken Line*. (c) $PC^{w}_{2\overline{m}}$ (d) $PC^{\psi}_{2\overline{m}}$. Shaded Region is $\pm 1\sigma$. ....26

Figure 12. Eigenvector ($E^{X}_{2}$) Plots. (a) $E^{\tau}_{2}$. Scaling Vector is 0.25 Pa. (b) $E^{w}_{2}$. Contour Interval is 100 cm Day$^{-1}$. (c) $E^{\psi}_{2}$. Solid Lines Indicate Negative Values. Arrowheads Indicate Direction of Transport. Zero is Denoted by the Bold Line....27

Figure 13. Seasonal Time Series of $PC^{X}_{3\overline{m}}$. (a) $rotationangle\left(PC^{\tau}_{3\overline{m}}\right)$ is the *Solid Line* and $magnitude\left(PC^{\tau}_{3\overline{m}}\right)$ is the *Broken Line* (b) $\mathrm{Re}\left(PC^{\tau}_{3\overline{m}}\right)$ is the *Solid Line* and $\mathrm{Im}\left(PC^{\tau}_{3\overline{m}}\right)$ is the *Broken Line*. (c) $PC^{w}_{3\overline{m}}$ (d) $PC^{\psi}_{3\overline{m}}$. Shaded Region is $\pm 1\sigma$. ....29

Figure 14. Eigenvector ($E^{X}_{3}$) Plots. (a) $E^{\tau}_{3}$. Scaling Vector is 0.25 Pa. (b) $E^{w}_{3}$. Contour Interval is 100 cm Day$^{-1}$. (c) $E^{\psi}_{3}$. Solid Lines Indicate Negative Values. Arrowheads Indicate Direction of Transport. Zero is Denoted by the Bold Line....30

Figure 15. Monthly Mean Wind Stress (Pa). Scaling Vector is 0.25 Pa. ....34

Figure 16. $M^{\tau}_{1,2,3} + \overline{X}$ for the Months Indicated. Scaling Vector is 0.25 Pa. ....35

Figure 17. $M^{\tau}_{1,2,3}$ Residuals for the Months Indicated. Scaling Vector is 0.25 Pa. ....36

Figure 18. Monsoon Wind Stress Monthly Means (Top Row) and $PC^{\tau}_{1} + \overline{X}$ (Bottom Row). Units are Pascals (Pa = kg m$^{-1}$ s$^{-2}$). Scaling Vector is 0.25 Pa. ....39

Figure 19. Monthly Mean Ekman Pumping. The Zero Isotach is Bold. The Contour Interval is 5 cm day$^{-1}$. Upwelling Regions are Shaded. ....41

Figure 20. Monthly Mean Ekman Pumping or Vertical Velocity at the Base of the Ekman Layer as a Result of Divergence of the Ekman Transport Computed for the Period 1948-1999. The Contour Interval is 5 cm day$^{-1}$. Zero Isotach is Bold. Upwelling Regions are Shaded. Geographic Limits As Shown. ....43

Figure 21. $M^{w}_{1,2,3} + \overline{X}$ for the Months Indicated. The Zero Isotach is Bold. The Contour Interval is 5 cm day-1. Upwelling Regions are Shaded. ....44

Figure 22. $M^{w}_{1,2,3}$ Residuals for the Months Indicated. The Zero Isotach is Bold. The Contour Interval is 5 cm day$^{-1}$. Positive Values (Shaded Regions) Indicate Area where the Seasonal Mean is Greater. ....45

Figure 23. Streamlines of Monthly Mean Sverdrup Transport. Zero is Bold. Arrowheads Indicate the Direction of the Transport. Positive Values are Dashed Lines. Zero Line is in Bold. Contour Interval is 10 Sverdrups (1 Sv ≡ $10^{6}$ m$^{3}$ s$^{-1}$). ....47

Figure 24. $M^{\psi}_{1,2,3} + \overline{X}$ Streamlines for the Months Indicated. Arrowheads Indicate the Direction of the Transport. Positive Values are Dashed Lines. Contour Interval is 10 Sverdrups (1 Sv ≡ $10^6$ $m^3$ $s^{-1}$). Zero Line is in Bold. ....49

Figure 25. Comparison of Depth Averaged Transport in the Tokara Strait and Sverdrup Transport in the Region. Seasonal Variability of Depth Averaged Transport (Thick Black Line). The Sverdrup Transport (Thick Grey Line) and the $PC^{\psi}_{1} + \overline{X}$ Sverdrup Transport (Thin Grey Line) is the Transport between the Two Grid Points Nearest the Tide Stations, 27.5°N,130°E And 30°N,130°E. The Sverdrup Transport is Derived from NCEP Wind Observations (1948-1999) as Described Above ....51

Figure 26. Smoothed Time Series (36 point) of $PC^{X}_{km}$ as Indicated Versus Smoothed Time Series (36 point) Monthly NOI(/-15) Values (Schwing *et al*., 2001) (heavy gray line). NOI is an Index of North Pacific Climate Variability. ....52

THIS PAGE INTENTIONALLY LEFT BLANK

# LIST OF TABLES

Table 1. Variables Description and Units Used in Text. .....2

Table 2. Percentage of the Total Variance and the Cumulative Variance Explained by the First Three EOF Modes for Wind Stress ($\tau$ = $Pa^2$), Ekman Pumping ($w$ = $cm^2\ day^{-2}$) and Sverdrup Transport ($\psi$ = $Sv^2$).....15

Table 3. North Pacific Transports (Sv) Values based on NCEP Wind Stress Forcing from 1948-1999 for Winter (February) and Summer (September). For Comparison, Transports from Two Other Studies for Winter (January) and Summer (July) are Shown. Sources are Trenberth Et Al. (1990), Derived from ECMWF (EC) and Hellerman and Rosenstein (HR) Wind Climatologies. .....48

THIS PAGE INTENTIONALLY LEFT BLANK

# ACKNOWLEDGMENTS

Ralph Waldo Emerson once remarked that sometimes a scream is better than a thesis. Often when this thesis became increasingly a race between education and catastrophe, a scream would alleviate some anguish. However, many bright and caring people gave me the strength to finish the race and I would like to acknowledge them here.

I would like to gratefully acknowledge the guidance and support of my two thesis advisors, Professor Curt Collins of the Oceanography Department, Naval Postgraduate School and Dr. Frank Schwing of the National Oceanographic and Atmospheric Administration (NOAA), Pacific Fisheries Environmental Laboratory (PFEL) in Pacific Grove, California. Thank you, Curt, for always caring about the science. Your challenges have made this a far better product than I could have envisioned. I will always be grateful to you, Frank, for your mentorship, friendship and confidence in abilities I had yet to discover in myself. I have learned more than oceanography from an all too brief time in working with you.

A special thanks to the two laboratory directors that have allowed me time as an employee to finish this academic pursuit, Dr. George Boehlert, PFEL, and Dr. Churchill Grimes, NOAA, Santa Cruz Laboratory.

I would also like to acknowledge the staff at PFEL where the bulk of this research was conducted, especially Phaedra Green Jessen, Steve Cummings, Jerry Norton and Art Stroud.

Lastly, but most importantly, I would like to thank my loving wife, Beth, for her care, insight, support, and patience. You will always be my hero.

THIS PAGE INTENTIONALLY LEFT BLANK

# I. INTRODUCTION

The surface momentum flux from the atmosphere, or wind stress, and the curl of the wind stress acting on the sea surface are fundamental forcing agents for dynamic ocean processes (Bakun and Nelson, 1991). Basin-wide winds, rather than local forcing, have been shown to be responsible for interannual fluctuations in the California Current System (CCS) (Chelton and Davis, 1982). Bryden *et al.* (1991) suggest that the surface circulation in the North Pacific controls the net meridional heat transport. Large-scale wind stress variations and the resulting Ekman pumping have major effects on the biological systems and marine fisheries at El Niño and decadal time scales (Brodeur and Ware, 1992; Beamish and Bouillon, 1993; Parrish *et al*., 2000). Ocean-atmosphere coupled models suggest that ocean temperature variability is due to coupling between the subtropical gyre and the wind stress field associated with the Aleutian Low (Latif and Barnett, 1994, 1996).

There are no direct long-term measurements of ocean circulation with regular spatial and temporal sampling. Circulation fields can be estimated from modeled and observed wind data by using fluid dynamical theory to derive lateral and vertical currents (Ekman, 1905; Sverdrup, 1947; Stommel, 1948; Munk, 1950). In recent years, ocean circulation estimates based on wind stress data from either observations (Wyrtki and Myers, 1976, Hellerman and Rosenstein, 1989, Chelton *et al*., 1990, and Xie and Hsieh, 1995) or model output have been developed for individual ocean areas and for the world ocean (Trenberth *et al*., 1990).

The goal of this thesis is to describe the annual cycle of the extratropical North Pacific wind stress and the derived circulation fields (Ekman pumping and Sverdrup transport) using Empirical Orthogonal Function (EOF) analysis. Annual means of the output of the EOF analysis and statistical correlations between the modes of the various fields will be described in an attempt to identify their seasonal dominance and spatial patterns. Table 1 provides a list of symbols used and follows standard oceanographic and statistical practice.

| Variable | Description | Units |
|---|---|---|
| $\overline{\tau}_x \left(\overline{\tau}_y\right)$ | Daily mean eastward (northward) wind stress component. | Pa |
| $M_x \left(M_y\right)$ | Monthly mean eastward (northward) Ekman transport component. | $m^2\ s^{-1}$ |
| $T_x \left(T_y\right)$ | Monthly mean eastward (northward) wind stress component. | Pa |
| $w$ | Ekman pumping vertical velocity. | cm $day^{-1}$ |
| $M_{tot}\ (\psi)$ | Monthly mean Sverdrup transport. | $10^6\ m^3\ s^{-1}$ |
| $\rho_a$ | Density of air | 1.22 kg $m^{-3}$ |
| $\phi$ | Geographic latitude | Degrees |
| $\lambda$ | Geographic longitude | Degrees |
| x | Input data matrix for a single month | |
| $X$ | Entire time series of the input data matrix | $X = T, w, \psi$ |
| $\overline{X}$ | Long-term annual mean of input data matrix (detrended) | |
| N | Number of input matrix grid points. | |
| M | Number of months in the data time series. | 624 |
| n | Grid point index | n=(1,2,…N) |
| m | Time index | m=(1,2,…M) |
| $PC_k^X$ | $k^{th}$ principal component of X | k=(1,2,…N) |
| $E_k^X$ | $k^{th}$ eigenvector of X | k=(1,2,…N) |
| $\lambda_k^X$ | $k^{th}$ eigenvalue of X | k=(1,2,…N) |
| $M_k^X$ | $k^{th}$ mode of X refers to( $PC_k^X$ , $E_k^X$ ) pairings | |
| H | Variance/covariance matrix of X | |
| $\overline{m}$ | Subscript denoting the arithmetic mean for each calendar month (m) over the entire time series (Y = (624 months x year/12 months) = 52 Years | $\overline{m} = \frac{1}{Y}\sum_{i=1}^{Y} m_i$ = (1,2,…12) |

Table 1. Variables Description and Units Used in Text.

# II. DATA AND METHODS

## A. DYNAMICAL CALCULATIONS

A 52-year subset (1948-1999) of daily averaged surface wind components from the National Centers for Environmental Prediction (NCEP) and the National Center for Atmospheric Research (NCAR) Reanalysis project (Kalnay et al., 1996) covering the North Pacific was used to calculate daily averaged wind stress. The geographical limits used are 15°N to 70°N and 100°E to 80°W. The data were gridded at 2.5° intervals for both latitude and longitude.

Daily averaged wind stress components were calculated using the formula:

$$\left(\bar{\tau}_x, \bar{\tau}_y\right) = \rho_a C_D \left( \left|\vec{W}_{995}\right| U_{995}, \left|\vec{W}_{995}\right| V_{995} \right) \tag{1}$$

where $\bar{\tau}_x$ ($\bar{\tau}_y$) denotes the eastward (northward) daily averaged component of wind stress, $\rho_a$ is the density of air (a constant 1.22 kg m$^{-3}$), $C_D$ is a non-linear drag coefficient based on Large and Pond (1981) and modified for low wind speeds as in Trenberth et al. (1990), $|W_{995}|$ is the wind speed, and $U_{995}$ ($V_{995}$) is the eastward (northward) component of the wind velocity (m sec$^{-1}$) at sea level, respectively.

The resultant long-term monthly mean eastward ($T_x$) and northward ($T_y$) wind stress components at each station (N = 1679 grid points) were computed as the arithmetic means of the daily eastward and northward components for each month over the entire time series (M = 624 months). These values were used to derive the monthly mean circulation fields as follows.

The monthly averaged eastward ($M_x$) and northward ($M_y$) components of the Ekman transport (m$^2$ s$^{-1}$) were calculated using the formula:

$$\left(M_x,\, M_y\right) = \left(\frac{\mathrm{T}_y}{\rho_{sw} f}, \frac{-\mathrm{T}_x}{\rho_{sw} f}\right) \tag{2}$$

where $\rho_{sw}$ is the density of seawater (a constant, 1025 kg m$^{-3}$) and f is the Coriolis parameter. Monthly averaged values for Ekman pumping, or open-ocean upwelling (cm day$^{-1}$) were calculated as the divergence of the surface Ekman transport using the formula:

$$w_{(i,j)} = \left[\left(\frac{M_{x(i+1,j)} - M_{x(i-1,j)}}{2\Delta\lambda}\right) + \left(\frac{M_{y(i,j-1)} - M_{y(i,j+1)}}{2\Delta\phi}\right)\right] \tag{3}$$

where $\phi$ and $\lambda$ denote geographic latitude and longitude, respectively, $\Delta\lambda = 2.5°$ and $\Delta\phi = (\Delta\lambda \cos \phi)$. Subscripts $i$ and $j$ represent column and row position in the data matrix (Figure 1).

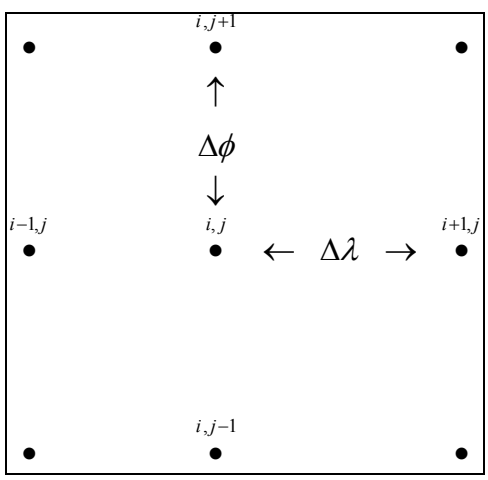


Figure 1. Grid Spacing Nomenclature Figure. The Variables *I* And *J* Represent Column and Row Position, Respectively, in the Data Matrix. $\phi$ and $\lambda$ Denote Geographic Latitude and Longitude Respectively.

Centered differences were used throughout the interior of the data matrix. Column and row end values were used at the boundaries of the data matrix. Most of the column and row end values lay over landmasses and any artificial feature introduced at the boundaries did not greatly affect oceanic circulation calculations.

Sverdrup transports were computed from the meridional transport, $M_y$. This was derived from the Sverdrup transport streamfunction relationship ($M_{tot} = \int_0^{-x} M_y \, dx$), by integrating westward from the eastern ocean boundary to the western ocean boundary between 15° and 57.5°N (N = 1314 grid points). The Aleutian Islands were ignored. Monthly averaged values for Sverdrup transport ($M_{tot}$, Sverdrup units = $10^6$ m$^3$ s$^{-1}$) were calculated by:

$$M_{tot(i-1,j)} = M_{tot(i,j)} - \left[ \frac{\Delta\lambda}{2} \left( M_{y_{(i,j)}} + M_{y(i-1,j)} \right) \right] \tag{4}$$

where $M_y$ is the Sverdrup meridional transport at location $(i, j)$ and $M_{tot}$ is initialized to zero at the eastern boundary.

## B. ANNUAL MEAN FIELDS

Annual mean fields were computed as the arithmetic mean over the entire time series and are shown in Figure 2. The mean wind stress field (Figure 2a) is dominated by a cyclonic circulation centered about 52°N, 170°E associated with the Aleutian low and anticyclonic circulation associated with the subtropical North Pacific high centered about 30°N, 140°W. There are strong westward wind stresses in the subtropics (15°-25°N) and strong eastward wind stresses in the mid-latitudes (35°-50°N, 140°E - 180°). The eastward wind stress drives a southward Ekman transport carrying cold water equatorward. The persistent westward trade winds in the subtropics drive a northward Ekman transport of warm water poleward. Due to convergence (divergence) of the surface Ekman layer within the westerly (easterly) wind stress regions, the subpolar region has resultant open ocean upwelling and the subtropical region has resultant open

ocean downwelling (Figure 2b). Strong equatorward alongshore and divergent (upwelling favorable) wind stress is found along California and the Baja peninsula. The equatorward wind stress along the eastern boundary creates a region of intense coastal upwelling. Through conservation of potential vorticity, anticyclonic circulation in the subtropical gyre and cyclonic circulation in the subpolar gyre is established (Figure 2c).

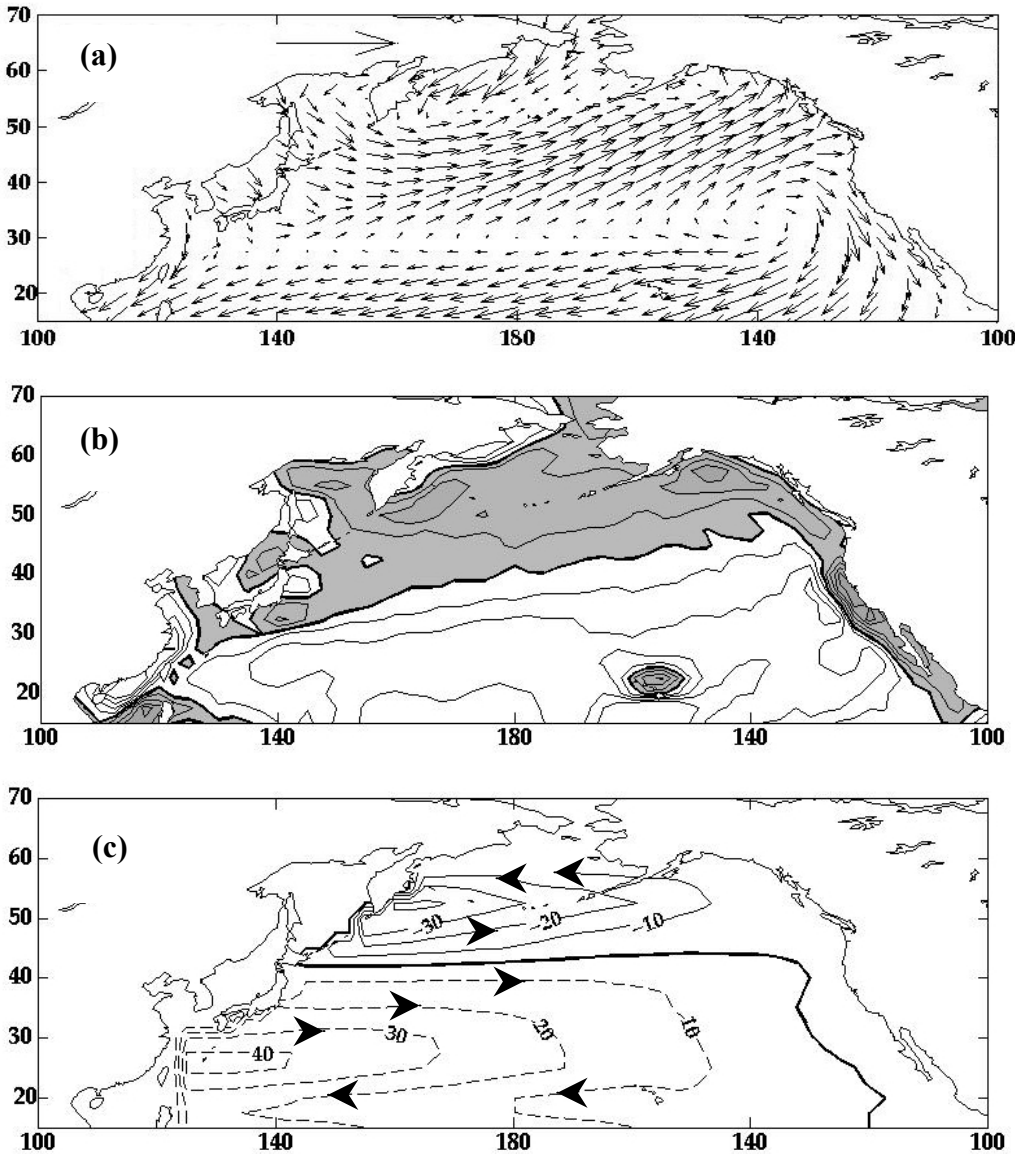


Figure 2. Mean Fields Computed for the Period 1948-1999. (a) Wind Stress. Scaling Vector is 0.25 Pa. (b) Ekman Pumping. The Contour Interval is 5 cm day$^{-1}$. Zero Isotach is Bold. Upwelling Regions are Shaded. (c) Sverdrup Transport. The Streamline Interval is 10 Sv (1 Sv ≡ $10^6$ m$^3$ s$^{-1}$). Arrowheads Indicate the Direction of the Transport. Zero is Bold. Positive Values are Dashed Lines and Negative Values are Solid Lines.

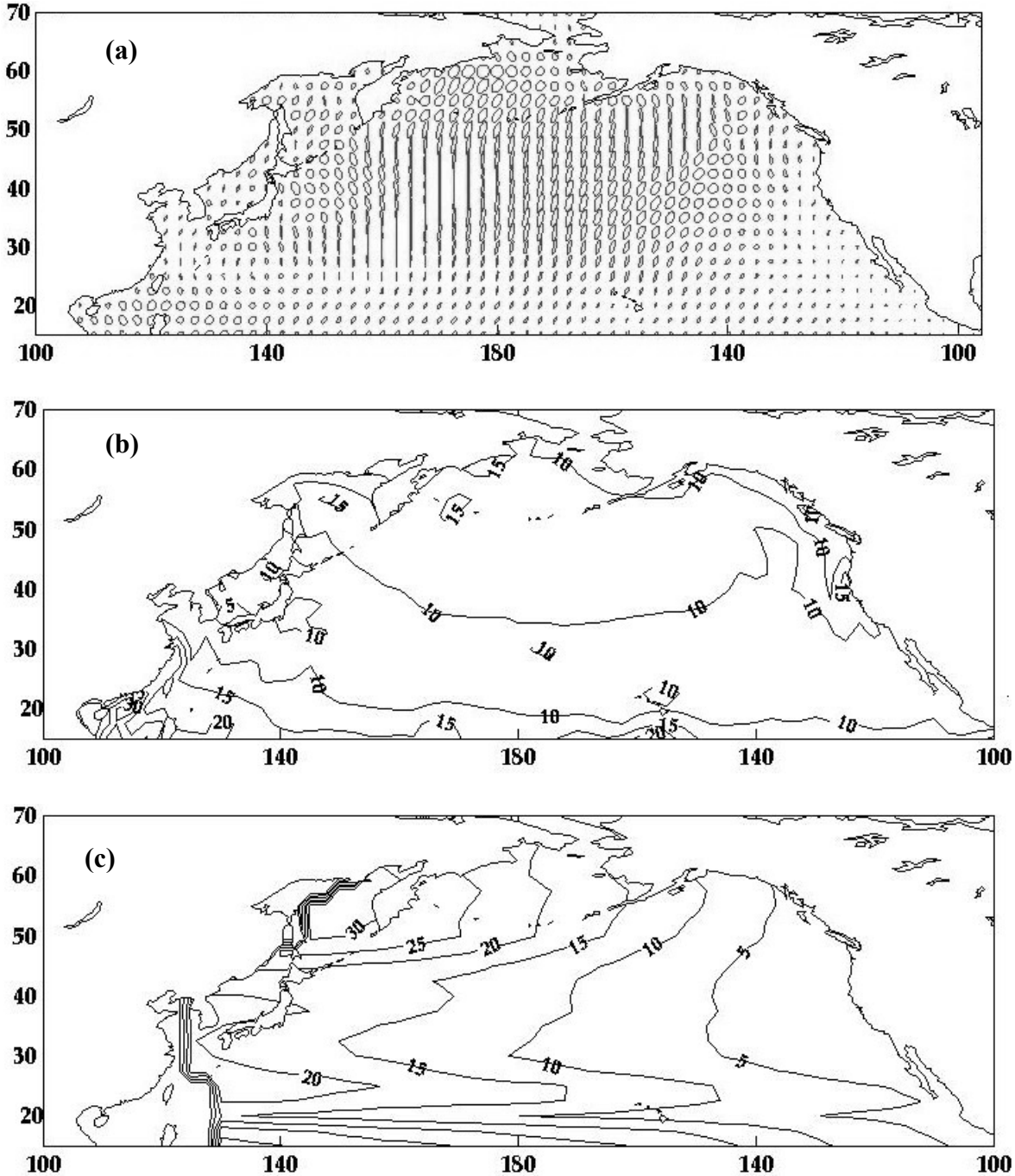


Figure 3. Standard Deviation of the Mean Fields Computed for the Period 1948-1999. (a) Wind Stress. Scaling Vector is .07 Pa. (b) Ekman Pumping. Contour Interval is 5 cm day$^{-1}$. (c) Sverdrup Transport. The Streamline Interval 5 Sv (1 Sv $\equiv 10^6$ m$^3$ s$^{-1}$).

## C. EOF ANALYSIS

Atmospheric forcing and the resultant oceanographic response are variable on a range of temporal and spatial scales (Hare, 1996). These overlapping processes produce a complicated picture that often defies simple explanation. However, with the use of "eigentechniques", such as EOF analysis, one can link both the temporal and spatial patterns of long-term records covering large spatial areas (Kutzbach, 1967; Barnett, 1977; Hardy and Walton, 1978; Legler, 1983; Hare, 1996; Mizoguchi *et al*., 1999).

The underlying mathematical principles of EOF analysis for scalar values (Ekman pumping and Sverdrup transport) and vector quantities (wind stress) are similar. The goal of such an analysis is to reduce the number of variables in the original data set while maintaining the total variance of the original data set (Hare, 1996).

The EOF analysis used in this study parallels the notation and methodology of Legler (1983). A data field was defined over $N$ grid points on $M$ time steps. Each data field had the long-term annual mean ($\overline{X}$) and linear trend removed at each grid point. The input matrix **X** was of dimension $N \times M$, with $n=(1,2,\ldots N)$ indexing grid points and $m=(1,2,\ldots M)$ indexing time, and contained the whole data set. The value of the field at any point in time and space is denoted as $x_{n,m}$. Wind stress components at each station were combined into a vector quantity of the complex form $x_{n,m} = \mathrm{T}_{x\ n,m} + i\,\mathrm{T}_{y\ n,m}$. The input data matrix is written in matrix notation as

$$X = \begin{bmatrix} x_{11} & x_{12} & . & . & . & x_{1M} \\ x_{21} & & & & & . \\ . & & & & & . \\ . & & & & & . \\ . & & & & & . \\ x_{N1} & . & . & . & . & x_{NM} \end{bmatrix} \tag{5}$$

The variance/covariance matrix $(H)$ is expressed as

$$[H] = \frac{1}{M}[X]\left[X^T\right] \tag{6}$$

where $X^T$ represents the transpose, or complex conjugate transpose in the case of the wind vectors, of $X$. $H$ is a Hermitian matrix, which is symmetric (NxN) with real-valued diagonal elements.

The EOF analysis has three results: principal components ($PC_k^X$), eigenvectors ($E_k^X$) and eigenvalues ($\lambda_k^X$), where the subscript $k$ = (1,2,…N) and the superscript $X$ designates the data field (wind stress ($\tau$), Ekman pumping, ($w$), and Sverdrup transport ($\psi$). The eigenvalue decomposition of $[H]$ produces a diagonal matrix $\left[\lambda_k^X\right]$ of eigenvalues and a full matrix $\left[E_k^X\right]$ whose columns are the corresponding eigenvectors so that

$$[H]\left[E_k^X\right] = \left[E_k^X\right]\left[\lambda_k^X\right] \tag{7}$$

Each eigenvalue, $\lambda_k^X$, has an associated spatial eigenvector, $E_k^X$. The eigenvectors have a spatial orthogonal relationship, that is, each eigenvector is orthogonal to all those preceding it. $E_k^\tau$ are in the complex form (Re $\left(E_k^\tau\right)$+ $i$ Im $\left(E_k^\tau\right)$).

$E_k^w$ and $E_k^\psi$ fields are displayed as contour and streamline maps, respectively. $E_k^\tau$ fields are displayed in vector form. $E_k^\tau$ vectors are computed using the formula

$$\left(E_k^\tau\right) = \sqrt{\mathrm{Re}\left(E_k^\tau\right)^2 + \mathrm{Im}\left(E_k^\tau\right)^2} \tag{8}$$

The PC for each eigenvector $k$ at time $\overline{m}$ is obtained from the equation

$$PC_{k\overline{m}}^{X} = \left[ \left( E_k^X \right)^T \right] \square \left[ X_{\overline{m}} \right] \tag{9}$$

where $X_{\overline{m}}$ represents a column vector from the monthly mean of the input data. The time series of the coefficients for eigenvector $E_k^X$ is known as the $k^{th}$ principal component ($PC_k^X$). In this study a seasonal time series of PCs are computed as the arithmetic mean ($\overline{m}$) of all the PCs for each month ($m$) over the entire time series *m=(1,2,…M)*.

The spatial positioning of the eigenvector patterns does not change over time. $PC_{k\overline{m}}^{w,\psi}$ modulate the magnitude of the eigenvector fields over time. $PC_{k\overline{m}}^{\tau}$ modulate both vector magnitude and rotation angle over time. $PC_k^{\tau}$ is of the complex form $\mathrm{Re}\left(PC_{k\overline{m}}^{\tau}\right) + i\,\mathrm{Im}\left(PC_{k\overline{m}}^{\tau}\right)$. Magnitude and rotation angle information are calculated as:

$$magnitude\left(PC_{k\overline{m}}^{\tau}\right) = \sqrt{\mathrm{Re}\left(PC_{k\overline{m}}^{\tau}\right)^2 + \mathrm{Im}\left(PC_{k\overline{m}}^{\tau}\right)^2} \tag{10}$$

and

$$rotation\ angle\left(PC_{k\overline{m}}^{\tau}\right) = \tan^{-1}\left(\frac{\mathrm{Im}\left(PC_{k\overline{m}}^{\tau}\right)}{\mathrm{Re}\left(PC_{k\overline{m}}^{\tau}\right)}\right) \tag{11}$$

$E_k^{\tau}$ vector fields are modulated by both the $magnitude\left(PC_{k\overline{m}}^{\tau}\right)$ and $rotation\ angle\left(PC_{k\overline{m}}^{\tau}\right)$ time series. A positive (negative) $rotation\ angle\left(PC_{k\overline{m}}^{\tau}\right)$ rotates $E_k^{\tau}$ vectors in a cyclonic (anticyclonic) manner around the grid point at the base of each vector.

The $PC_{k\overline{m}}^{X}, E_{k}^{X}$ pairings are referred to as modes and are designated $M_{k}^{X}$. The modes are ranked by their overall variability with respect to the total dataset. The contribution of each mode to the total variance of the dataset is calculated by dividing the corresponding $\lambda_{k}^{X}$ by the trace of the variance/covariance matrix where

$$TRACE\,[H] = \sum_{k=1}^{N} \lambda_{k}^{X} \tag{12}$$

The original data at any time $\overline{m}$ can be recreated by the complete set of orthonormal eigenvectors through the relationship

$$\left[X_{\overline{m}}\right] = \left( \sum_{i=1}^{N} PC_{k\overline{m}}^{X} \bullet \left[E_{k}^{X}\right] \right) + \overline{X} \tag{13}$$

It is important to remember in the following discussion that the output of this EOF analysis represents anomalies to the mean field.

THIS PAGE INTENTIONALLY LEFT BLANK

# III. RESULTS

## A. STATISTICAL ANALYSIS

Two methods were used to determine the significance of the EOF modes that were based on the relative magnitudes of the eigenvalues; the Scree test and the Log EigenValue (LEV) graph. The term scree derives from the resemblance to the rubble that forms at the foot of a mountain. Cattell (1966) hypothesized the scree represented unwanted noise and that only the EOF/PCs prior to the scree should be retained for further use. Identification of the exact root where the scree begins to form is rather subjective, however. A visual inspection of a plot of the eigenvalue versus its root (Scree test) (Figure 4) showed the typical eigenvalue plot that had a steep slope over the first few roots and then a gradual trailing off of the rest of the roots (the scree). The first two eigenvalues define the slope and the third is at the top of the scree. In other words, $E_{1,2,3}^{\tau,w,\psi}$ appear to be above the scree and therefore may be significant.

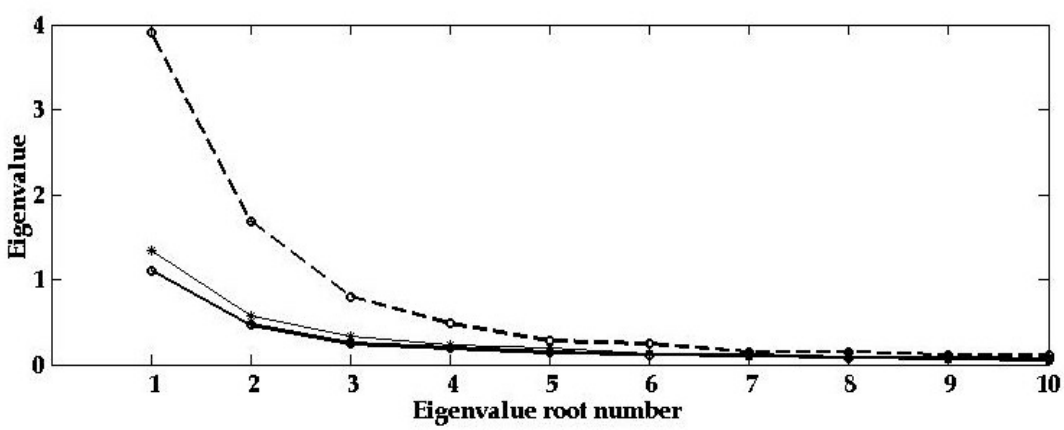


Figure 4. Scree Test Plot of $\lambda_k^{\tau}$ (Solid Line), $\lambda_k^{w}/10^4$ (Solid Bold Line) and $\lambda_k^{\psi}/10^{16}$ (Broken Bold Line) for k=(1,2,…10) versus Eigenvalue Root Number.

A plot of the LEV versus its root (Craddock and Flood, 1969) is shown in Figure 5. Experimental results indicate that an EOF of random data results in a straight-line LEV graph (Farmer, 1971). To determine the number of modes to retain, a straight line is drawn through the higher number roots, and those lying above the line are retained. To

emphasize the break-point of the lower number roots from the straight line (gray line), only the first 400 modes are shown here. $M_{1,2,3}^{\tau,w,\psi}$ were significantly above the noise level and, therefore, may have some physical meaning.

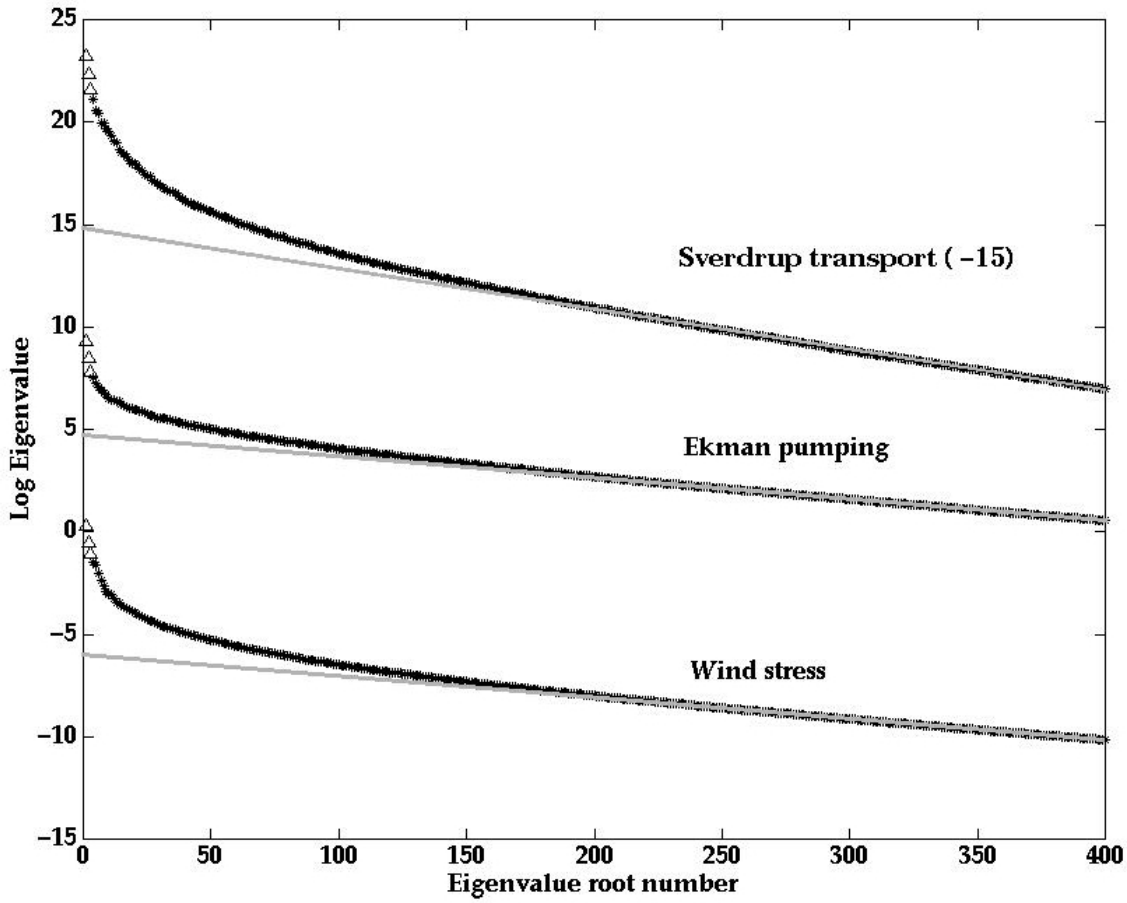


Figure 5. Log EigenValue (LEV) Graph for the Data Fields as Labeled. The First Three Eigenvalues are Designated by Triangles.

This study focused on $M_{1,2,3}^{\tau,w,\psi}$. $M_{4-10}^{\tau,w,\psi}$ are presented in Appendix D. The percent of variance and cumulative variance for the first three eigenvalues are given in Table 2. Only a few EOF modes were needed to explain a large part of the variance for each series of fields. $M_{1,2,3}^{\tau}$, $M_{1,2,3}^{w}$, $M_{1,2,3}^{\psi}$ accounted for 57.9%, 38.5% and 74.6% of the total variance, respectively.

| Mode | VARIANCE | | | | | |
|---|---|---|---|---|---|---|
| | $\tau$ | | $w$ | | $\psi$ | |
| | Percent | Cumulative | Percent | Cumulative | Percent | Cumulative |
| 1 | 34.5 | 34.5 | 23.5 | 23.5 | 45.6 | 45.6 |
| 2 | 14.9 | 49.4 | 9.9 | 33.4 | 19.7 | 65.3 |
| 3 | 8.5 | 57.9 | 5.1 | 38.5 | 9.3 | 74.6 |

Table 2. Percentage of the Total Variance and the Cumulative Variance Explained by the First Three EOF Modes for Wind Stress ($\tau$ = Pa$^2$), Ekman Pumping ($w$ = cm$^2$ day$^{-2}$) and Sverdrup Transport ($\psi$ = Sv$^2$).

Spectral analysis of the entire time series of $PC_{1,2,3}^{\tau,w,\psi}$ (Figures 7a, b, c) showed that most of $PC_1^{\tau,w,\psi}$ spectral energy was found at the annual (0.083/month) cycle. $PC_1^{\tau,w,\psi}$ also exhibited a small amount of energy at the semiannual (0.167/month) cycle. $PC_2^{\tau,\psi}$ spectra had more energy at the semiannual cycle than at the annual cycle; however $PC_2^{w}$ spectra had more energy at the annual cycle than at the semiannual cycle. Power spectra for $PC_3^{\tau,\psi}$ was generally in the noise level of the $PC_1^{\tau,\psi}$ spectra, although $PC_3^{w}$ spectra showed energy above the noise level at the semiannual cycle. Coherence function estimates for the entire series of $PC_1^{\tau,w,\psi}$ (Figure 7) showed high coherence at the annual frequency.

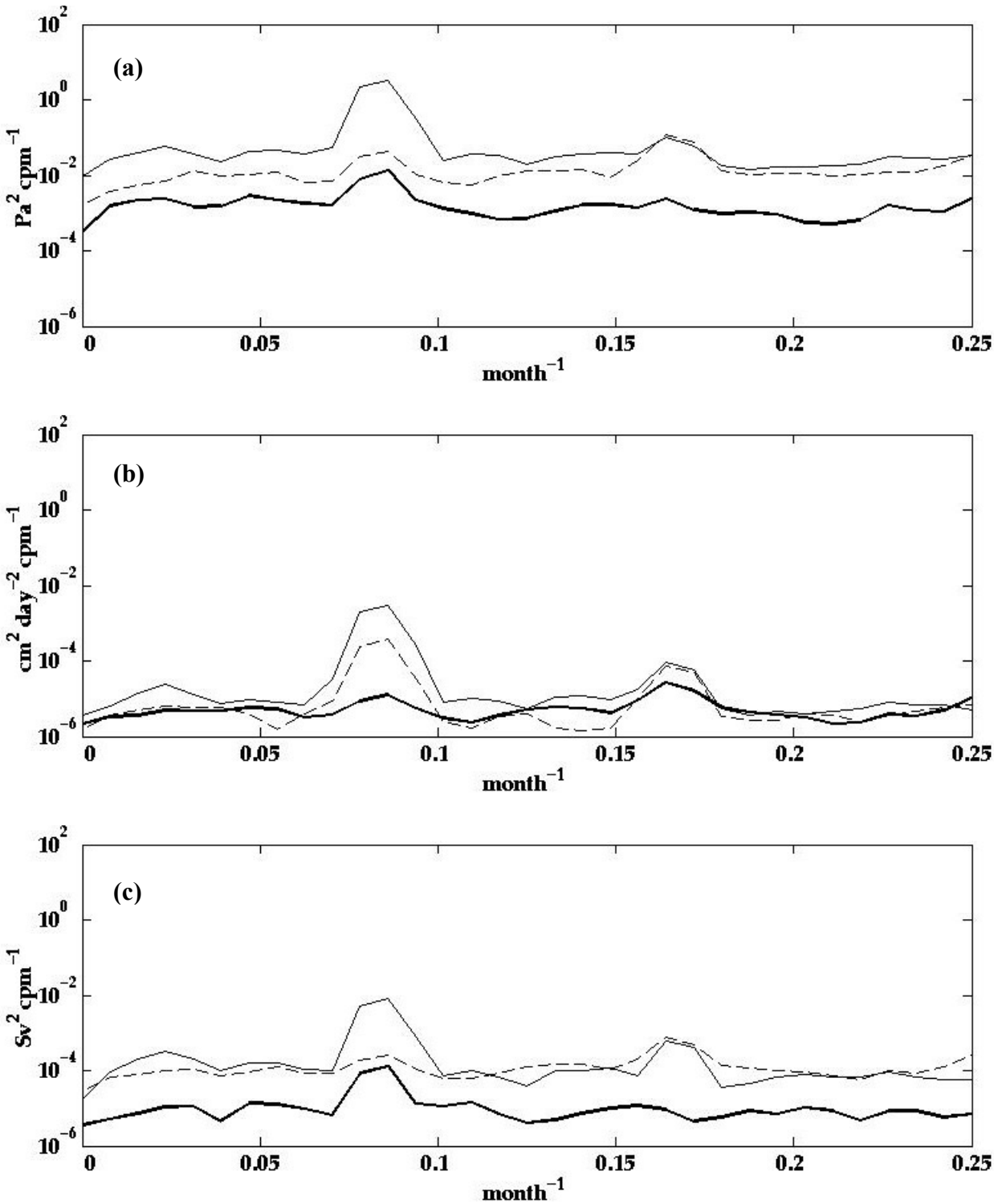


Figure 6. Power Spectra of $PC_1^X$ (Thin Solid Line), $PC_2^X$ (Broken Line), and $PC_3^X$ (Bold Solid line) for (a) $\mathrm{Re}\left(PC_k^{\tau}\right)$, (b) $\mathrm{Re}\left(PC_k^{w}\right)$ and (c) $\mathrm{Re}\left(PC_k^{\psi}\right)$ for the Entire Time Series. Each time Series has been Weighted by its Variance.

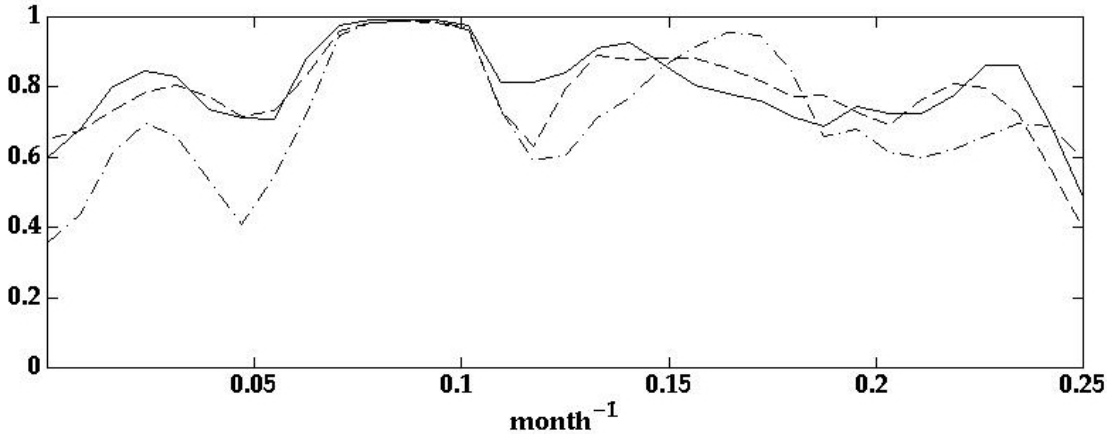


Figure 7. Coherence Function Estimate for the Entire Monthly Averaged Time Series (1948-1999) of $\mathrm{Re}\left(PC_1^{\tau}\right)$ and $PC_1^{w}$ (Solid Line), $\mathrm{Re}\left(PC_1^{\tau}\right)$ and $PC_1^{\psi}$ (Broken Line), $PC_1^{w}$ And $PC_1^{\psi}$ (Broken Dotted Line).

## B. EOF MODE 1

$M_1^{\tau}$ (Figures 8a, b and 9a), $M_1^{w}$ (Figures 8c and 9b) and $M_1^{\psi}$ (Figures 8d and 9c) account for 34.5%, 23.5% and 45.6% of the total variance, respectively (Table 2). The first principal components for wind stress, Ekman pumping and Sverdrup transport, designated $PC_{1\overline{m}}^{X}$, were uniquely similar in that all three have a coherent annual cycle. $PC_{1\overline{m}}^{X}$ had an annual cycle with a maximum in January and a minimum in July, August and September for $\mathrm{Re}\left(PC_{1\overline{m}}^{\tau}\right)$, $PC_{1\overline{m}}^{w}$ and $PC_{1\overline{m}}^{\psi}$, respectively. $PC_{1\overline{m}}^{X}$ had a larger magnitude during the winter maximum ($\mathrm{Re}\left(PC_{1m}^{\tau}\right)$ = 1.375, $PC_{1m}^{w}$ = 0.059 and $PC_{1m}^{\psi}$ = 0.052, where m = January) as opposed to the summer minimum ($\mathrm{Re}\left(PC_{1m}^{\tau}\right)$ = -1.135, $PC_{1m}^{w}$ = -0.051 and $PC_{1m}^{\psi}$ = -0.035, where m = July, August and September, respectively). The range of one standard deviation was also greater during the winter months as opposed to the summer months. In other words, the wind stress was stronger, pumping more vigorous, and the transport more robust during the height of winter than during the peak of summer. There was also greater directional and strength variability among all these fields during the winter than during the summer. The transition between winter to summer was determined by the change in the sign of the $PC_{1\overline{m}}^{X}$ and occurred

rapidly (< 1 month). During the transitional periods, designated here as the spring and fall, the contribution of the first mode to the mean field was minimal.

The dominant $E_1^\tau$ wind stress pattern was centered about 50°N, 165°W and, when combined with $PC_1^\tau$, was cyclonic from early-October to mid-March. The strongest annual wind stress (~ 0.1 Pa) were southwestward which occurred in January between 30°-40°N around the dateline. These were comparable to magnitudes of the mean field found in this region (Figure 2) however, the direction of the stress was different. The mean wind stress field showed maximum northwestward wind stress (~ 0.12 Pa) located between 40°-50°N east of the dateline that extended into the Gulf of Alaska. The mean field wind stress in this region was part of a subtropical anticyclonic circulation whereas the $M_1^\tau$ wind stress in this region was part of a cyclonic circulation pattern in the winter (October – March). During summer (April – September) the dominant wind stress pattern reversed and became anticyclonic.

Separate and less dominant features were also visible in $E_1^\tau$ along the boundaries. In the Western Pacific, equatorward wind stress associated with the monsoons occurred in the winter. Specifically, $E_1^\tau$ wind stress in the East China Sea was southward while that in the South China Sea was southwestward. The magnitude (~0.08 Pa) and relative direction during the winter were comparable with that found in the long-term mean wind stress field. In the Eastern Pacific, poleward wind stress along the California-Oregon-Washington coast occurred during the winter and reversed equatorward (upwelling favorable) during the summer. Also in the Eastern Pacific there was a region of anticyclonic circulation centered at 22.5°N, 120°W west of the Baja California Peninsula.

The Ekman pumping pattern observed in $E_1^w$ (Figure 9b) appeared related to the wind stress observed in $E_1^\tau$ (Figure 9a). In fact, straightforward fluid dynamical calculations of Ekman pumping from $E_1^\tau$ wind stress gave virtually the same geographical pumping pattern. In describing $E_1^w$ pumping, it was observed that open-ocean upwelling (downwelling) occurred from mid-October to March over much of the basin north (south) of the zero isotach which lies roughly along 30°N. This pattern

reversed from April to mid-October. North of 30°N, the interior basin of the mid-latitudes and the Gulf of Alaska regions contoured by $E_1^w$=100 had a maximum of 5.9 cm day $^{-1}$ upwelling in January and 5.1 cm day $^{-1}$ downwelling in August. Pumping south of 30°N was relatively quiescent in the mid-latitudes, but pumping maxima were found in the tropics along 15°N and west of the dateline. These regions showed maximum downwelling (~11.8 cm day $^{-1}$) in January and maximum upwelling (~10.2 cm day $^{-1}$) in August.

The pumping pattern along the western boundary consisted of intermixed centers of oppositely phased pumping. For instance, along the western boundary, maximum ($E_1^w$>200) pumping regions occur around the Kamchatka Peninsula, the Japan Sea, and the South China Sea. Most of the Asian coast north of 30°N was an upwelling region during the winter while the western boundary of the Bering Sea, east of the Kamchatka Peninsula, subtropical and tropical coastal regions were downwelling during this time. The pattern was reversed in summer.

$E_1^w$ pumping along the eastern boundary had a less complex structure than that found along the western boundary. The zero isotach separated nearshore pumping from oppositely-signed interior ocean pumping along the eastern boundary north of 30°N. A narrow strip of nearshore pumping began at the center of the Gulf of Alaska (140°W) and continued uninterrupted southward along the North American coast to the southern Baja Peninsula. This entire boundary pumping region was in phase with the subtropical open ocean pumping; downwelling in the winter and upwelling in the summer. A concentric region of intensified pumping was found within this region and was located from the Columbia River southward to the San Francisco Bay. This concentric region was an area of intense downwelling during the winter and intense upwelling during the summer. The maximum was located at about 42°N ($E_1^w$ = 300). Maximum downwelling in this small region occurred in January at a rate of 17.7 cm day$^{-1}$ and maximum upwelling occurred in August at a rate of 15.3 cm day$^{-1}$.

The most striking difference in comparison with the long-term mean field (Figure 2b) was the slope of the zero isotach across the North Pacific. $E_1^w$ had a zero isotach that

was relatively zonal centered about 30°N. The long-term mean field, however, showed a zero isotach that began in the west about 30°N and sloped northward across the Pacific to the Gulf of Alaska (~50°N) before turning south and encompassing the eastern boundary. The western boundary pumping pattern observed in the long-term mean was consistent with the winter-time pattern observed in $E_1^w$ with regards to the location, approximate magnitude and phase of pumping maxima. For example, pumping maxima were observed in both the long-term mean and $E_1^w$ in the Sea of Okhotsk and east of the Kamchatka Peninsula, in the Sea of Japan and eastward of Japan, in the Yellow Sea and the East and South China Seas. Additionally, the position of the zero isotach in the Bering sea was well correlated between the two fields.

Eastern boundary comparisons between the long-term mean and $E_1^w$ were not as well correlated. Most of the midlatitude and subtropical eastern boundary was out of phase with the long-term mean field. Additionally, the pumping maxima were not found in the same position nor were they the same geographical dimension. The $E_1^w$ concentric maxima was displaced slightly to the north of the long-term mean maxima found along the eastern boundary. Long-term mean upwelling along the eastern boundary extended from northern California to central Mexico and was more intense than that found in $E_1^w$ pumping at any time of the year. Still, a unique nearshore-offshore dipolar upwelling-downwelling feature was observed in both fields along the eastern boundary off the California coast, but in slightly different locations. Additionally, pumping activity around the Hawaiian Islands was not as robust in $E_1^w$ as in the long-term mean pumping field.

$E_1^\psi$ (Figure 9c) consisted of two gyres located at the western boundary. The strongest was cyclonic and located at 45°N. This gyre was centered on the division between the subpolar and subtropical gyre as defined by the mean field (Figure 2c). The weaker gyre was located immediately to the south at 20°N within the subtropical gyre and was anticyclonic. Maximum amplitude (0.05) occurred in January and the minimum in September (-0.04). In January, $M_1^\psi$ would increase the Kuroshio transport by 5.7 Sv and in September decrease it by 3.9 Sv.

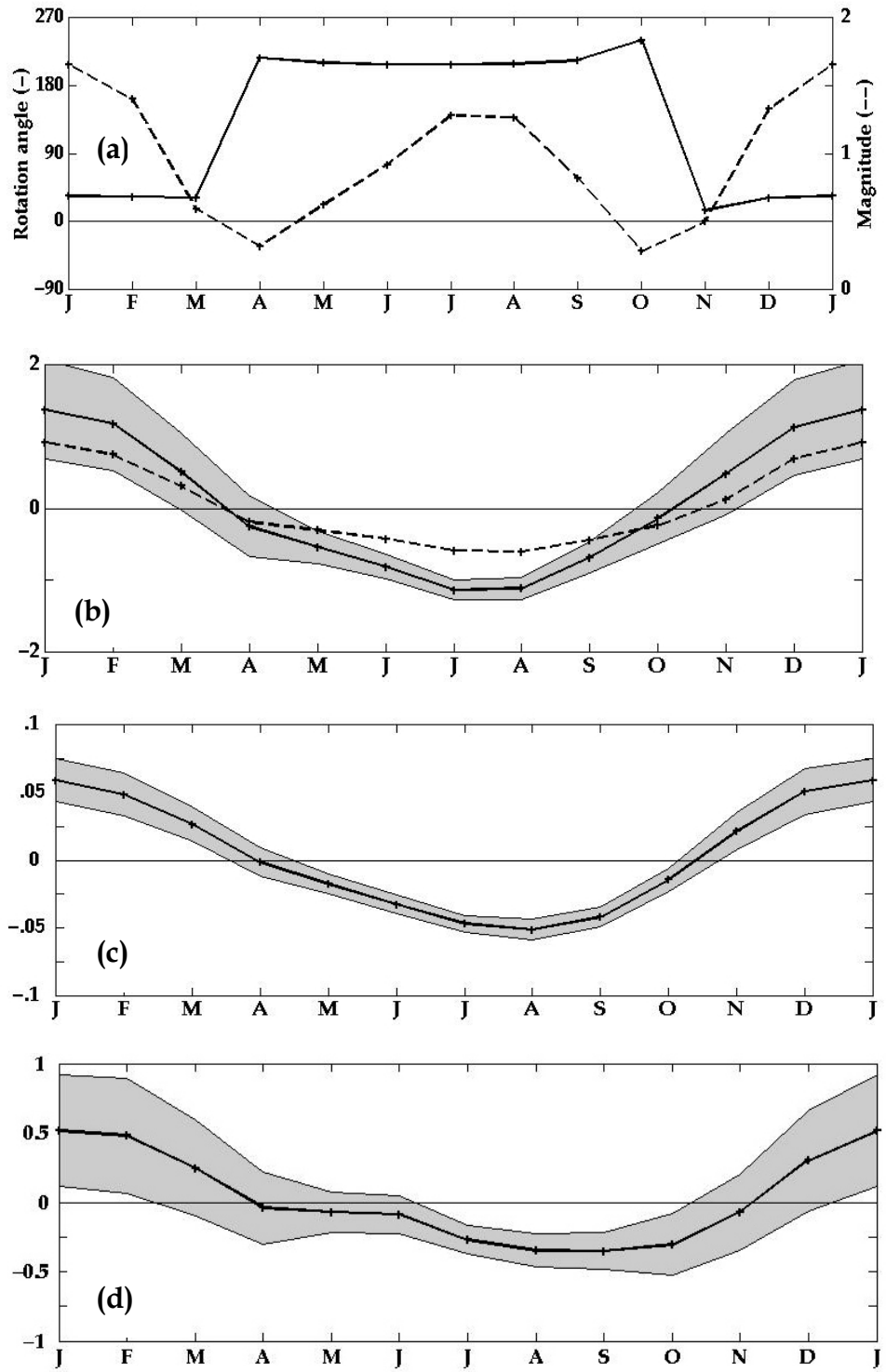


Figure 8. Seasonal Time Series of $PC_{1\overline{m}}^{X}$. (a) *rotation angle* $\left(PC_{1\overline{m}}^{\tau}\right)$ is the Solid Line and *magnitude* $\left(PC_{1\overline{m}}^{\tau}\right)$ is the Broken Line (b) $\mathrm{Re}\left(PC_{1\overline{m}}^{\tau}\right)$ is the Solid Line and $\mathrm{Im}\left(PC_{1\overline{m}}^{\tau}\right)$ is the Broken Line. (c) $PC_{1\overline{m}}^{w}$ (D) $PC_{1\overline{m}}^{\psi}$. Shaded Region is $\pm 1\sigma$.

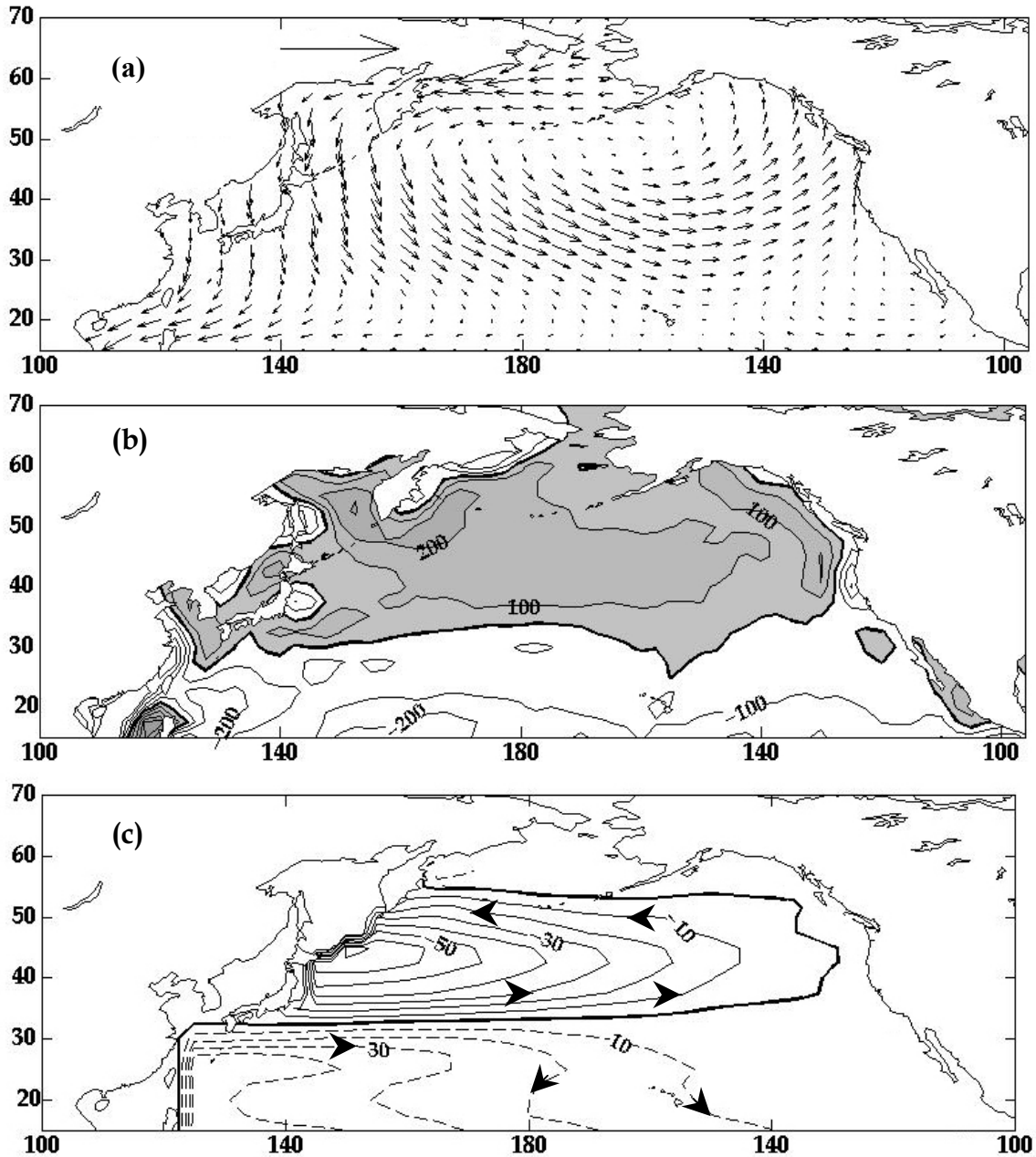


Figure 9. Eigenvector ( $E_1^X$ ) Plots. (a) $E_1^\tau$ . Scaling Vector is 0.25 Pa. (b) $E_1^w$ . Contour Interval is 100 cm Day$^{-1}$. (c) $E_1^\psi$ . Solid Lines Indicate Negative Values. Arrowheads Indicate Direction of Transport. Zero is Denoted by the Bold Line.

## C. EOF MODE 2

$M_2^\tau$ (Figures 10a,b and 11a), $M_2^w$ (Figures 10c and 11b) and $M_2^\psi$ (Figures 10d and 11c) accounted for 14.9%, 9.9% and 24.5% of the total variance, respectively. Whereas the first principal components of wind stress, Ekman pumping and Sverdrup

transport all possessed a highly coherent annual cycle, of the second principal components, only Ekman pumping ( $PC_2^w$ ) had a predominantly annual cycle. Coherence function estimates for the entire monthly averaged time series (1948-1999) for $PC_2^\tau$ and $PC_2^\psi$ showed the two time series to be highly coherent at the semi-annual cycle (Figure 8). $PC_2^\tau$, $PC_2^w$ and $PC_2^\psi$ were all at their lowest amplitude in November. $PC_2^\tau$ and $PC_2^\psi$ had larger standard deviations during winter than summer while the standard deviation of $PC_2^w$ was relatively consistent throughout the year.

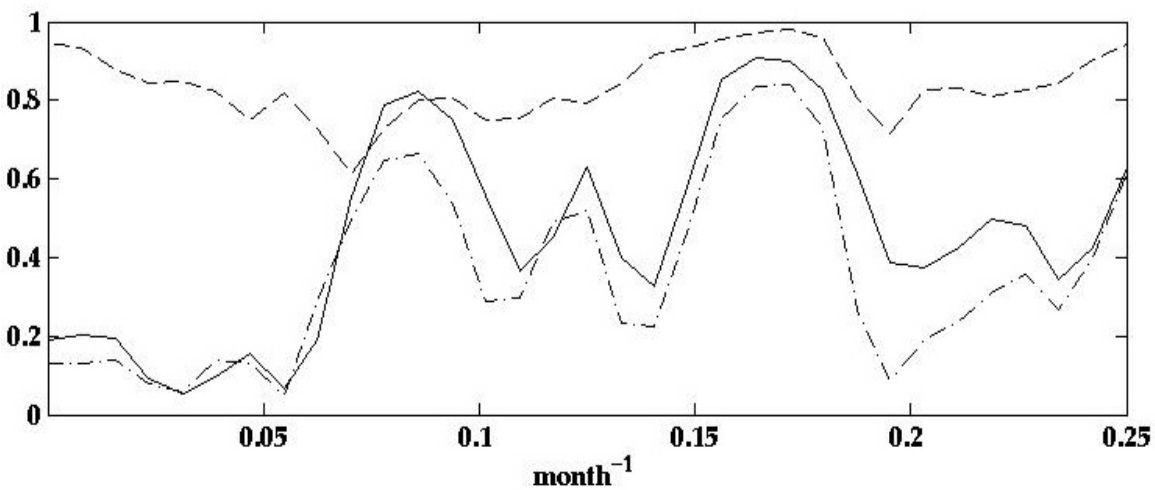


Figure 10. Coherence Function Estimate for the Entire Monthly Averaged Time Series (1948-1999) of $\mathrm{Re}\left(PC_2^\tau\right)$ and $PC_2^w$ (Solid Line), $\mathrm{Re}\left(PC_2^\tau\right)$ and $PC_2^\psi$ (Broken Line), $PC_2^w$ and $PC_2^\psi$ (Broken Dotted Line).

The circulation pattern shown for $E_2^\tau$ (Figure 11a) was dominated by a basin wide circulation centered at ~38°N/180°. Cyclonic circulation occurred in winter (January - February) and summer (May - September) when $PC_2^\tau$ was positive. During this time poleward circulation occurred in the Bering Straits and the South and East China Seas. Anticyclonic circulation occurred during the spring (March through April) and the fall (September to mid-December) while there was equatorward circulation in the Bering Straits and the South and East China Seas. Wind stress was greater in the subpolar region than in the subtropical region. The strongest wind stress was found between 45°-52°N. Seasonally, the strongest $M_2^\tau$ wind stress was in November when

$PC_2^\tau$ amplitudes approach –1.0. The negative phase of $M_2^\tau$ was stronger in fall than spring while the positive phase was stronger in the winter. Although these seasonal patterns are clear in the rotation angle and magnitude plots (Figure 10a), the winter and spring transition periods are within one standard deviation of the zero line so that the probability that the second mode will reverse in a given month was high. Periods of time that $M_2^\tau$ was statistically significant (i.e., $PC_2^\tau$ was more than one standard deviation from the zero line) were during June to August and October to mid-November.

The most striking feature of $E_2^w$ (Figure 11b) was that the subpolar and subtropical pumping regions were out of phase with midlatitude and eastern boundary regions. $M_2^w$ midlatitude pumping covered most of the interior North Pacific and was distinctly separated from the eastern boundary pumping region. $PC_2^w$ (Figure 10b) was positive for the first seven months of the year and negative for the last five months of the year. The maximum amplitude was in June and the minimum amplitude was in October and November. The resulting $M_2^w$ Ekman pumping was strongest during the fall at which time it was twice as strong as during the summer. Subpolar pumping maxima were located in the Sea of Okhotsk and the Gulf of Alaska. In these regions, $M_2^w$ pumping during the first seven months of the year was downwelling with a maximum of 4.2 cm day$^{-1}$ in June and the last 5 months of the year was upwelling with maxima during October and November averaging of 6.5 cm day$^{-1}$. A tropical maxima located in the western Pacific had a similar phase, but twice the magnitude (8.4 cm day$^{-1}$ in June and 13 cm day$^{-1}$ in October/November). The subpolar and tropical regions were coincident with active pumping regions observed in $E_1^w$ (Figure 9a) and the mean field (Figure 2b).

$M_2^w$ pumping along the eastern boundary and in regions associated with the midlatitude open ocean pumping were areas of upwelling during the first seven months of the year and downwelling during the last five months. The entire eastern boundary from the Queen Charlotte Islands to 15°N was delineated by the zero isotach. The zero isotach of $E_1^w$ (Figure 9b) and $E_2^w$ was in the same position along the eastern boundary from the Queen Charlotte Islands southward to the San Francisco Bay (Figure 11b). Along the eastern boundary, $M_1^w$ and $M_2^w$ pumping combined to enhance mean upwelling by as

much as 15 cm day$^{-1}$ from April to August and mean downwelling by as much as 12 cm day$^{-1}$ from November to mid-December.

$E_2^{\psi}$ (Figure 19c) consisted of two gyres located at the western boundary. The strongest was anticyclonic and located at 50°N. Immediately to the south, a cyclonic gyre was located at 35°N. The northern gyre was located in the subpolar gyre and the southern gyre in the subtropical gyre as defined by the mean field (Figure 2c). $PC_2^{\psi}$ had semiannual variability and was positive from mid-December to February and May to mid-September. The standard deviation exceeded the amplitude in all months except during the summer months of June, July and August. During this time, $M_2^{\psi}$ would increase the Kuroshio transport by 2.2 Sv.

## D. EOF MODE 3

The third mode had more complex spatial variability than the first and second mode. $M_3^{\tau}$ (Figures 12a, b and 13a), $M_3^{w}$ (Figures 12c and 13b) and $M_3^{\psi}$ (Figures 12d and 13c) account for 8.5%, 5.1% and 9.3 % of the total variance, respectively. The circulation pattern shown for $E_3^{\tau}$ (Figure 13a) occurred from November to March as shown by the rotation angle in Figure 12a. The winter circulation pattern was strongest in the subpolar region where flow consisted of three circulation centers, anticyclonic over the Aleutian Islands and cyclonic over Kamchatka and British Columbia. The resulting circulation was poleward along the dateline and equatorward along the coasts of Asia and North America. In the subtropics, the strongest circulation was associated with the monsoons in the Western Pacific where westward flow occurred in winter but weak cyclonic flow was centered over Hawaii and weak anticyclonic flow to the west of Baja California. This circulation pattern reverses in summer (April through September) so that in subpolar regions, equatorward winds occurred along the dateline and poleward winds along the continental margins and in the Gulf of Alaska. The wind stress was strongest during the period November through January and in May and July, when amplitudes (Figure 12a) approach 0.4. Although the seasonal patterns are clear in the rotation angle (Figure 12a), the range of plus or minus one standard deviations crosses the zero line in all months (Figure 12b) so that the third mode will reverse in a given month was high.

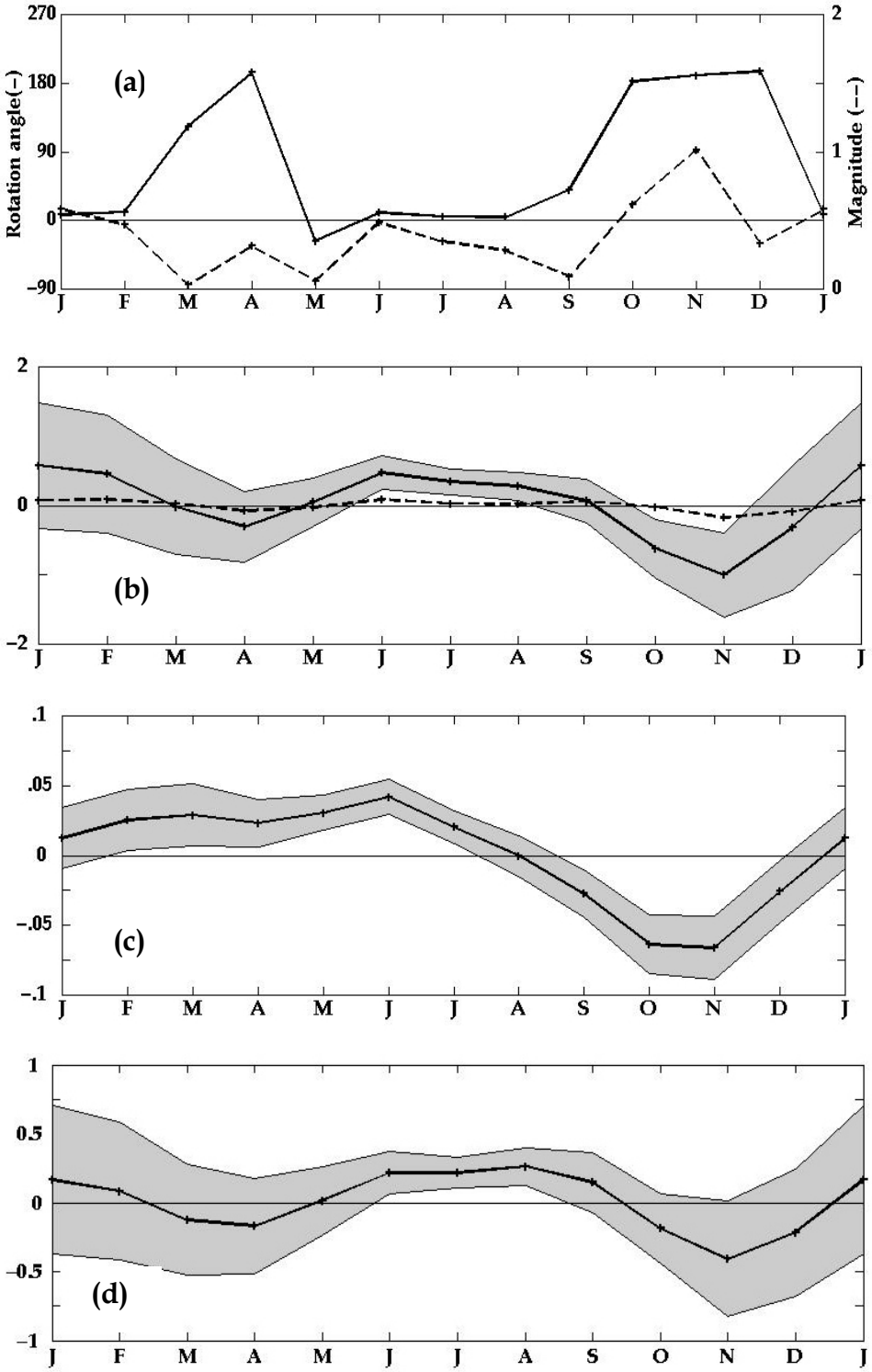


Figure 11. Seasonal Time Series of $PC_{2\overline{m}}^{X}$. (a) *rotationangle*$\left(PC_{2\overline{m}}^{\tau}\right)$ is the *Solid Line* and *magnitude*$\left(PC_{2\overline{m}}^{\tau}\right)$ is the *Broken Line* (b) $\mathrm{Re}\left(PC_{2\overline{m}}^{\tau}\right)$ is the *Solid Line* and in $\mathrm{Im}\left(PC_{2\overline{m}}^{\tau}\right)$ is the *Broken Line*. (c) $PC_{2\overline{m}}^{w}$ (d) $PC_{2\overline{m}}^{\psi}$. Shaded Region is $\pm 1\sigma$.

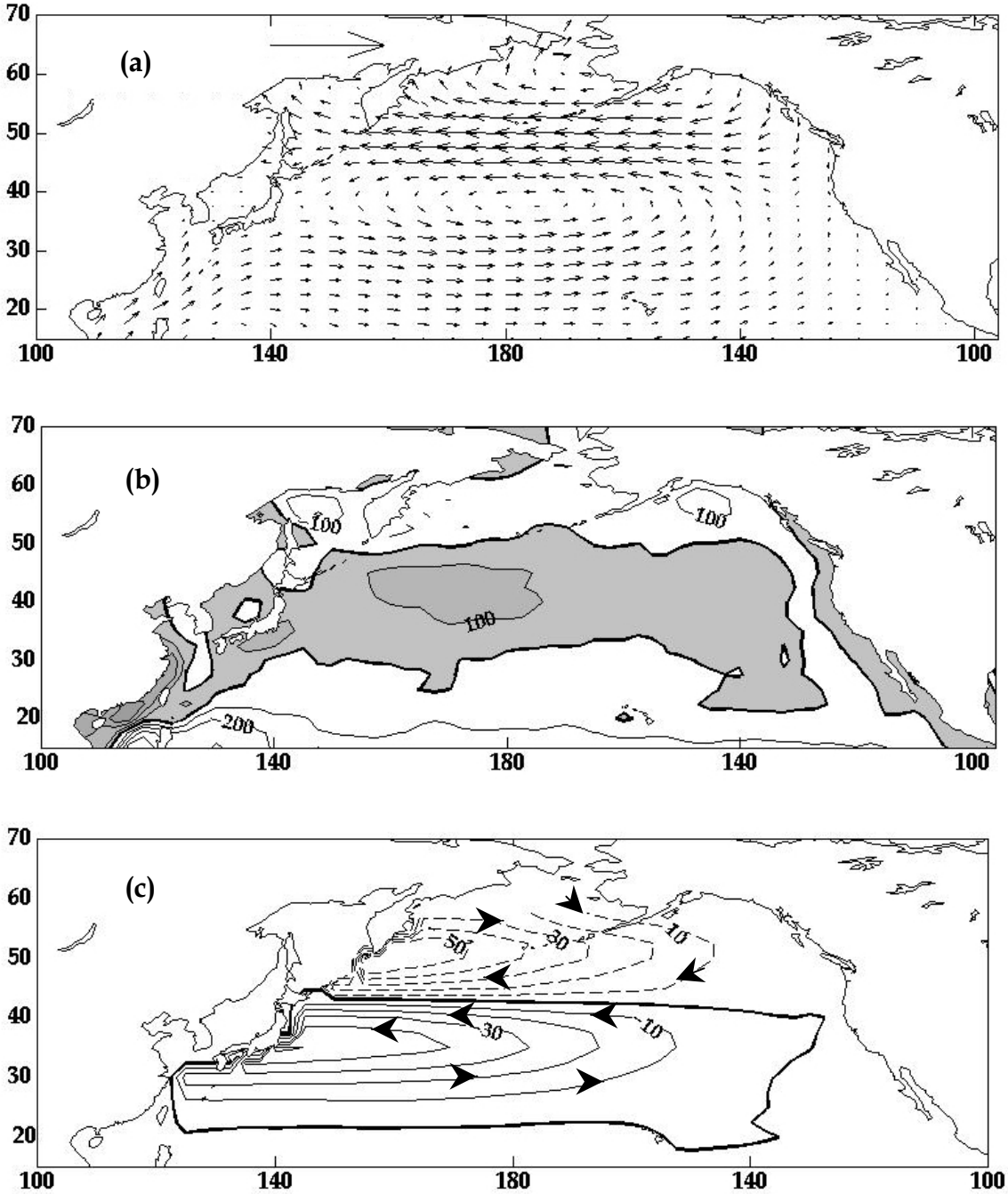


Figure 12. Eigenvector ( $E_2^X$ ) Plots. (a) $E_2^\tau$. Scaling Vector is 0.25 Pa. (b) $E_2^w$. Contour Interval is 100 cm Day$^{-1}$. (c) $E_2^\psi$. Solid Lines Indicate Negative Values. Arrowheads Indicate Direction of Transport. Zero is Denoted by the Bold Line.

At first glance, $E_3^w$ (Figure 13b) appeared related to $E_3^\tau$. $E_3^w$ (Figure 13b) was dominated by a large dipole along the dateline with downwelling north of 45°N centered

on the Aleutian Islands and upwelling to the south centered at about 38°N. Along the eastern and western boundaries, this pattern reversed with downwelling in the subpolar region and upwelling in the subtropics but the Western Pacific was more complex and the downwelling area along 28°N extended eastward, almost reaching the dateline. A small dipole also existed in the region of the Hawaiian Islands; however the variability of $PC_3^w$ (Figure 12b) was semiannual (compared to the annual variability of the rotation angle for $PC_3^\tau$) and was positive in January and February and from July through October. The maximum amplitude (0.04) occurred in January and minimum amplitude in April (-0.04). As for $PC_3^\tau$, the standard deviation of $PC_3^w$ (Figure 12c) was equal to or exceeded the amplitude in each month, except in August.

$E_3^\psi$ (Figure 13c) consisted of four gyres. The strongest was cyclonic and located at the western boundary at 56°N. Immediately to the south, an anticyclonic gyre was centered at 48°N, 170°W. Both of the northern gyres were located within the subpolar gyre as defined by the mean field (Figure 2c). Two weaker gyres occurred farther south within the subtropical gyre, cyclonic at 34°N and anticyclonic at 20°N. $PC_3^\psi$ (Figure 12c) had annual variability and was positive from October to March and negative the rest of the time. Maximum amplitude (0.025) occurred in February and minimum amplitude (-0.04) in July. The standard deviation of $PC_3^\psi$ exceeded the amplitude in all months except July. In July, $M_3^\psi$ would increase the Kuroshio transport by 1.2 Sv.

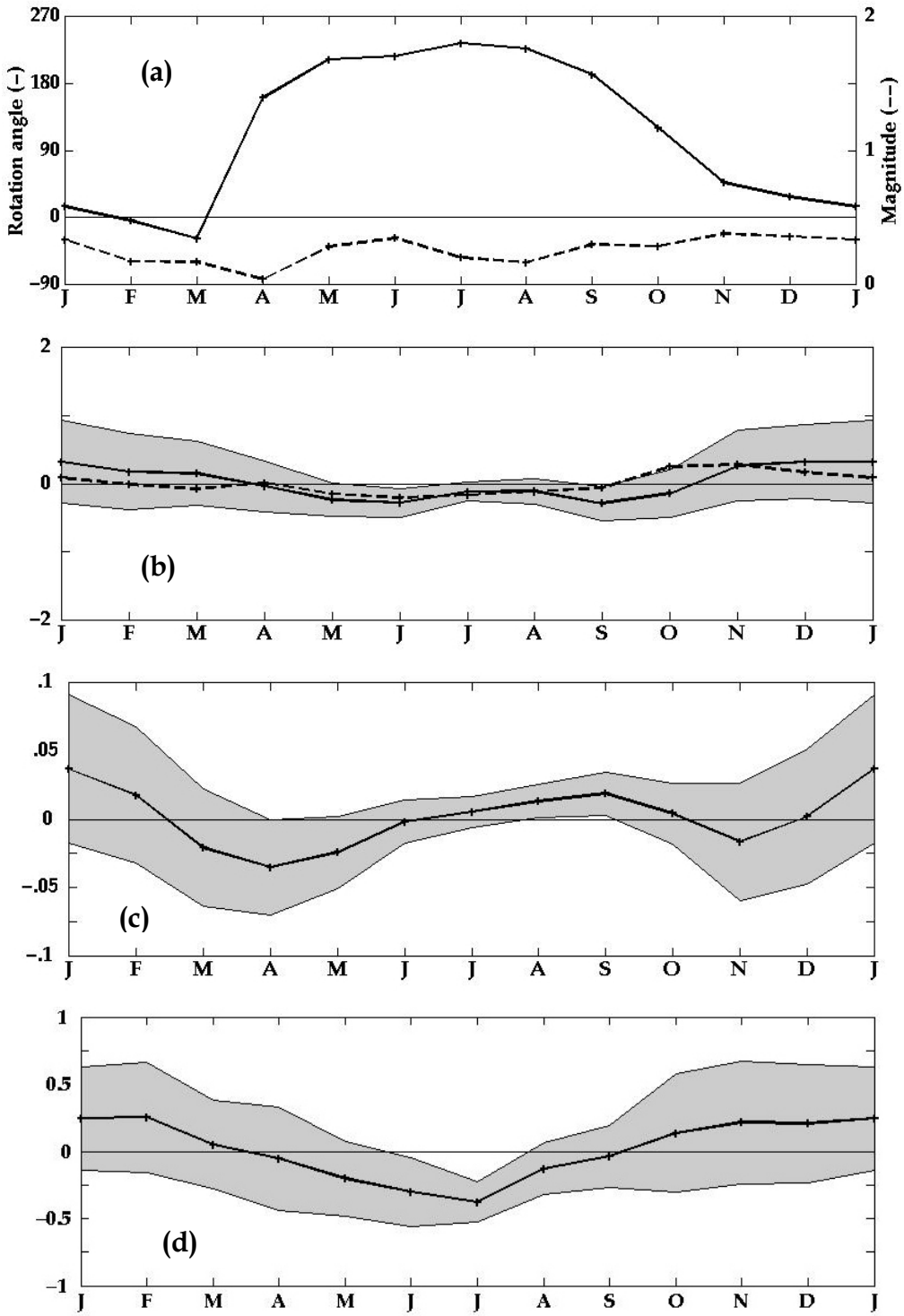


Figure 13. Seasonal Time Series of $PC^{X}_{3\overline{m}}$. (a) *rotationangle*$\left(PC^{\tau}_{3\overline{m}}\right)$ is the *Solid Line* and *magnitude*$\left(PC^{\tau}_{3\overline{m}}\right)$ is the *Broken Line* (b) $\mathrm{Re}\left(PC^{\tau}_{3\overline{m}}\right)$ is the *Solid Line* and $\mathrm{Im}\left(PC^{\tau}_{3\overline{m}}\right)$ is the *Broken Line*. (c) $PC^{w}_{3\overline{m}}$ (d) $PC^{\psi}_{3\overline{m}}$. Shaded Region is $\pm 1\sigma$.

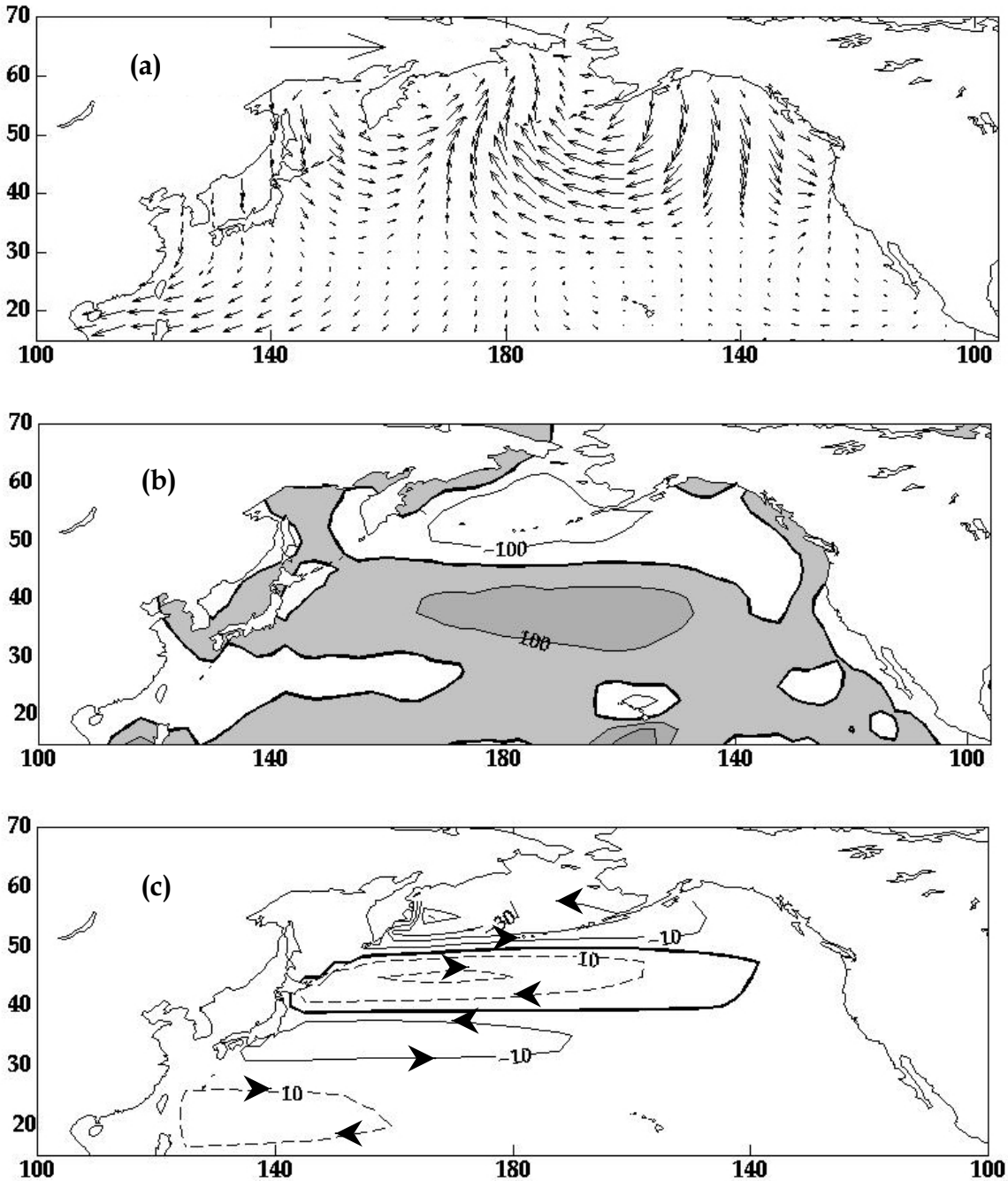


Figure 14. Eigenvector ( $E_3^X$ ) Plots. (a) $E_3^\tau$. Scaling Vector is 0.25 Pa. (b) $E_3^w$. Contour Interval is 100 cm Day$^{-1}$. (c) $E_3^\psi$. Solid Lines Indicate Negative Values. Arrowheads Indicate Direction of Transport. Zero is Denoted by the Bold Line.

# IV. DISCUSSION

This section will demonstrate that the annual variability can reasonably be described using just the first three EOF modes. The benefit in using a minimal number of modes to explain annual variability is that the complex overlapping patterns modulated in time and space are reduced to a fewer number of features (from the eigenfield spatial plots) with a seasonal amplitude (from the principal components).

$M_1^{\tau,w,\psi}$ contains the largest amount of total variance of the annual cycle. $PC_1^{\tau,w,\psi}$ had an annual cycle that can be described as two seasons (winter and summer) that last for five months each separated by two rapid (approximately one month) transition periods (spring and fall). North Pacific (NP) winter occurred during the positive phase of $PC_1^{\tau,w,\psi}$ (November thru March) and summer during the negative phase (May thru September). The transitional periods occurred about the month related to the zero line crossings, April and October for the spring and fall, respectively. Therefore, seasons were designated based on $PC_1^{\tau,w,\psi}$ amplitudes and zero line crossings.

Individual months were selected to represent typical seasonal circulations rather than averaging several months within a season. Selecting individual months provided a truer representation of actual seasonal circulation patterns and magnitudes at smaller scales which may have been smoothed out through averaging. The selection criteria was based on the minimum and maximum amplitudes of $PC_1^{\tau,w,\psi}$ and where the zero line crossings occurred. Maxima $PC_1^{\tau,w,\psi}$ amplitudes occurred in January, which was selected as the month representative of winter. Although the minima for $PC_1^{\tau}$, $PC_1^{w}$, and $PC_1^{\psi}$ occurred at different times of the year (July, August and September, respectively), August was selected as the month representative of summer. The rationale behind choosing August, other than it was the median month among the three circulations, was that the August value was within one standard deviation of the true minima for each circulation, and therefore only magnitude, not phase, would be slightly affected and remain within statistical tolerance. The same logic was used for choosing April and October as the spring and fall transition months, respectively. Monthly means

representative of the winter season (a), spring transition (b), summer season (c) and fall transition (d) are shown for wind stress, Ekman pumping and Sverdrup transport in Figures 15, 19 and 23, respectively.

This discussion contains three sections, a. Wind stress, b. Ekman pumping and c. Sverdrup transport. Each section will contain a discussion of the annual cycle using a monthly mean representative of the two seasons and two transition periods, quantify how well $M_{1-3}^{\tau,w,\psi}$ account for the seasonal variability and examine a regional example to demonstrate how the PCs replicate the annual cycle. Lastly, the interannual variability of the PCs is compared to environmental indices.

## A. WIND STRESS

Monthly means for the winter season (a), spring transition (b), summer season (c) and fall transition (d) for wind stress are shown in Figure 15. The annual cycle of North Pacific wind stress is dominated by variations in intensity and meridional movement of the subpolar Aleutian low and subtropical North Pacific high. The Aleutian low generates cyclonic wind stress and dominates North Pacific circulation in winter. The North Pacific subtropical high generates anticyclonic wind stress that dominates the summer circulation. Each circulation system has its own annual cycle in the North Pacific and is considered separately below.

The strongest monthly mean cyclonic wind stress occurs during the winter in the subpolar region and is centered about 50°N, 170°E (Figure 15a). Cyclonic wind stress occurs over the North Pacific north of 27°N from the eastern to the western boundaries. This wind stress circulation pattern diminishes in magnitude and geographical extent throughout the year, becoming centered over Alaska during the spring transition (Figure 15b), and disappearing completely in the summer (Figure 15c). It and re-develops over Alaska, east of its winter position, during the fall transition (Figure 15d).

The annual cycle of the subtropical anticyclonic wind stress shows moderate wind stress centered about 30°N, 130°W in the winter (Figure 15a). This circulation becomes centered at about 32°N, 170°W and expands basin-wide during the spring (Figure 15b), intensifying equatorward wind stress along the eastern boundary in the California Current System (CCS). During summer the circulation pattern becomes centered about 40°N,

145°W (Figure 15c). Strong equatorward windstress continues in the CCS; however, windstress in the western Pacific subsides and becomes poleward. During the fall transition, a ridge develops connecting eastern and western anticyclonic centers about 35°N, 140°W and 35°N, 175°E (Figure 15d) which create westward stress in the subtropics and eastward stress in the subpolar regions.

The wind stress patterns are similar to each other during both spring and fall (Figures 15b and 15d). There is strong anticyclonic circulation over most of the North Pacific basin centered about 30°N and weak cyclonic circulation centered over Alaska. Eastward wind stress is found in the subpolar regions and westward wind stress is found in the subtropical regions. A nearly zonal band of strong eastward wind stress centered about 45°N is observed when cyclonic and anticyclonic circulation centers exist concurrently in the eastern North Pacific. In the eastern North Pacific, the wind stress gradient is strongest between 35°-55°N at 140°W between the centers of these two different circulation systems.

At smaller scales there are regional differences between the spring and fall. Most notably, anticyclonic wind stress circulation during spring (Figure 15b) appears as a single coherent pattern that is centered about 32°N, 170°W. Although the fall (Figure 15d) also exhibits a large scale anticyclonic mean circulation across most of the basin, it appears to be a composite of two separate anticyclonic circulation systems centered at 35°N, 170°E and 35°N, 140°W. Additionally, in the western North Pacific, strong northeastward wind stress is centered around 40°N during the spring and during the fall eastward windstress is centered around 50°N and across the Sea of Okhotsk. Equatorward wind stress along the eastern boundary is more intense during the spring than during the fall.

Winter and summer are distinctly different. Winter has two distinct circulation centers present and strong southward monsoonal wind stress while summer shows near uniform anticyclonic circulation over most of the North Pacific and northward monsoonal wind stress. The annual cycle of the windstress in the monsoon region is discussed below.

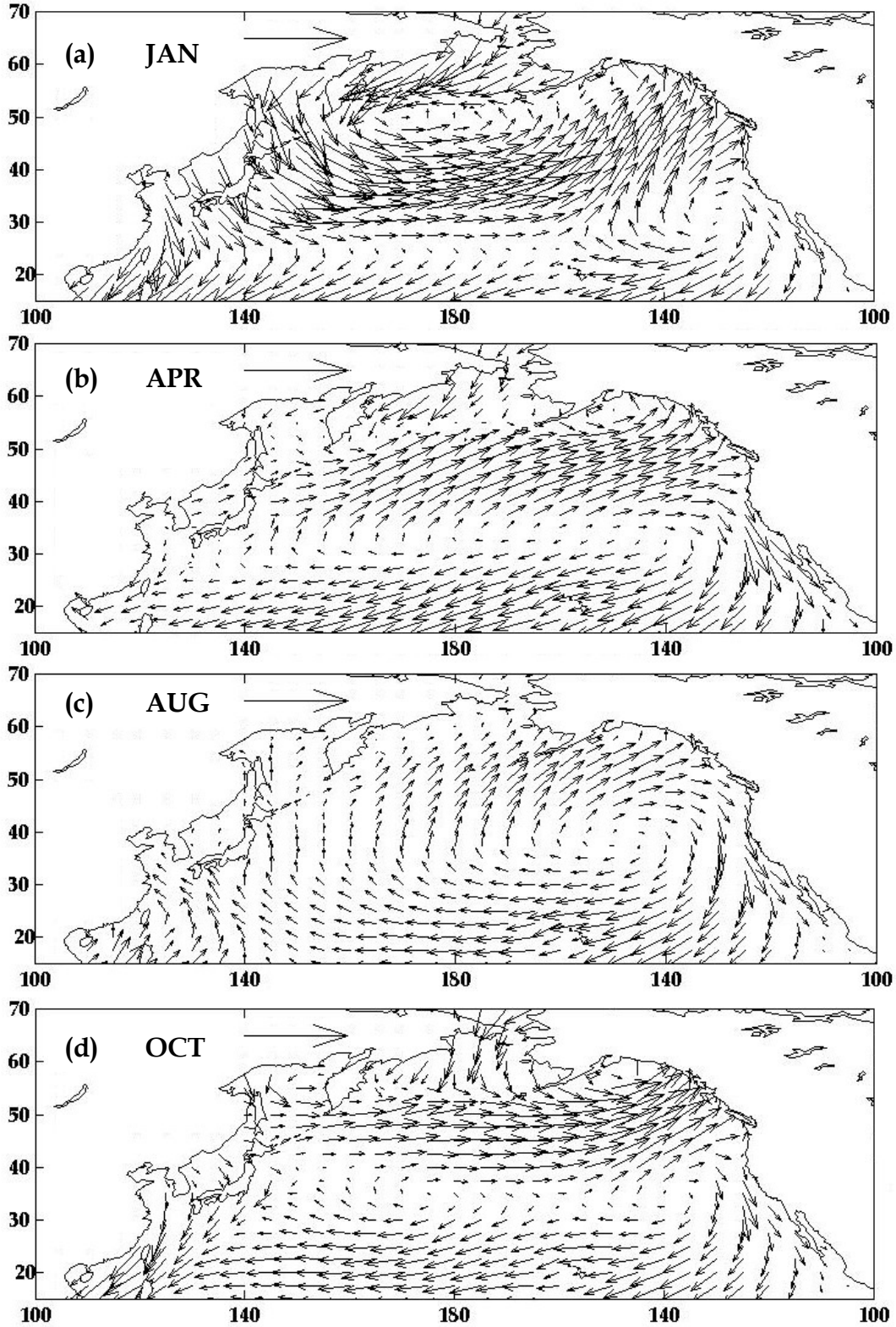


Figure 15. Monthly Mean Wind Stress (Pa). Scaling Vector is 0.25 Pa.

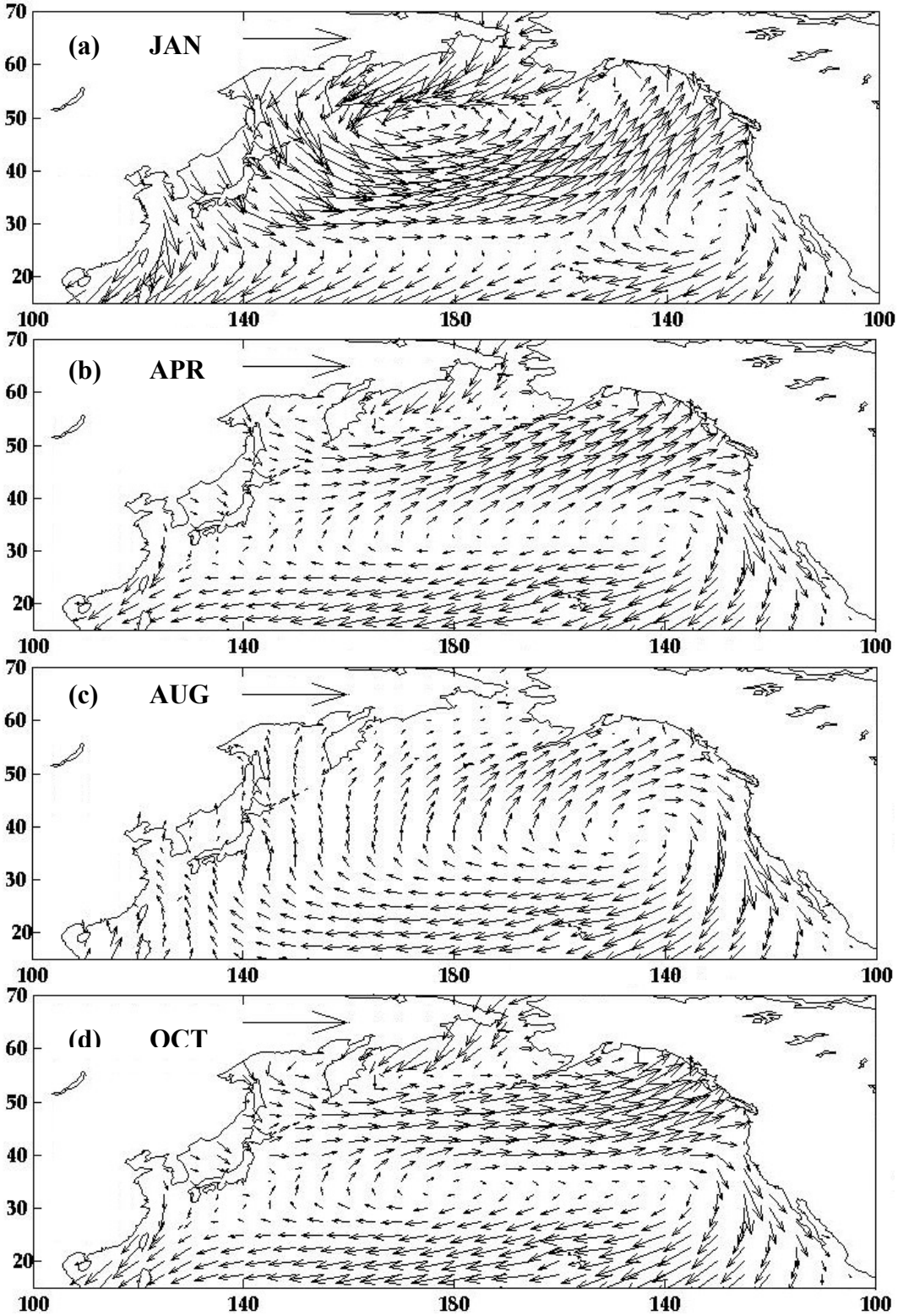


Figure 16. $M^{\tau}_{1,2,3} + \overline{X}$ for the Months Indicated. Scaling Vector is 0.25 Pa.

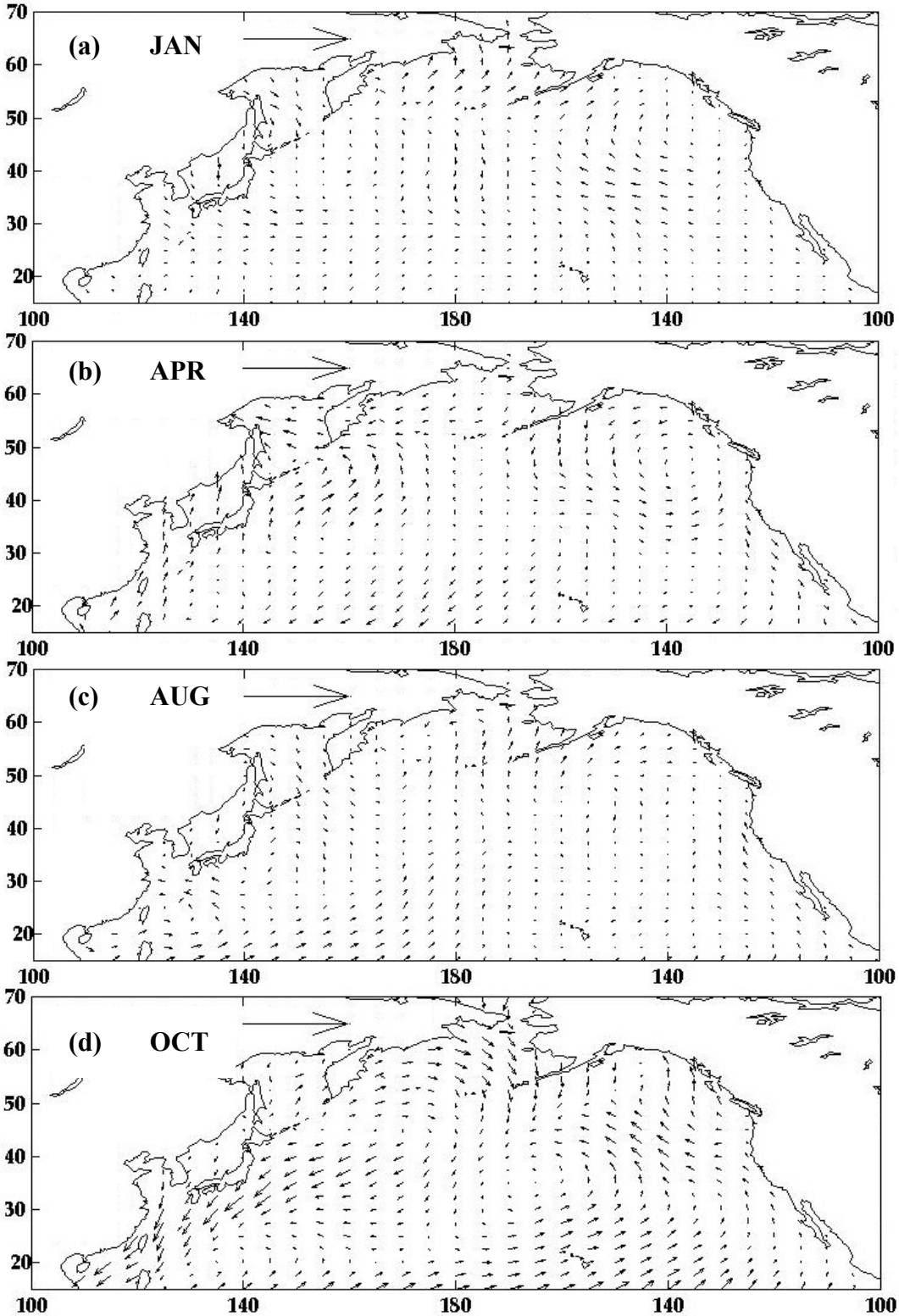


Figure 17. $M^{\tau}_{1,2,3}$ Residuals for the Months Indicated. Scaling Vector is 0.25 Pa.

Maximum eastward stress occurs in the western and central Pacific between 30°-45°N during the winter (Figure 15d), averaging 0.18 Pa. Maximum equatorward wind stress in the CCS occurs during spring, averaging 0.15 Pa. (Figure 15b). The weakest basin-wide mean scalar wind stress field magnitude occurs during the summer (0.03 Pa) (Figure 15c) and the strongest during the winter (0.07 Pa) (Figure 15a).

The sums of $M^{\tau}_{1,2,3} + \overline{X}$ (annual mean) for January, April, August, and October are shown in Figure 16. The difference between the vector components of the monthly mean and $M^{\tau}_{1,2,3} + \overline{X}$, termed $M^{\tau}_{1,2,3}$ residuals, is shown in Figure 17 and was used as a quantitative measure of replicability of seasonal wind stress. Upon visual inspection of Figures 15 and 16, the three modes accounting for 57.9% of the total variance fairly replicates the main physical features discussed above. Spring (Figure 17b) and fall (Figure 17d) have larger residuals than winter (Figure 17a) and summer (Figure 17c). This is in part due to the contribution of mode 1, which accounts for 34.5% of the total variance, being near zero at these times. This implies the higher modes may account for much of the transitional period variability. Regions of large deviation (in parenthesis) occur in the Bering Sea (0.04 Pa), the western Pacific (0.06 Pa), the Gulf of Alaska (0.04 Pa), and the trade wind regions (0.05 Pa) during the spring and fall. This deviation is accounted for in the higher modes, especially $M^{\tau}_{4}$ and $M^{\tau}_{5}$ (Appendix D).

Two wind stress time series for the northwest Pacific are shown in Figure 18. Geographic boundaries are $0^{o}$-$50^{o}$N and $100^{o}$-$160^{o}$E for both time series. Data limits are $15^{o}$-$50^{o}$N and $100^{o}$-$160^{o}$E to correspond with the established EOF analysis limits. Wind stress is computed on a $2.5^{o}$ grid and plotted on a $5^{o}$ grid for resolution of the wind stress vectors.

The Aleutian low is fully developed during the winter, generating large cyclonic wind stress over much the western North Pacific. The Asian winter high extends over much of the ocean and produces a wind reversal over the East and South China Seas and the region east of the Philippines; these regions thus experience monsoonal climate, with Northeast Monsoon during winter (December – March) and Southwest Monsoon during summer (June – September).

$PC_1^\tau + \overline{X}$ replicates the monthly means throughout the annual cycle well even though $PC_1^\tau$ accounts for only 34.5% of the total variance of the wind stress. During the periods of May-August, $PC_1^\tau + \overline{X}$ does not have the same direction as the monthly mean although the magnitude of the wind stress is similar. This is also reflected in the residual plots (Figure 17) and may indicate that higher modes are important during this time. Fall and winter $PC_1^\tau + \overline{X}$ wind stress show similar direction, but with a lesser magnitude. This is also apparent in the residual plots.

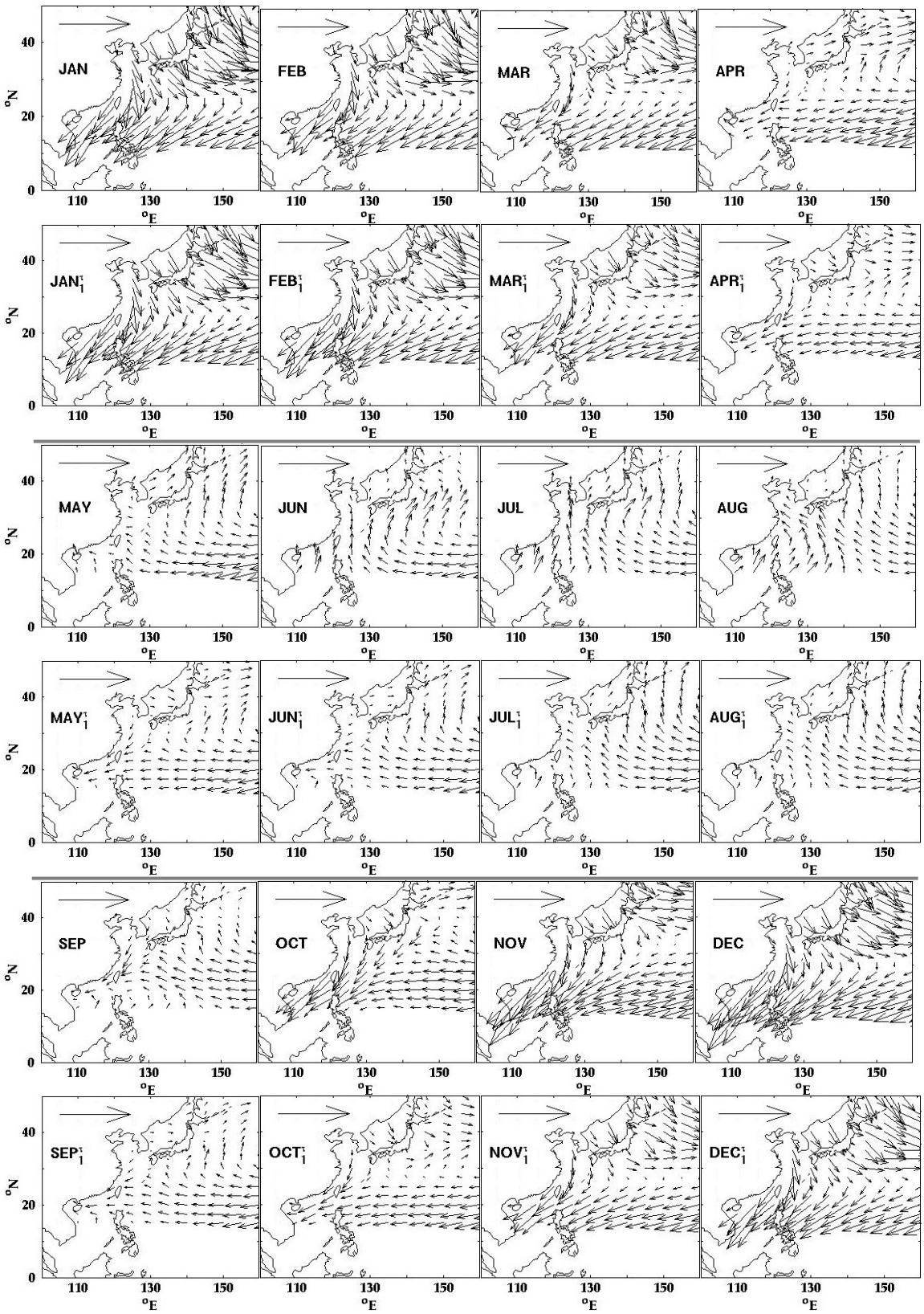


Figure 18. Monsoon Wind Stress Monthly Means (Top Row) and $PC_1^\tau + \overline{X}$ (Bottom Row). Units are Pascals (Pa = kg m$^{-1}$ s$^{-2}$). Scaling Vector is 0.25 Pa.

## B. EKMAN PUMPING

Since wind stress on the ocean surface varies in time and space, so does the Ekman transport. Diminishing cyclonic wind stress and expanding anticyclonic wind stress from winter to summer results in a general seasonal northward movement of the zero isotach (Figures 19a, b, c). The zero isotach is at its southernmost limit (~32°N) in the western and central Pacific during winter (Figure 19a) and its northernmost limit (~50°N) during summer (Figure 19c). The mean upwelling value for the region north of the zero isotach is greatest (~5.9 cm day$^{-1}$) in the winter and weakest in the summer (~1.4 cm day$^{-1}$).

Sub-basin scale upwelling maxima in the Gulf of Alaska and near the Kamchatka peninsula persist throughout the year, but are strongest (> 15 cm day$^{-1}$) when cyclonic wind stress generated from the Aleutian low is present during winter (Figure 19a) and fall (Figure 19d). A distinctive tilt of the zero isotach occurs in the Gulf of Alaska during the winter when the Aleutian Low is centered west of the dateline. Weak (< 5 cm day$^{-1}$) small-scale coastal downwelling also occurs off Oregon, Washington and British Columbia during these seasons.

A small-scale upwelling feature near the Hawaiian Islands (20°N, 160°W), that is also apparent in other climatologies (Trenberth *et al*., 1990; Chelton *et al*., 1990; Hellerman and Rosenstein, 1983), persists throughout the year and is due to changes in both wind speed and direction (Figures 15a-d). The formation of a dipolar upwelling-downwelling structure in the summer (Figure 19c) and fall (Figure 19d) has been noted and discussed in other studies (Trenberth *et al*., 1990; Harrison, 1989).

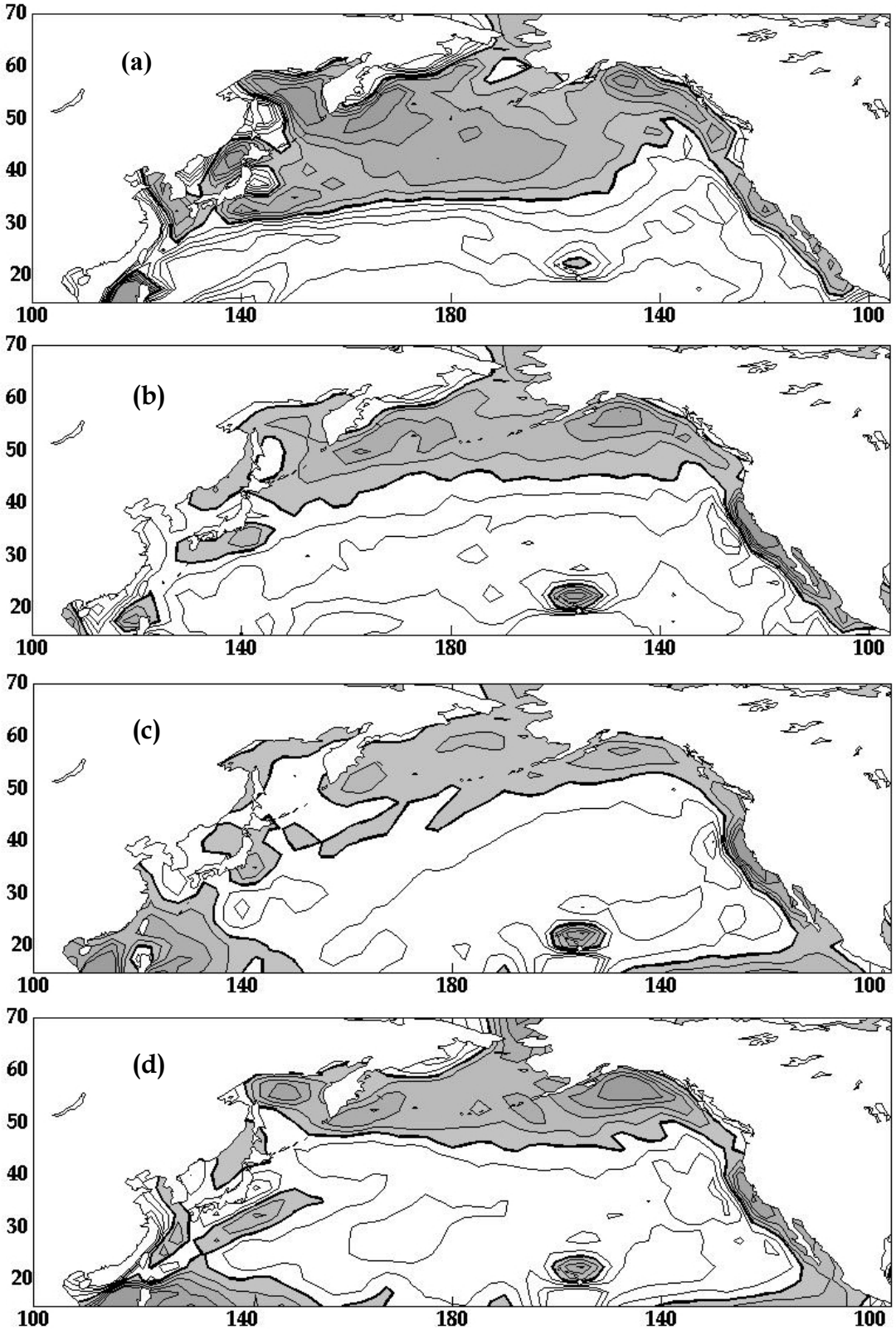


Figure 19. Monthly Mean Ekman Pumping. The Zero Isotach is Bold. The Contour Interval is 5 cm day$^{-1}$. Upwelling Regions are Shaded.

The CCS is dominated by intense equatorward alongshore (upwelling favorable) wind stress during the spring into the summer and fall (Figures 15b-d). Coastal upwelling in the CCS is most intense (> 15 cm day$^{-1}$) off the California and Baja coasts during the spring (Figure 19b). The active upwelling region covers the largest zonal range in summer (Figure 19c), extending from British Columbia to the Baja Peninsula. In summer, areas with upwelling rates greater than 15 cm day$^{-1}$ are located from Oregon to the central California.

This upwelling favorable wind stress is associated with anticyclonic curl offshore of the coastal upwelling zone in the CCS (Figure 15). The pairing of coastal cyclonic curl and offshore anticyclonic curl results in the development of a dipolar upwelling-downwelling structure (30°-45°N, 120°-135°W) (Figure 20). This dipole oscillates north and south seasonally about 35°N. The dipole feature intensifies as it moves northward through the spring transition and summer. The dipole is strongest and at its northernmost limit (~ 45$^{o}$N) in July and at its southernmost limit (~ 32$^{o}$N) in December thru February.

The offshore downwelling feature tracks the northward movement of the upwelling maximum and intensifies at the same time. The upwelling portion of the dipole is most intense in the months of June and July (summer), averaging about 35 cm day$^{-1}$, and least intense from December through February (winter), averaging about 15 cm day$^{-1}$. The downwelling portion of the dipole is most intense during June and July also, averaging 25 cm day$^{-1}$. This feature averages about 15 cm day$^{-1}$ from August through March and 20 cm day$^{-1}$ during April and May.

The implication of all this is that the seasonal evolution of coastal upwelling relates to the large-scale evolution of the wind field over the North Pacific. Also the onset of spring transition is due to the variability in seasonal transition from an Aleutian low to a North Pacific high dominance.

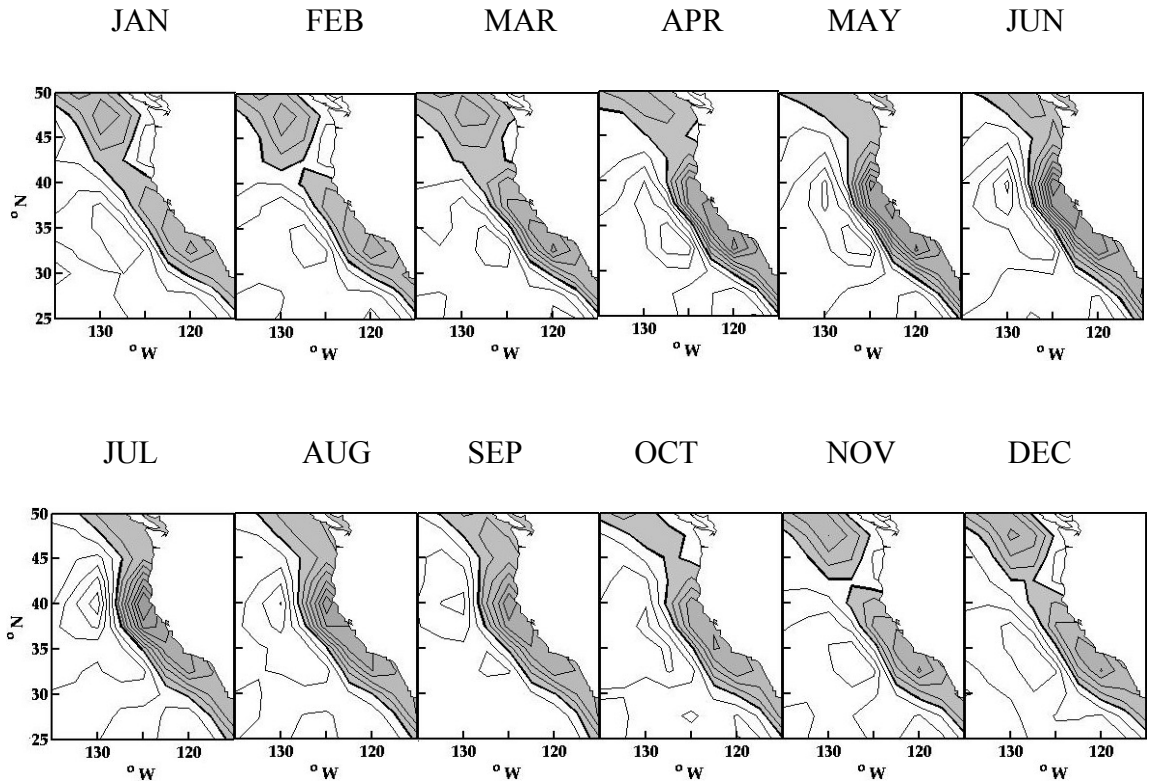


Figure 20. Monthly Mean Ekman Pumping or Vertical Velocity at the Base of the Ekman Layer as a Result of Divergence of the Ekman Transport Computed for the Period 1948-1999. The Contour Interval is 5 cm day$^{-1}$. Zero Isotach is Bold. Upwelling Regions are Shaded. Geographic Limits As Shown.

The sum of $M^{w}_{1,2,3}$ + $\overline{X}$ (annual mean) for January, April, August, and October are shown in Figure 21. The difference between the monthly mean and $M^{w}_{1,2,3}$ + $\overline{X}$, termed $M^{w}_{1,2,3}$ residuals, is shown in Figure 22 and was again used as a quantitative measure of replicability. The three modes, accounting for only 38.5% of the total variance, replicate the main physical features discussed above to within 5 cm day$^{-1}$. The CCS dipole, the Hawaii Island dipole and active upwelling centers are well replicated. The winter tilt of the zero isotach, sloping northeastward east of 155°W, is well replicated also.

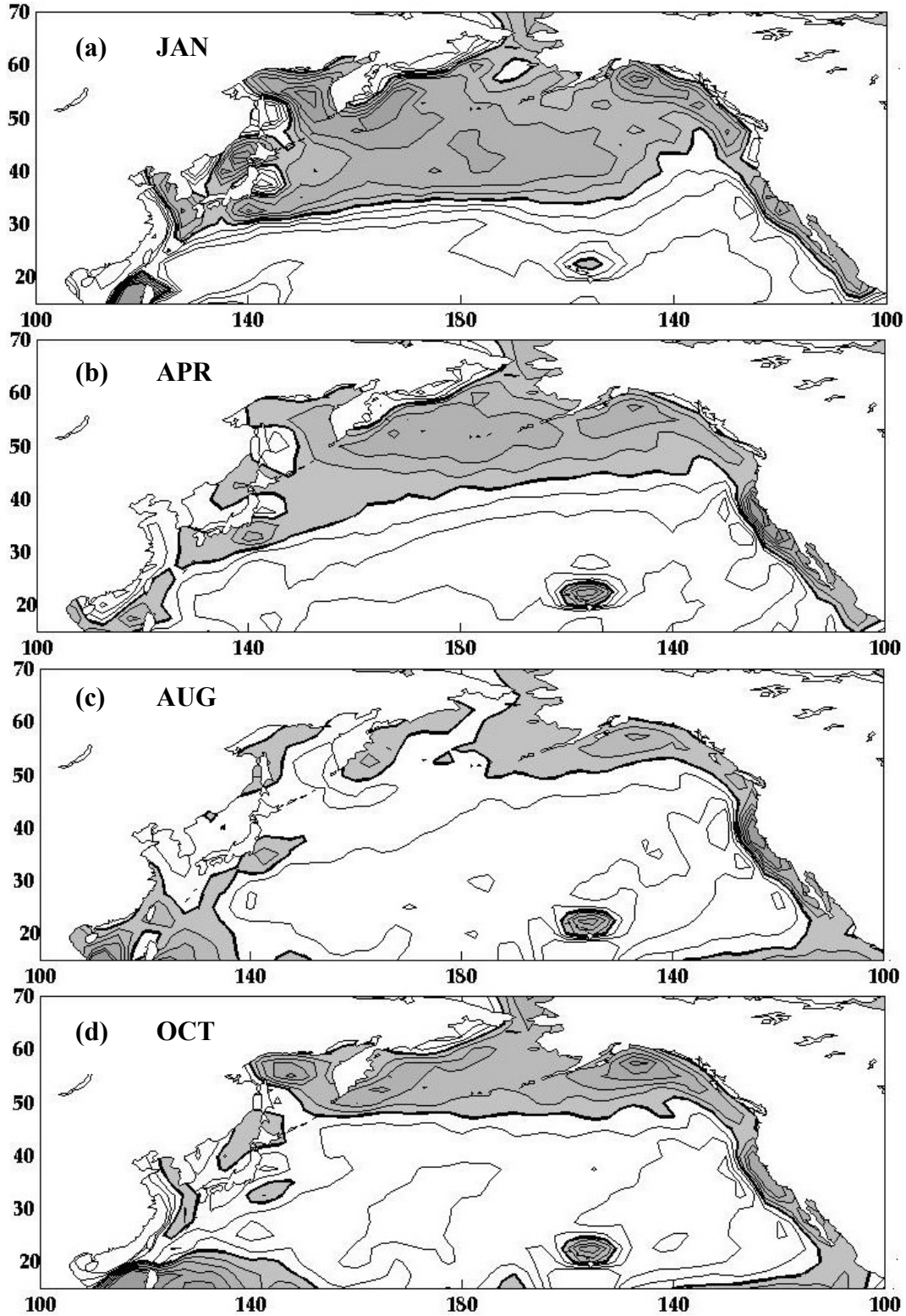


Figure 21. $M^{w}_{1,2,3} + \overline{X}$ for the Months Indicated. The Zero Isotach is Bold. The Contour Interval is 5 cm day-1. Upwelling Regions are Shaded.

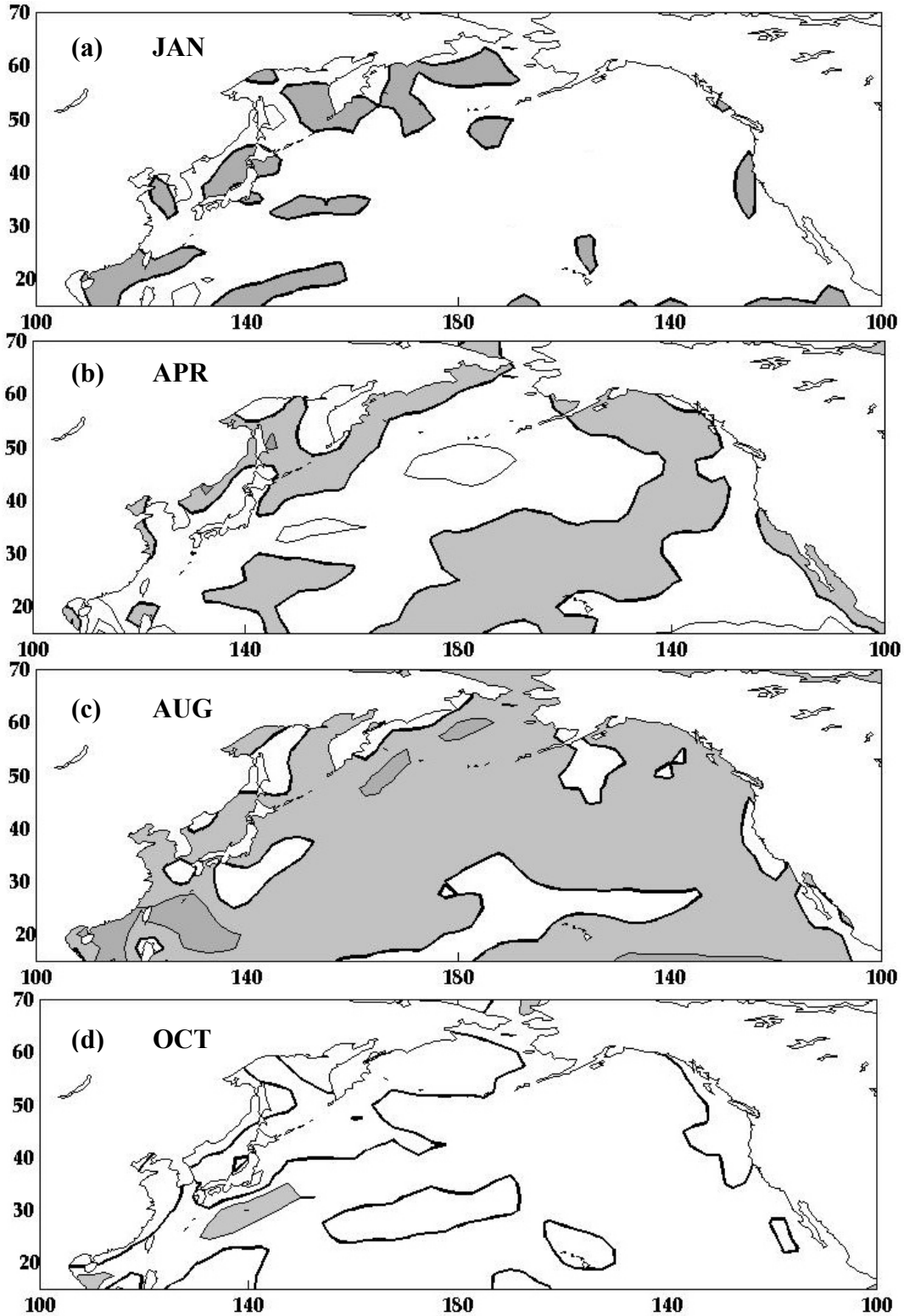


Figure 22. $M^{w}_{1,2,3}$ Residuals for the Months Indicated. The Zero Isotach is Bold. The Contour Interval is 5 cm day$^{-1}$. Positive Values (Shaded Regions) Indicate Area where the Seasonal Mean is Greater.

## C. SVERDRUP TRANSPORT

The total ocean transport based on the Sverdrup relation (Sverdrup, 1947; Pedlosky, 1987) is used as a measure of the oceanic response to atmospheric forcing, rather than a true reflection of the actual currents. Calculations of the Sverdrup transport are meaningful when the forcing is slowly varying, relative to the internal adjustment time of the ocean, i.e. the assumption of a steady state is valid. The reliability of this assumption decreases with increasing latitude. Even when the wind stress varies with time, it must be assumed that the ocean is always in near-equilibrium, namely the Sverdrup balance (Kutsuwada, 1988).

Monthly means representative of the winter season (a), spring transition (b), summer season (c) and fall transition (d) for Sverdrup transport are shown in Figure 23. The calculated transports are in general agreement with Trenberth et al. (1990) and Hellerman and Rosenstein (1983) (Table 3). Differences arise due to the different drag coefficients and wind data sets used.

Seasonal variations in the wind stress change the strength of the subpolar and subtropical gyres substantially (Trenberth et al., 1990). The annual mean eastward transport derived from NCEP winds is 80 Sverdrups (Figure 2c). The gyres are strongest in northern hemisphere winter (Figure 23a) and weakest in summer (Figure 23c). Seasonal variations range from 128 Sv in January to around 56 Sv in August. The circulation of the North Pacific subpolar gyre decreases from 57 to 33 Sv (-42%) and the subtropical gyre decreases from 71 to 23 Sv (-68%) accounting for most of the decrease in the eastward transport.

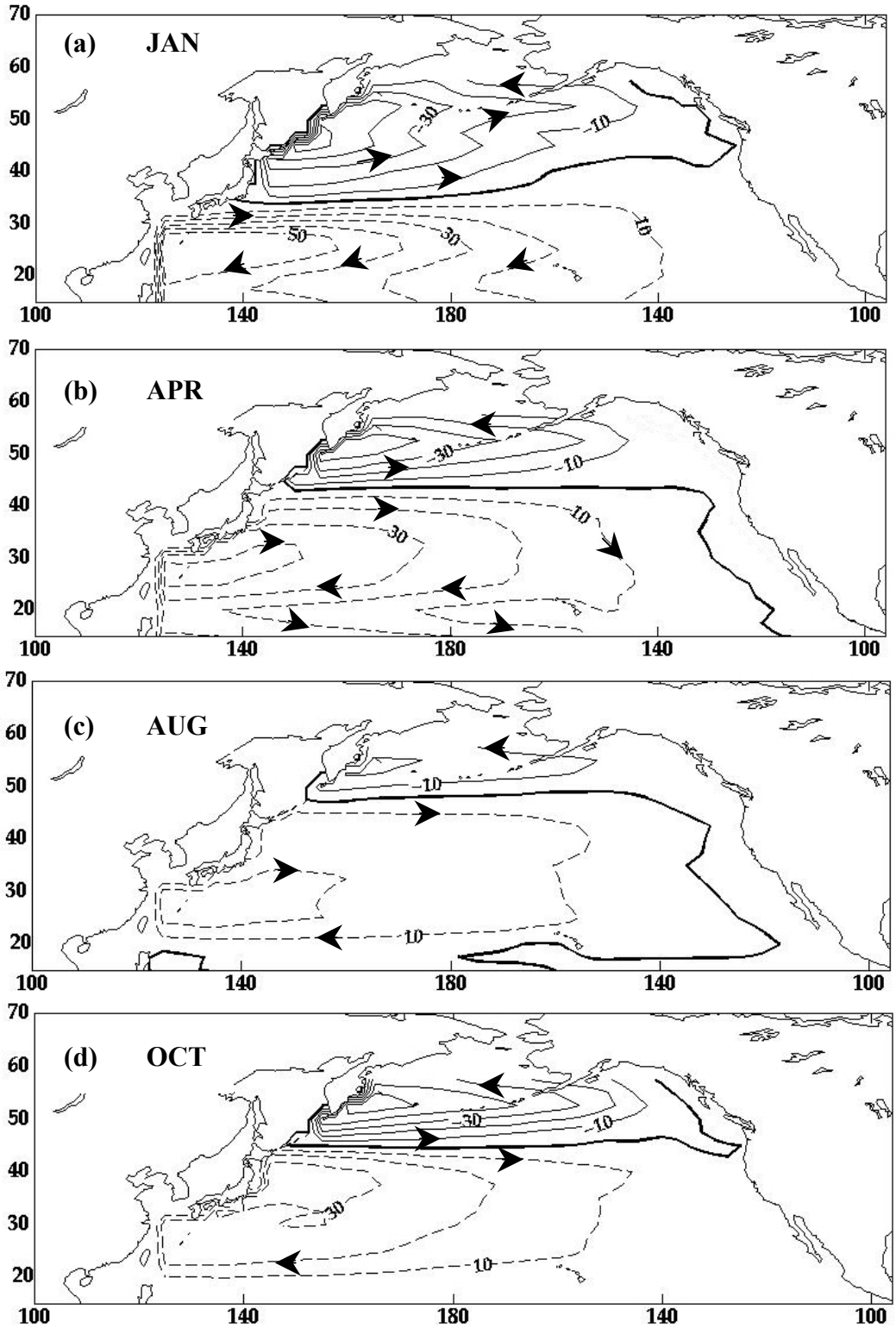


Figure 23. Streamlines of Monthly Mean Sverdrup Transport. Zero is Bold. Arrowheads Indicate the Direction of the Transport. Positive Values are Dashed Lines. Zero Line is in Bold. Contour Interval is 10 Sverdrups (1 Sv ≡ $10^6$ $m^3$ $s^{-1}$).

| | Winter | | | Summer | | | Annual | | |
|---|---|---|---|---|---|---|---|---|---|
| | **NCEP** | **EC** | **HR** | **NCEP** | **EC** | **HR** | **NCEP** | **EC** | **HR** |
| **Northward Transport** | | | | | | | | | |
| Subpolar gyre | -57 | -75 | -55 | -33 | -25 | -10 | -40 | -50 | -35 |
| Subtropical gyre | 71 | 100 | 100 | 23 | 40 | 45 | 40 | 60 | 60 |
| **Eastward Transport** | | | | | | | | | |
| North Pacific | 128 | 175 | 155 | 56 | 65 | 55 | 80 | 110 | 95 |

Table 3. North Pacific Transports (Sv) Values based on NCEP Wind Stress Forcing from 1948-1999 for Winter (February) and Summer (September). For Comparison, Transports from Two Other Studies for Winter (January) and Summer (July) are Shown. Sources are Trenberth Et Al. (1990), Derived from ECMWF (EC) and Hellerman and Rosenstein (HR) Wind Climatologies.

The sum of $M^{w}_{1,2,3}$ + $\overline{X}$ (annual mean) for January, April, August, and October are shown in Figure 24. The $M^{w}_{1,2,3}$ residuals are not shown as the residual values are less than 10 Sv for each of the four months. In other words, the first three modes, accounting for only 74.6% of the total variance, replicate the main physical features discussed above to within 10 Sv.

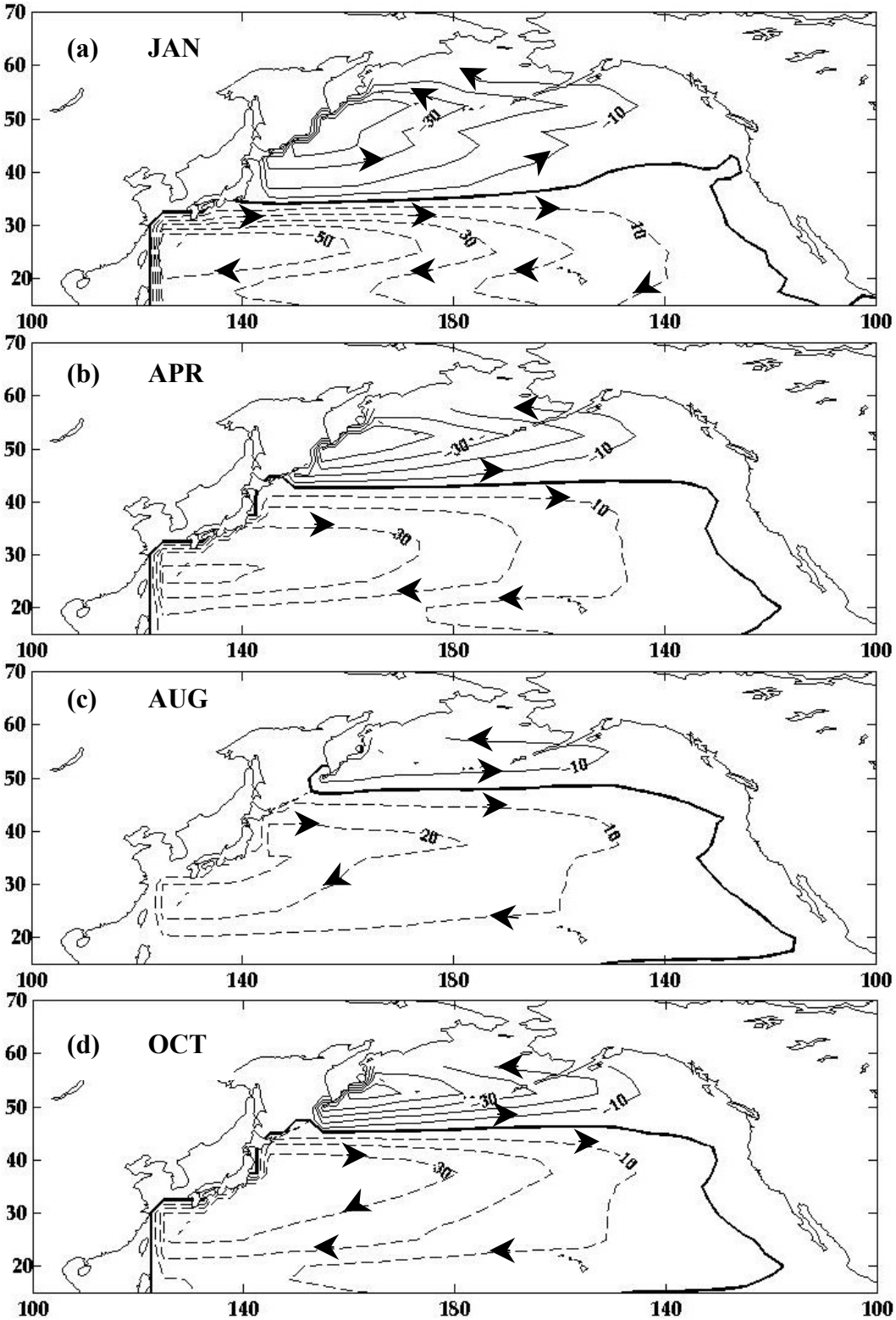


Figure 24. $M^{\psi}_{1,2,3} + \overline{X}$ Streamlines for the Months Indicated. Arrowheads Indicate the Direction of the Transport. Positive Values are Dashed Lines. Contour Interval is 10 Sverdrups (1 Sv ≡ $10^6$ $m^3$ $s^{-1}$). Zero Line is in Bold.

While the Sverdrup relation does not replicate the western boundary current (i.e. the Kuroshio current), it is assumed that the transport of the mid-latitude anticyclonic gyre must be balanced by a western boundary current. The circulation inferred from the streamfunctions in the subtropics gives rise to the Kuroshio as the return flow. The Kuroshio transport is defined as the total eastward flow north of 30°N (Qiu and Joyce, 1992). This transport is composed of a barotropic (Sverdrup) and baroclinic (geostrophic) components. The Kuroshio transport has a large seasonal signal (Sekine and Kutsuwada, 1994), with maximum baroclinic transport in the summer; the maximum Sverdrup transport calculated from the winds occurs in winter.

Kutsuwada (1988) suggests that another way to derive the Kuroshio transport is to estimate it from sea level data at two stations on both sides of a strait through which the Kuroshio always flows. The sea level variations are due to the variations both of the barotropic transport and the baroclinic transport. The total volume transport of the Kuroshio is composed of transports through the Osumi and Tokara Straits (Kawabe, 1995).

Figure 25 looks at the time variations of the depth averaged transport derived from the monthly averaged sea level, the Sverdrup transport and the $PC_1^{\psi} + \overline{X}$ Sverdrup transport. Sea level data from the Joint Archive for Sea Level (JASL) at the University of Hawaii was obtained for two stations on opposite sides of the Tokara Strait. Monthly mean values from 1964 thru 1968 were used for Naze, Japan (28°22.7'N, 129°29.9'E) and Nishinoomote, Japan (30°43.9'N, 130°59.7'E). A mean *f* between the two stations was used to calculate the transport at a depth of 1000 meters. The Sverdrup transport and the $PC_1^{\psi} + \overline{X}$ Sverdrup transport is the transport between the two grid points nearest the tide stations, 27.5°N, 130°E and 30°N, 130°E. The Sverdrup transport is derived from NCEP wind observations (1948-1999) as described above

There is some discrepancy between the barotropic and baroclinic annual cycle which may be due to unmeasured barotropic changes as was suggested by Hautala et al. (1994) for the difference between the annual mean Sverdrup and Kuroshio transport in

the western Pacific. The Sverdrup relation, however, accounts for a good portion of the seasonal variance of the Kuroshio transport, giving credibility to the results shown here.

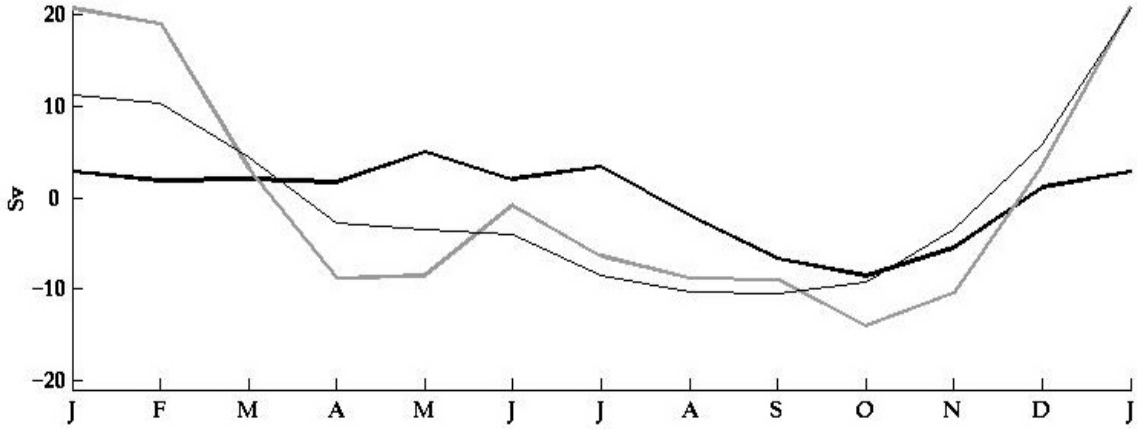


Figure 25. Comparison of Depth Averaged Transport in the Tokara Strait and Sverdrup Transport in the Region. Seasonal Variability of Depth Averaged Transport (Thick Black Line). The Sverdrup Transport (Thick Grey Line) and the $PC_1^{\psi} + \overline{X}$ Sverdrup Transport (Thin Grey Line) is the Transport between the Two Grid Points Nearest the Tide Stations, 27.5°N,130°E And 30°N,130°E. The Sverdrup Transport is Derived from NCEP Wind Observations (1948-1999) as Described Above

## D. INTERANNUAL VARIABILITY

This thesis has characterized the annual variability of the wind stress, Ekman pumping and Sverdrup transport in the North Pacific. The EOF analysis may characterize interannual variability of these circulation fields as well. The PCs were compared with an atmospheric climate index and the first modes, although strongly correlated with each other, were poorly correlated with the climate index. For illustration, Figure 26 shows smoothed time series of $PC_2^{\tau}$, $PC_3^{w}$ and $PC_2^{\psi}$. Down and up arrows indicate the time of the strong historic El Niño and La Niña events, respectively (Wolter and Timlin, 1998).

The PCs are well correlated to each other on the interannual time scale; $r^2_{(PC_2^{\tau},PC_3^{w})} = 0.76$, $r^2_{(PC_2^{\tau},PC_3^{\psi})} = 0.88$, $r^2_{(PC_3^{w},PC_2^{\psi})} = 0.82$. Strong El Niño (La Niña) events are consistently characterized by increases (decreases) in the smoothed time series of all three PCs shown in Figure 26. The implication of this is that El Niño events result in a stronger cyclonic wind stress around the Aleutian Low (Figure 11a), and a weaker North

Pacific Current (Figure 11c). The associated Ekman pumping will be greater in the coastal Gulf of Alaska and south of 45°N, and weaker in the California Current and Bering Sea (Figure 13b). The encouraging correlation of these PCs with the El Niño-Southern Oscillation (ENSO) signals suggests EOF analysis of seasonal values of these fields will yield an improved understanding of the response of the North Pacific Ocean to ENSO forcing.

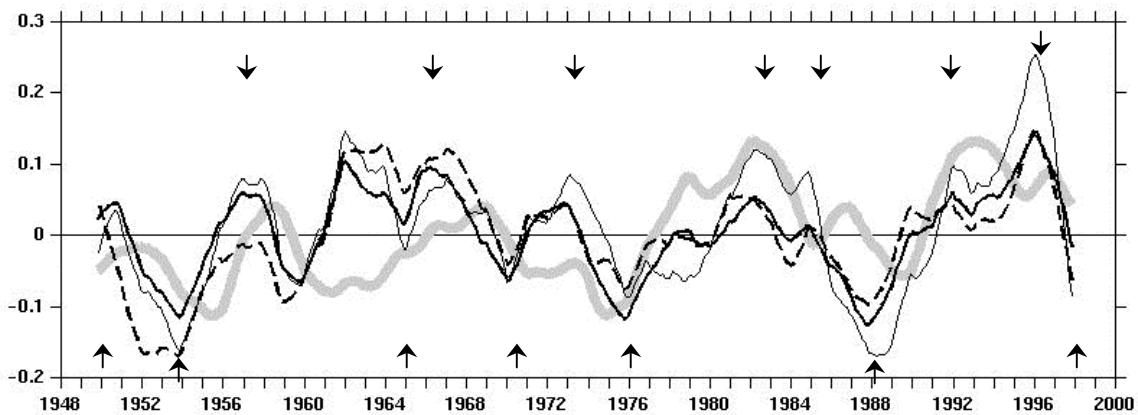


Figure 26. Smoothed Time Series (36 point) of $PC_{km}^{X}$ as Indicated Versus Smoothed Time Series (36 point) Monthly NOI(/-15) Values (Schwing *et al*., 2001) (heavy gray line). NOI is an Index of North Pacific Climate Variability.

There is also some evidence of coherent longer-term variability in these results. The three PCs are plotted against monthly Northern Oscillation Index (NOI) values, an environmental index of interannual to decadal climate variability in the North Pacific (Schwing et al., 2001). The PCs follow the general trend of the NOI and explain about one quarter to one third of the interannual variability of the NOI using this method of EOF analysis; $r^2_{(PC_2^{\tau},NOI)} = 0.38$, $r^2_{(PC_3^{w},NOI)} = 0.25$, $r^2_{(PC_2^{w},NOI)} = 0.36$. There appears to be some coincidence between the PCs and the NOI on decadal scales. For example, all series increase at about the time of a reported regime shift in 1976 (Trenberth, and Hurrell, 1994). Future work is planned using a similar EOF methodology to explore interannual variability by season.

# APPENDIX A. VARIANCE

Percentage of total variance and cumulative variance explained by the first 10 EOF modes for wind stress ($\tau$ = Pa$^2$), Ekman pumping ($w$=cm$^2$ day$^{-2}$) and Sverdrup transport ($\psi$ = Sv$^2$).

| Mode | $\tau$ | | $w$ | | $\psi$ | |
|---|---|---|---|---|---|---|
| | Variance | | Variance | | Variance | |
| | Percent | Cumulative | Percent | Cumulative | Percent | Cumulative |
| 1 | 34.5 | 34.5 | 23.5 | 23.5 | 45.6 | 45.6 |
| 2 | 14.9 | 49.4 | 9.9 | 33.4 | 19.7 | 65.3 |
| 3 | 8.5 | 57.9 | 5.1 | 38.5 | 9.3 | 74.6 |
| 4 | 5.9 | 63.8 | 4.0 | 42.5 | 5.6 | 80.2 |
| 5 | 5.1 | 68.9 | 2.9 | 45.4 | 3.2 | 83.4 |
| 6 | 3.4 | 72.3 | 2.5 | 47.9 | 2.9 | 86.3 |
| 7 | 2.4 | 74.7 | 2.2 | 50.1 | 1.7 | 88.0 |
| 8 | 1.9 | 76.6 | 1.8 | 51.9 | 1.7 | 89.7 |
| 9 | 1.3 | 77.9 | 1.8 | 53.7 | 1.4 | 91.1 |
| 10 | 1.2 | 79.1 | 1.4 | 55.1 | 1.2 | 92.3 |

THIS PAGE INTENTIONALLY LEFT BLANK

# APPENDIX B. LONG-TERM MONTHLY MEAN PRINCIPAL COMPONENTS

Long-term (1948-1999) monthly mean ($\overline{m}$) principal components ($PC_{k\overline{m}}^{X}$) for wind stress ($X = \tau$), Ekman pumping ($X = w$) and Sverdrup Transport ($X = \psi$) for the first ($PC_1^X$), second ($PC_2^X$) and third ($PC_3^X$) principal components.

| Month | $PC_1^X$ | | | $PC_2^X$ | | | $PC_3^X$ | | |
|---|---|---|---|---|---|---|---|---|---|
| | $\tau$ | $w$ | $\psi$ | $\tau$ | $w$ | $\psi$ | $\tau$ | $w$ | $\psi$ |
| J | 1.375 | 0.059 | 0.52 | 0.576 | 0.012 | 0.17 | 0.324 | 0.037 | 0.25 |
| F | 1.178 | 0.048 | 0.48 | 0.459 | 0.025 | 0.09 | 0.172 | 0.018 | 0.25 |
| M | 0.508 | 0.026 | 0.25 | -0.017 | 0.029 | -0.13 | 0.148 | -0.021 | 0.05 |
| A | -0.256 | -0.001 | -0.04 | -0.306 | 0.023 | -0.17 | -0.038 | -0.035 | -0.06 |
| M | -0.542 | -0.018 | -0.07 | 0.052 | 0.031 | 0.01 | -0.241 | -0.024 | -0.20 |
| J | -0.811 | -0.033 | -0.09 | 0.477 | 0.042 | 0.22 | -0.281 | -0.002 | -0.30 |
| J | -1.135 | -0.047 | -0.27 | 0.343 | 0.020 | 0.22 | -0.118 | 0.006 | -0.38 |
| A | -1.111 | -0.051 | -0.35 | 0.279 | -0.000 | 0.26 | -0.113 | 0.013 | -0.13 |
| S | -0.682 | -0.042 | -0.35 | 0.071 | -0.028 | 0.15 | -0.291 | 0.019 | -0.04 |
| O | -0.140 | -0.014 | -0.30 | -0.618 | -0.064 | -0.19 | -0.142 | 0.004 | 0.14 |
| N | 0.484 | 0.021 | -0.07 | -0.998 | -0.066 | -0.41 | 0.262 | -0.017 | 0.22 |
| D | 1.130 | 0.051 | 0.30 | -0.318 | -0.026 | -0.22 | 0.317 | 0.002 | 0.21 |

THIS PAGE INTENTIONALLY LEFT BLANK

# APPENDIX C. MAGNITUDE AND ROTATION ANGLE

Long-term (1948-1999) monthly mean *magnitude* $\left(PC_{\overline{km}}^{\tau}\right)$ (Amplitude) and *rotation angle* $\left(PC_{\overline{km}}^{\tau}\right)$ (Rotation) for the first ($PC_1^{\tau}$), second ($PC_2^{\tau}$) and third ($PC_3^{\tau}$) principal components of wind stress.

| Month | $PC_1^{\tau}$ | | $PC_2^{\tau}$ | | $PC_3^{\tau}$ | |
|---|---|---|---|---|---|---|
| | Amplitude | Rotation | Amplitude | Rotation | Amplitude | Rotation |
| J | 1.6537 | 33.7229 | 0.5815 | 7.6212 | 0.3344 | 14.6895 |
| F | 1.3977 | 32.5308 | 0.4671 | 10.9634 | 0.1725 | 355.6761 |
| M | 0.5946 | 31.4013 | 0.0302 | 123.5166 | 0.1684 | 331.6285 |
| A | 0.3191 | 216.6722 | 0.3145 | 193.6069 | 0.0402 | 160.4186 |
| M | 0.6227 | 209.5626 | 0.0581 | 333.0765 | 0.2830 | 211.7337 |
| J | 0.9158 | 207.6332 | 0.4842 | 10.0637 | 0.3475 | 216.0875 |
| J | 1.2784 | 207.4295 | 0.3443 | 4.8415 | 0.2019 | 234.2814 |
| A | 1.2632 | 208.4240 | 0.2800 | 4.4830 | 0.1639 | 226.6040 |
| S | 0.8140 | 213.1499 | 0.0923 | 40.1402 | 0.2972 | 191.4542 |
| O | 0.2795 | 239.9615 | 0.6182 | 182.1053 | 0.2839 | 119.8881 |
| N | 0.5008 | 14.7813 | 1.0138 | 190.0247 | 0.3804 | 46.5604 |
| D | 1.3257 | 31.4950 | 0.3294 | 195.2547 | 0.3590 | 27.8798 |

THIS PAGE INTENTIONALLY LEFT BLANK

# APPENDIX D. $M_{4-10}^{\tau,w,\psi}$

Seasonal time series of the $PC_{4-10\overline{m}}^{\tau,w,\psi}$, $E_{4-10\overline{m}}^{\tau,w,\psi}$ pairings, referred to as modes and designated $M_{4-10}^{\tau,w,\psi}$. The principal components (PC) for a particular mode (M) and the corresponding eigenvectors (E) are each on separate pages. Captions at the bottom of each page reference the mode.

There are four principal component plots per mode: (a) *rotation angle*$\left(PC_{k\overline{m}}^{\tau}\right)$ is the solid line and *magnitude*$\left(PC_{k\overline{m}}^{\tau}\right)$ is the broken line (b) $\mathrm{Re}\left(PC_{k\overline{m}}^{\tau}\right)$ is the solid line and $\mathrm{Im}\left(PC_{k\overline{m}}^{\tau}\right)$ is the broken line. (c) $PC_{k\overline{m}}^{w}$ (d) $PC_{k\overline{m}}^{\psi}$. Shaded region is $\pm 1\sigma$.

There are three eigenvector plots per mode: (a) $E_k^{\tau}$. Scaling vector is 0.25 Pa. (b) $E_k^{w}$. Contour interval is 100 cm day$^{-1}$. (c) $E_k^{\psi}$. Solid lines indicate negative values. Arrowheads indicate direction of transport.

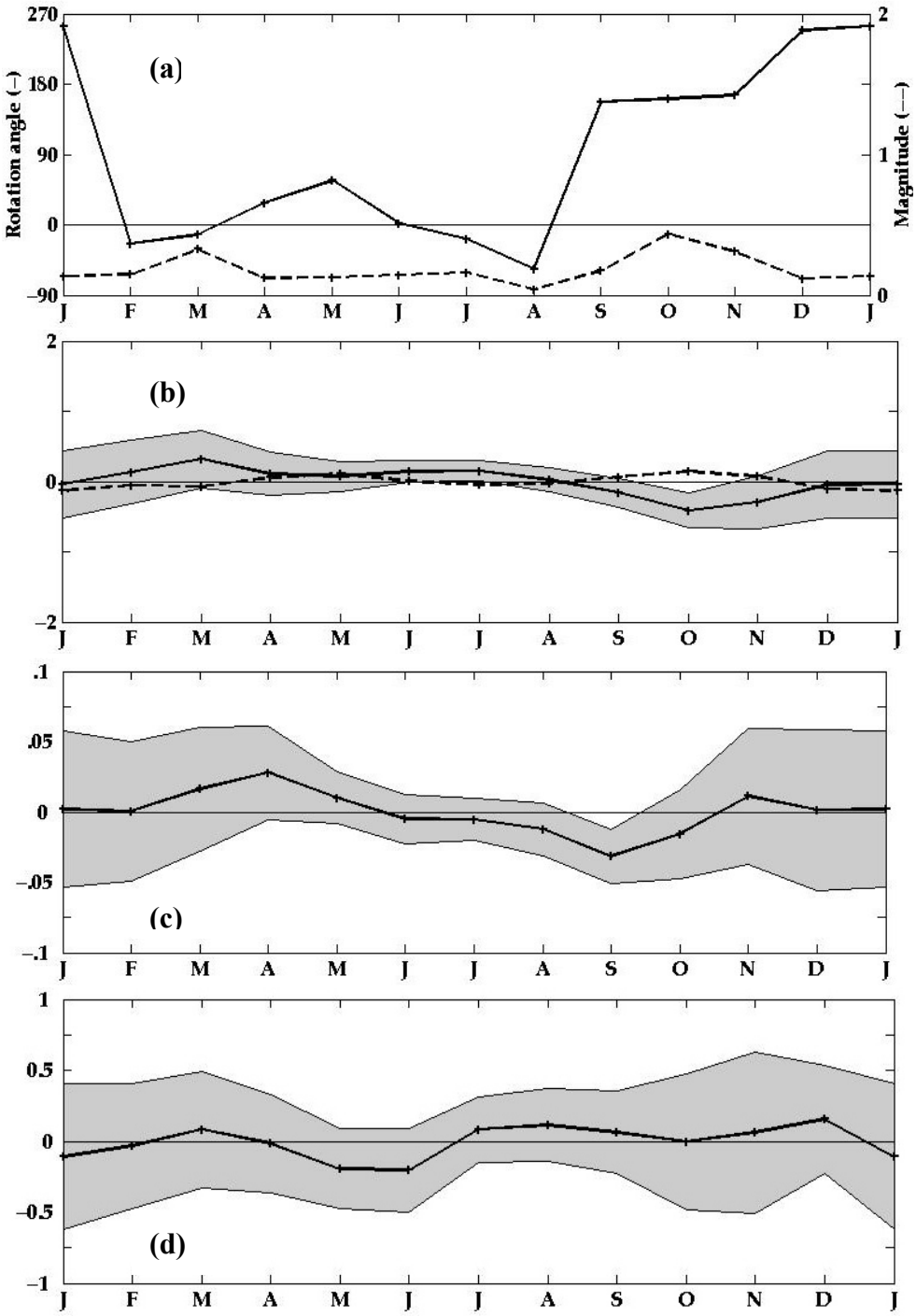


Seasonal Time Series of $PC_{4\overline{m}}^{X}$. (a) *rotation angle*$\left(PC_{4\overline{m}}^{\tau}\right)$ is the Solid Line and *magnitude*$\left(PC_{4\overline{m}}^{\tau}\right)$ is the Broken Line (b) $\mathrm{Re}\left(PC_{4\overline{m}}^{\tau}\right)$ is the Solid Line and $\mathrm{Im}\left(PC_{4\overline{m}}^{\tau}\right)$ is the Broken Line. (c) $PC_{4\overline{m}}^{w}$ (d) $PC_{4\overline{m}}^{\psi}$. Shaded Region is $\pm 1\sigma$.

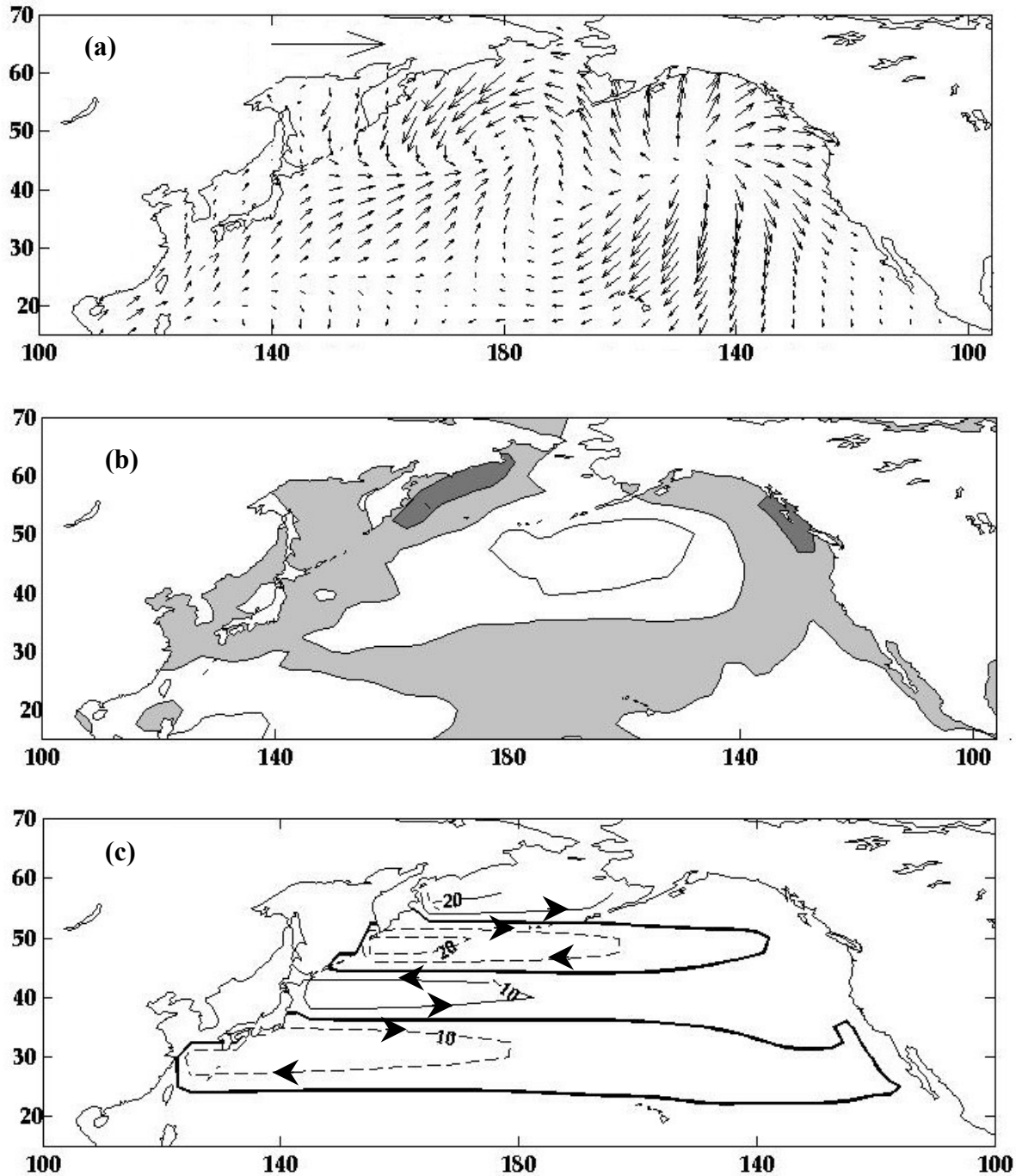


Eigenvector ( $E_4^X$ ) Plots. (a) $E_4^\tau$. Scaling Vector is 0.25 Pa. (b) $E_4^w$. Contour Interval is 100 cm Day$^{-1}$. (c) $E_4^\psi$. Solid Lines Indicate Negative Values. Arrowheads Indicate Direction of Transport. Zero is Bold.

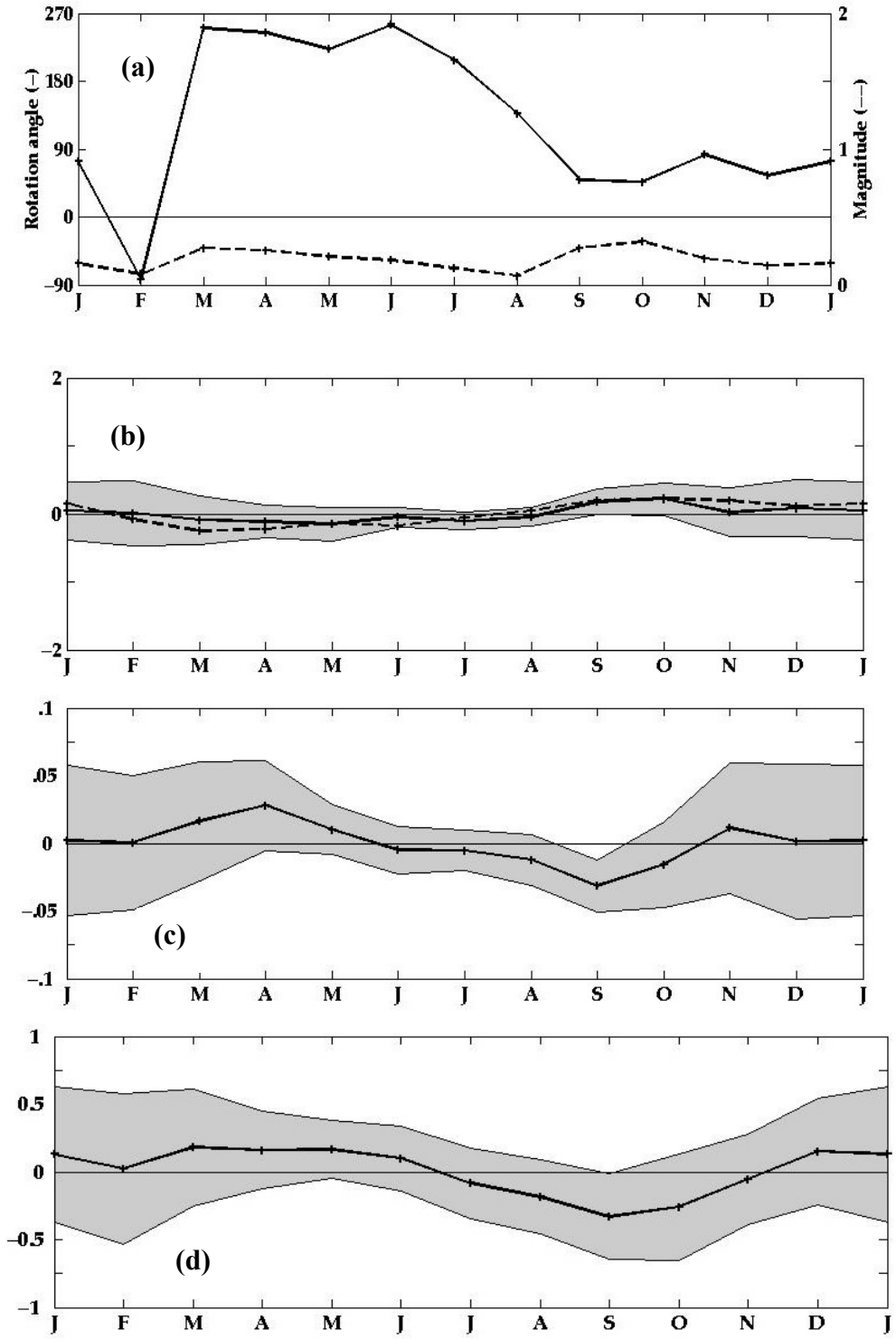


Seasonal Time Series of $PC_{5\overline{m}}^{X}$. (a) *rotation angle* $\left(PC_{5\overline{m}}^{\tau}\right)$ is the Solid Line and *magnitude* $\left(PC_{5\overline{m}}^{\tau}\right)$ is the Broken Line (b) $\mathrm{Re}\left(PC_{5\overline{m}}^{\tau}\right)$ is the Solid Line and $\mathrm{Im}\left(PC_{5\overline{m}}^{\tau}\right)$ is the Broken Line. (c) $PC_{5\overline{m}}^{w}$ (d) $PC_{5\overline{m}}^{\psi}$. Shaded Region is $\pm 1\sigma$.

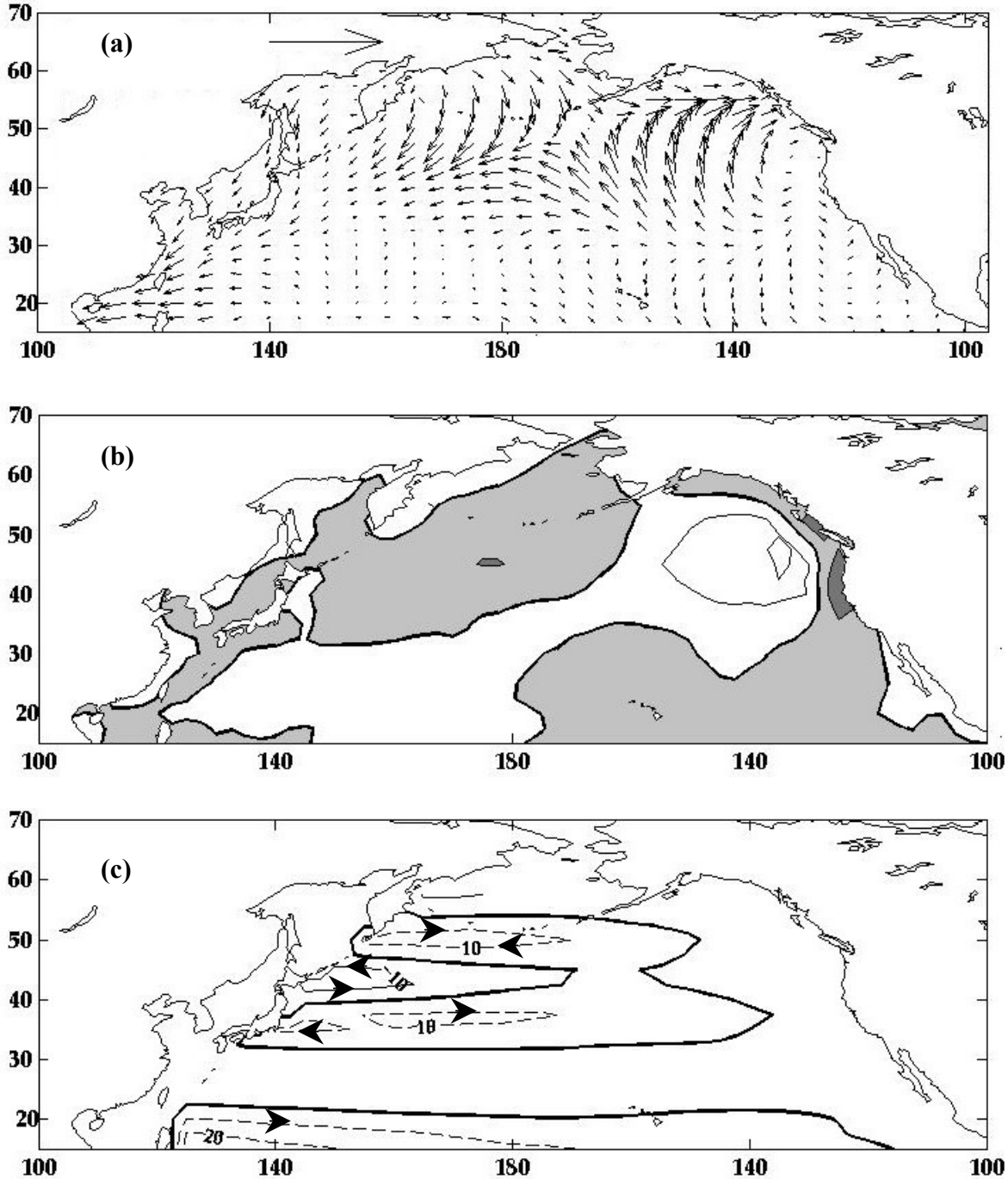


Eigenvector ( $E_5^X$ ) Plots. (a) $E_5^\tau$ . Scaling Vector is 0.25 Pa. (b) $E_5^w$ . Contour Interval is 100 cm Day$^{-1}$. (c) $E_5^\psi$ . Solid Lines Indicate Negative Values. Arrowheads Indicate Direction of Transport. Zero is Bold.

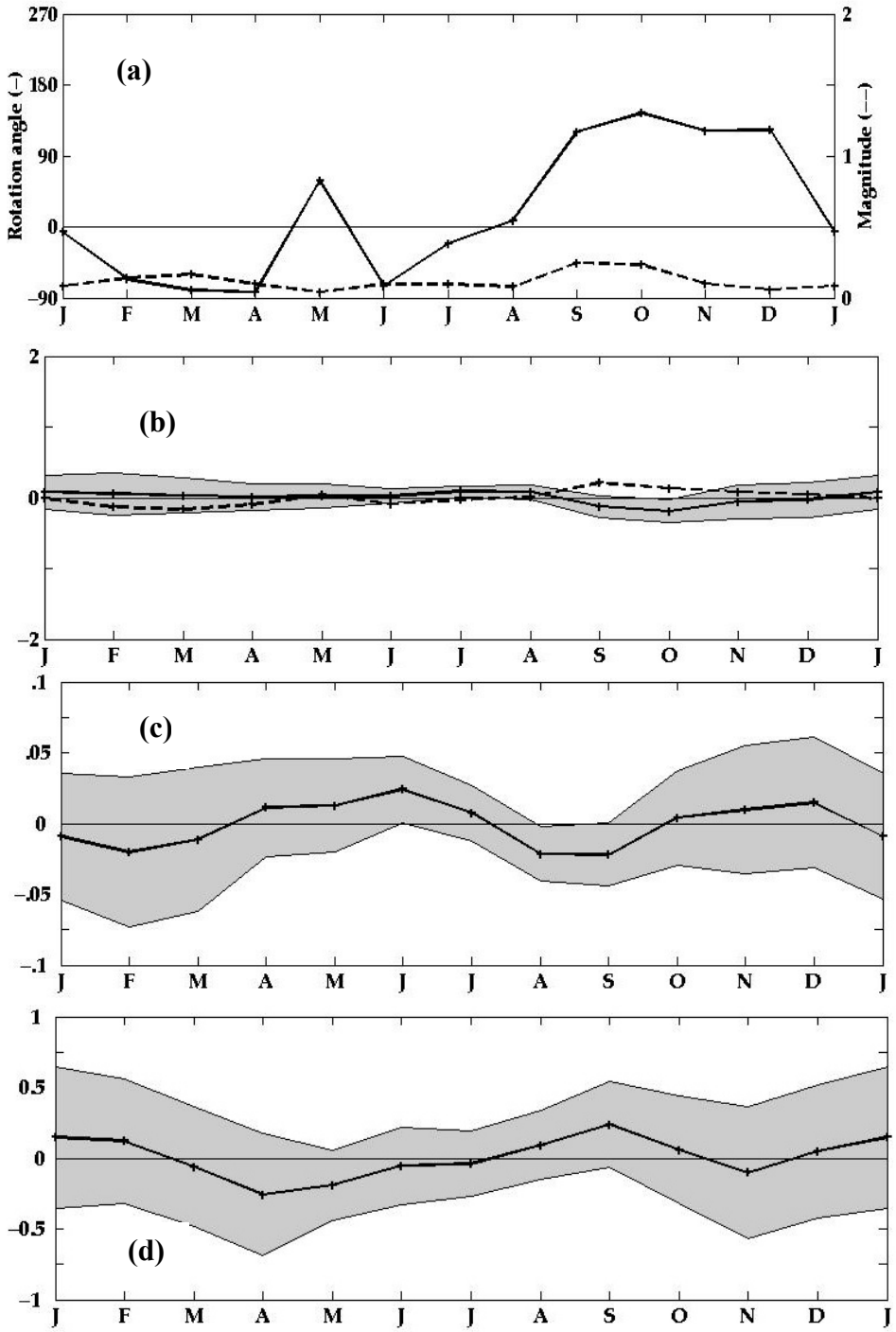


Seasonal Time Series of $PC_{6\overline{m}}^{X}$. (a) *rotation angle*$\left(PC_{6\overline{m}}^{\tau}\right)$ is the Solid Line and *magnitude*$\left(PC_{6\overline{m}}^{\tau}\right)$ is the Broken Line (b) $\mathrm{Re}\left(PC_{6\overline{m}}^{\tau}\right)$ is the Solid Line and $\mathrm{Im}\left(PC_{6\overline{m}}^{\tau}\right)$ is the Broken Line. (c) $PC_{6\overline{m}}^{w}$ (d) $PC_{6\overline{m}}^{\psi}$. Shaded Region is $\pm 1\sigma$.

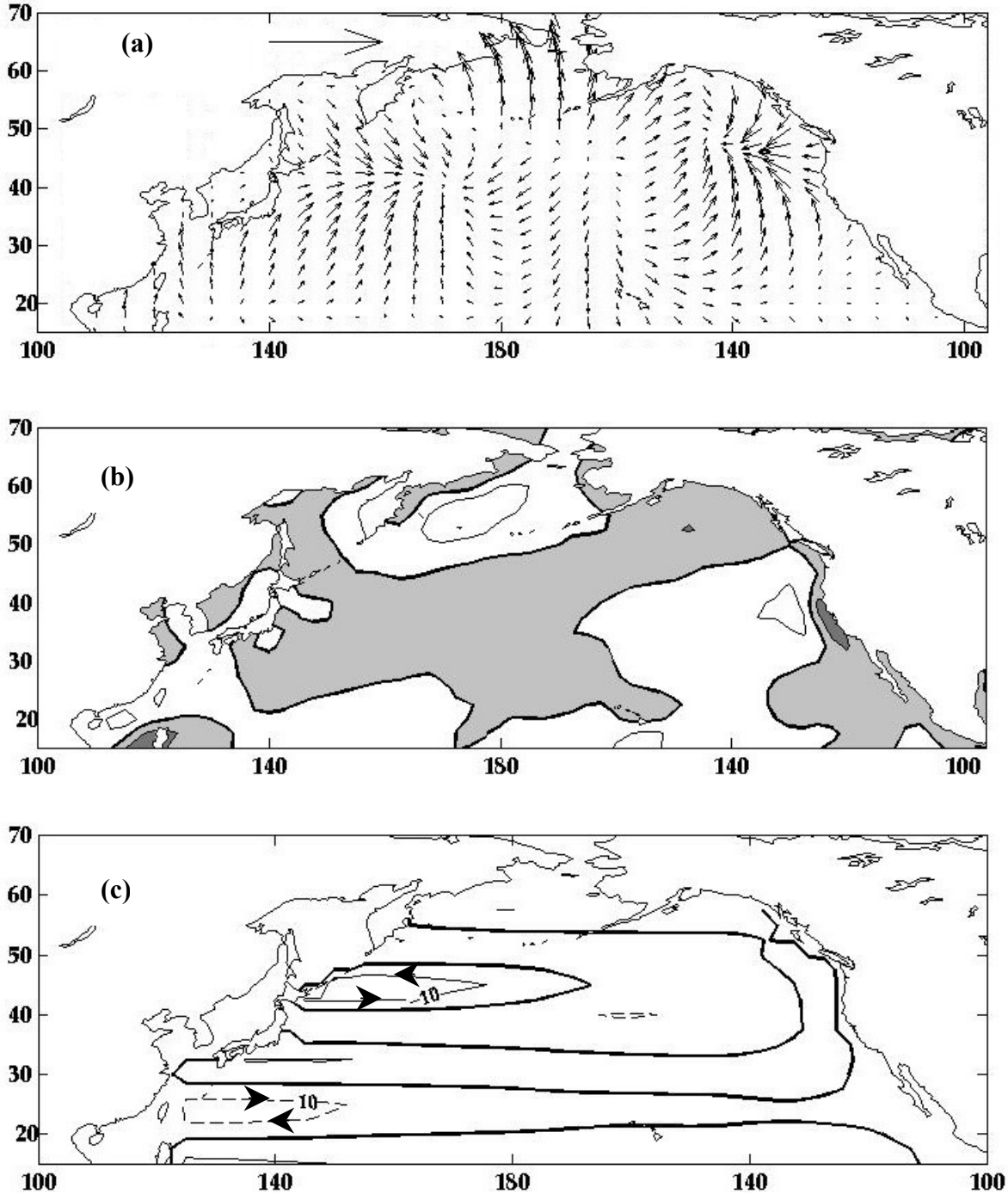


Eigenvector ( $E_6^X$ ) Plots. (a) $E_6^\tau$ . Scaling Vector is 0.25 Pa. (b) $E_6^w$ . Contour Interval is 100 cm Day$^{-1}$. (c) $E_6^\psi$ . Solid Lines Indicate Negative Values. Arrowheads Indicate Direction of Transport. Zero is Bold.

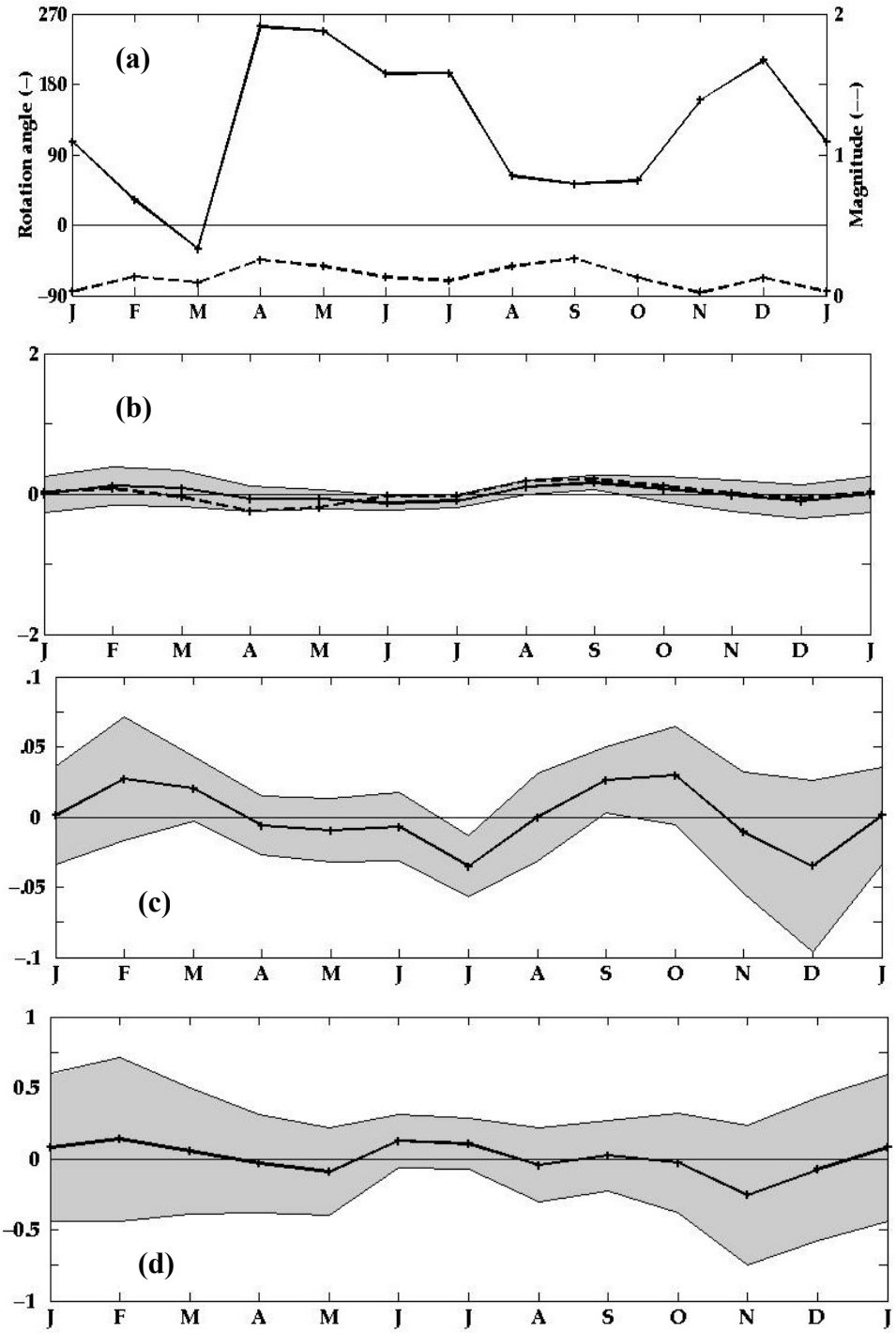


Seasonal Time Series of $PC_{7\overline{m}}^{X}$. (a) *rotation angle*$\left(PC_{7\overline{m}}^{\tau}\right)$is the Solid Line and *magnitude*$\left(PC_{7\overline{m}}^{\tau}\right)$ is the Broken Line (b) $\mathrm{Re}\left(PC_{7\overline{m}}^{\tau}\right)$ is the Solid Line and $\mathrm{Im}\left(PC_{7\overline{m}}^{\tau}\right)$ is the Broken Line. (c) $PC_{7\overline{m}}^{w}$ (d) $PC_{7\overline{m}}^{\psi}$. Shaded Region is $\pm 1\sigma$.

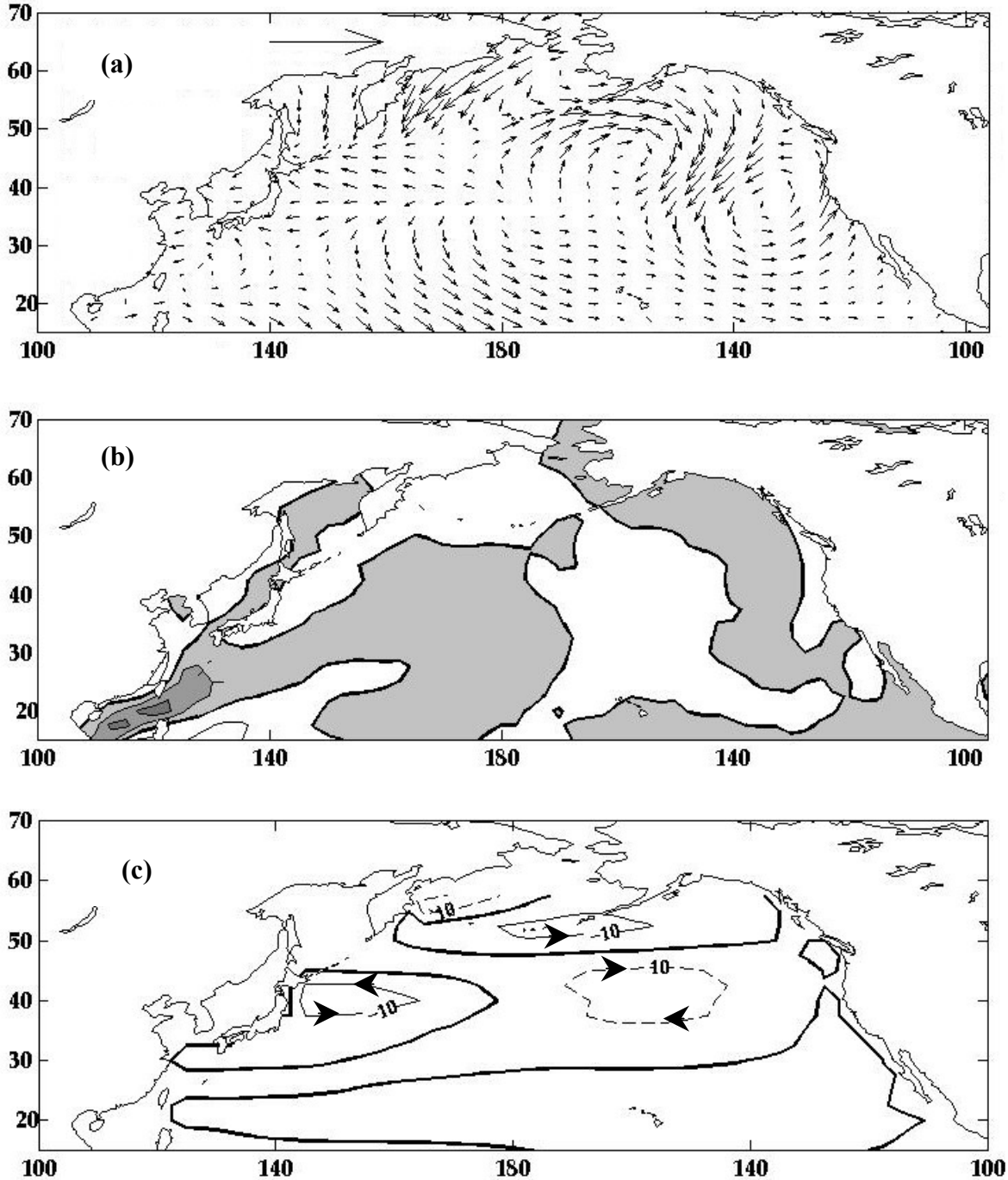


Eigenvector ( $E_7^X$ ) Plots. (a) $E_7^\tau$. Scaling Vector is 0.25 Pa. (b) $E_7^w$. Contour Interval is 100 cm Day$^{-1}$. (c) $E_7^\psi$. Solid Lines Indicate Negative Values. Arrowheads Indicate Direction of Transport. Zero is Bold.

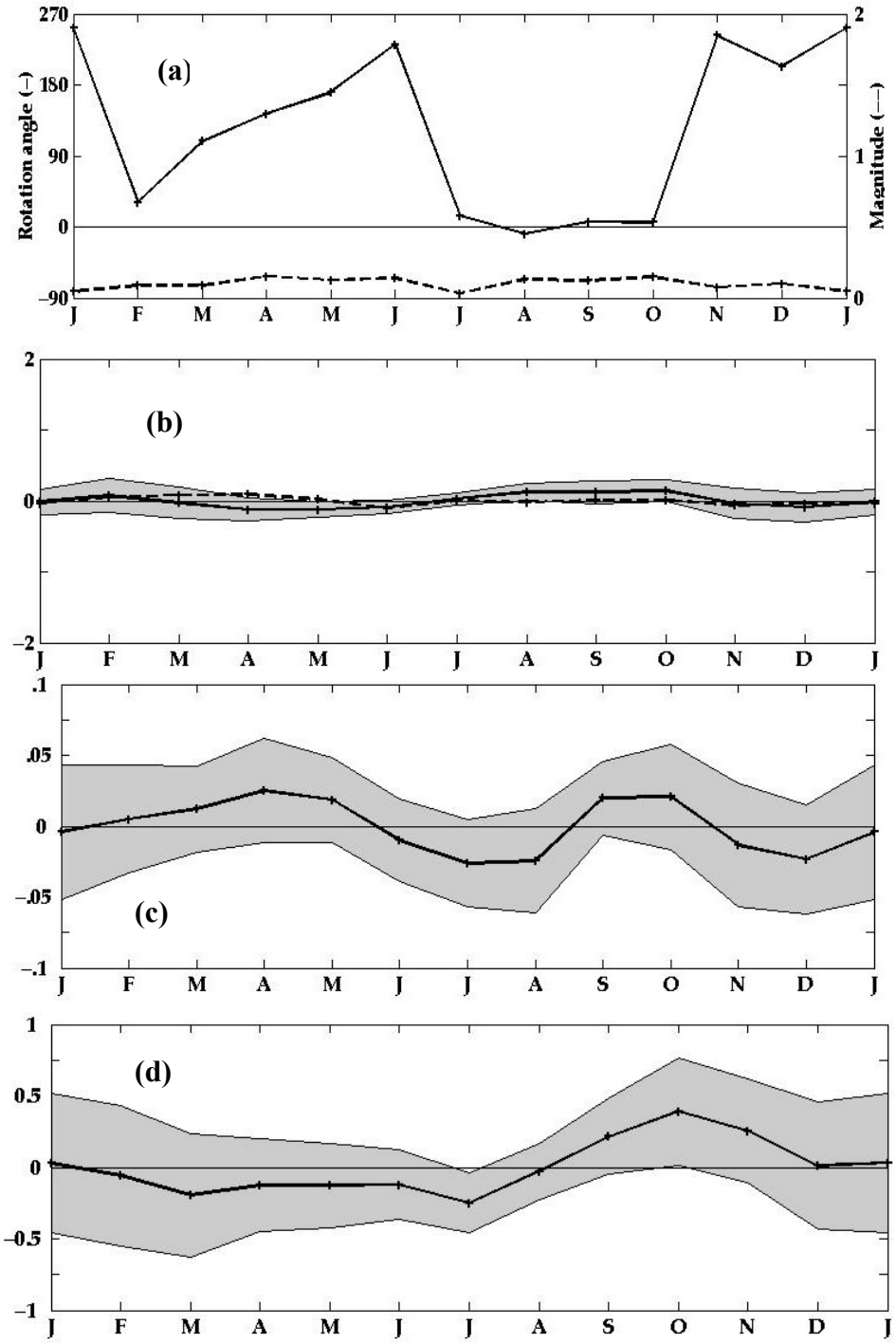


Seasonal Time Series of $PC_{8\overline{m}}^{X}$. (a) *rotation angle* $\left(PC_{8\overline{m}}^{\tau}\right)$ is the Solid Line and *magnitude* $\left(PC_{8\overline{m}}^{\tau}\right)$ is the Broken Line (b) $\mathrm{Re}\left(PC_{8\overline{m}}^{\tau}\right)$ is the Solid Line and $\mathrm{Im}\left(PC_{8\overline{m}}^{\tau}\right)$ is the Broken Line. (c) $PC_{8\overline{m}}^{w}$ (d) $PC_{8\overline{m}}^{\psi}$. Shaded Region is $\pm 1\sigma$.

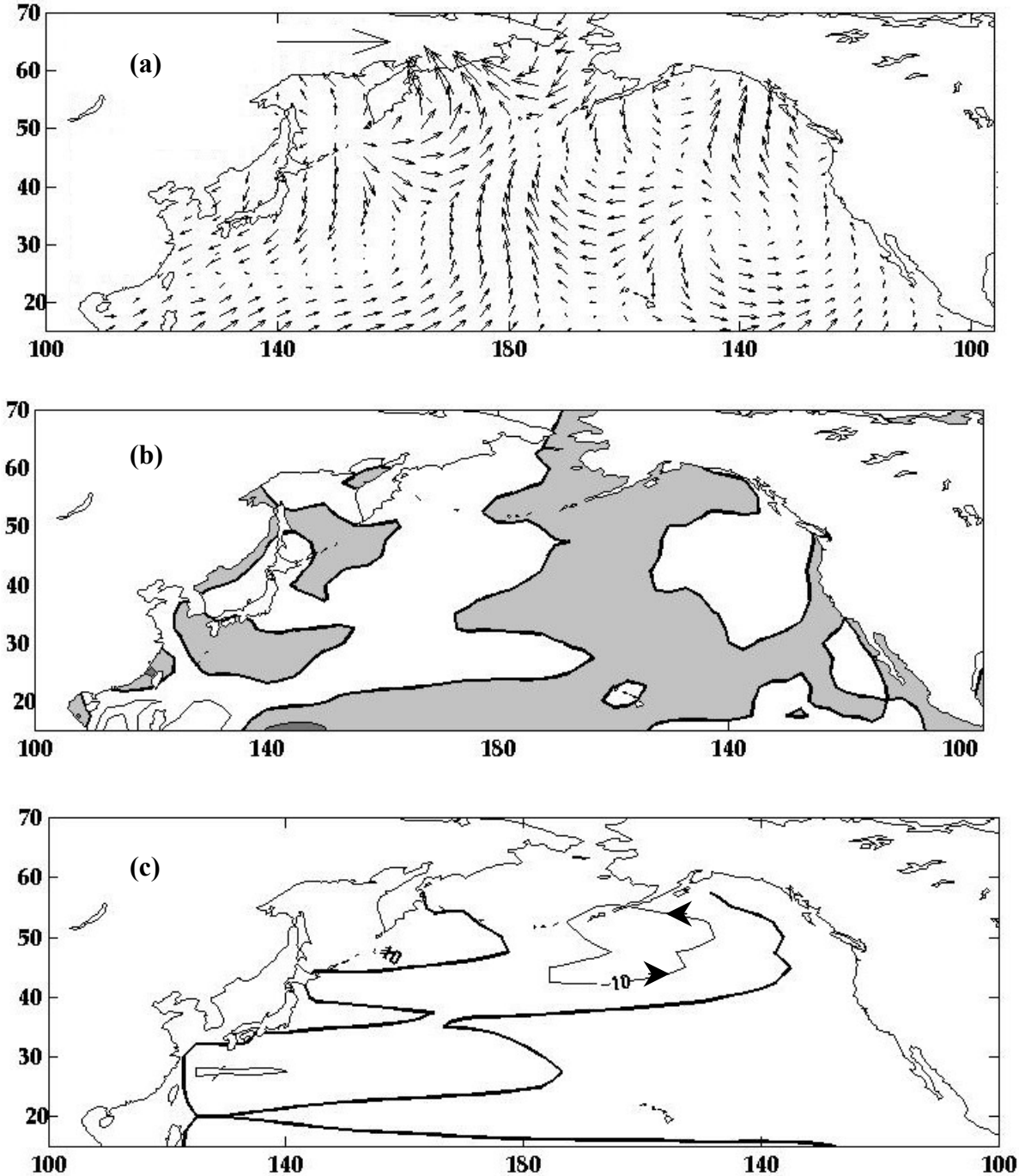


Eigenvector ( $E_8^X$ ) Plots. (a) $E_8^\tau$ . Scaling Vector is 0.25 Pa. (b) $E_8^w$ . Contour Interval is 100 cm Day$^{-1}$. (c) $E_8^\psi$ . Solid Lines Indicate Negative Values. Arrowheads Indicate Direction of Transport. Zero is Bold.

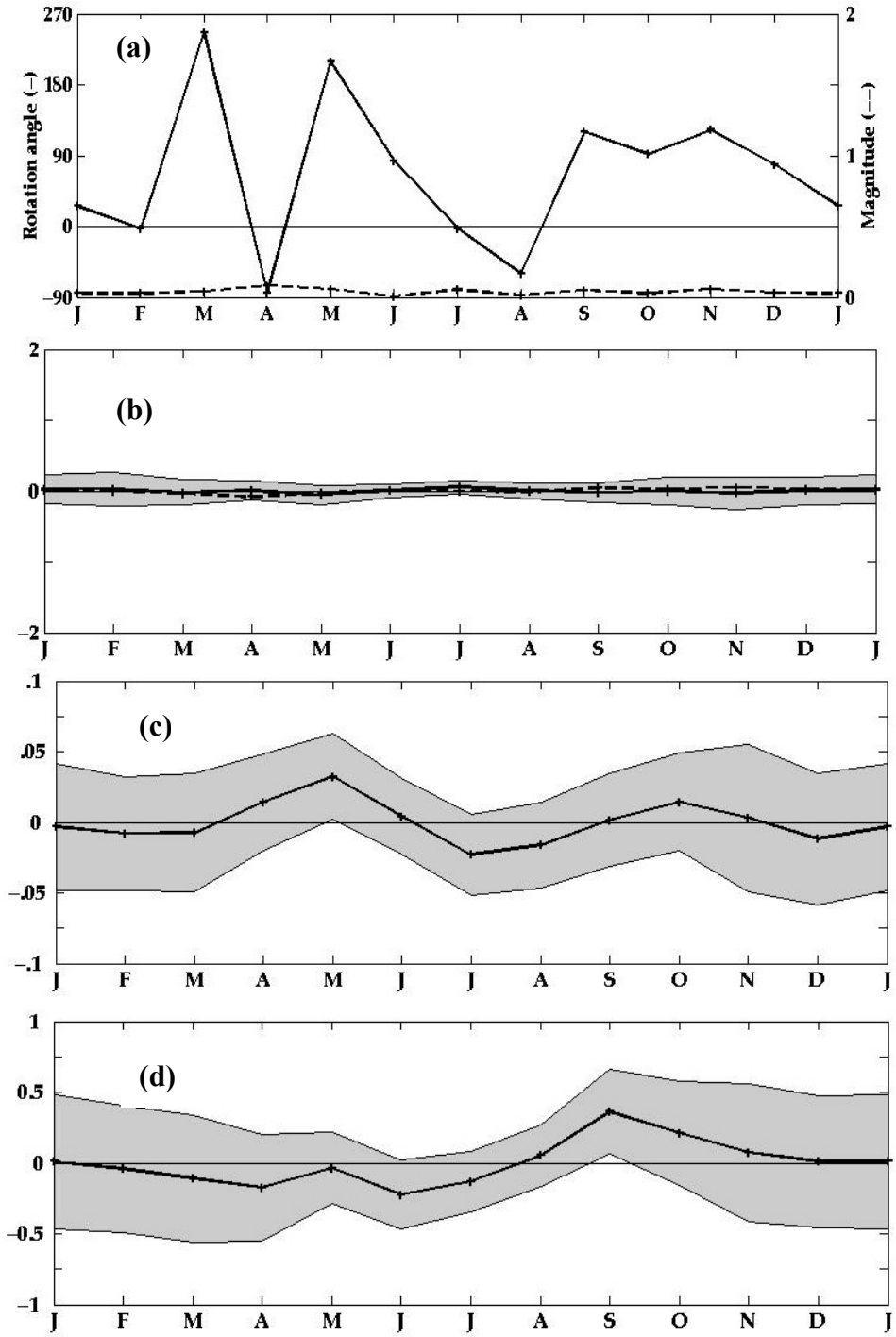


Seasonal Time Series of $PC_{9\overline{m}}^{X}$. (a) *rotation angle*$\left(PC_{9\overline{m}}^{\tau}\right)$ is the Solid Line and *magnitude*$\left(PC_{9\overline{m}}^{\tau}\right)$ is the Broken Line (b) $\mathrm{Re}\left(PC_{9\overline{m}}^{\tau}\right)$ is the Solid Line and $\mathrm{Im}\left(PC_{9\overline{m}}^{\tau}\right)$ is the Broken Line. (c) $PC_{9\overline{m}}^{w}$ (d) $PC_{9\overline{m}}^{\psi}$. Shaded Region is $\pm 1\sigma$.

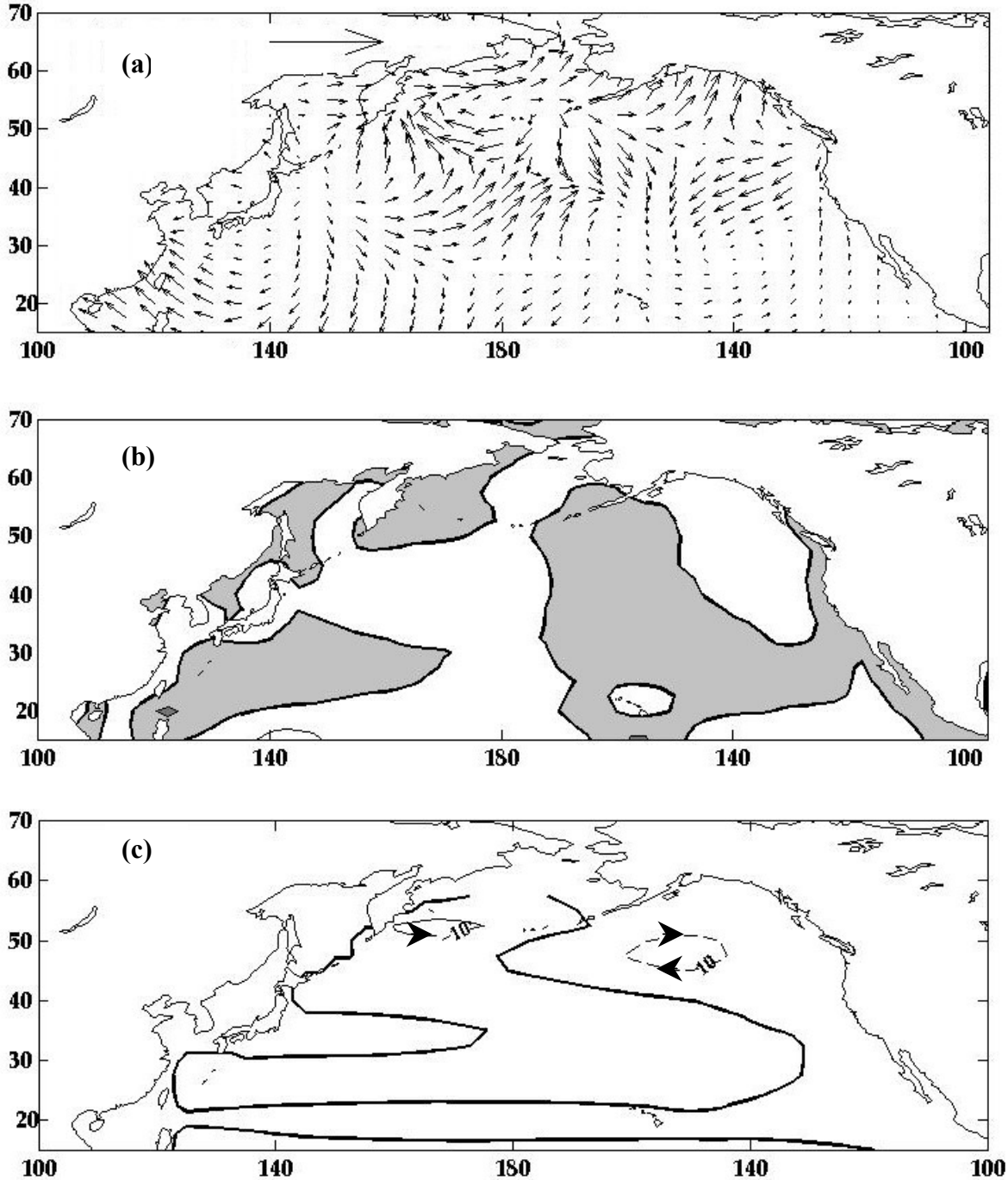


Eigenvector ( $E_9^X$ ) Plots. (a) $E_9^\tau$ . Scaling Vector is 0.25 Pa. (b) $E_9^w$ . Contour Interval is 100 cm Day$^{-1}$. (c) $E_9^\psi$ . Solid Lines Indicate Negative Values. Arrowheads Indicate Direction of Transport. Zero is Bold.

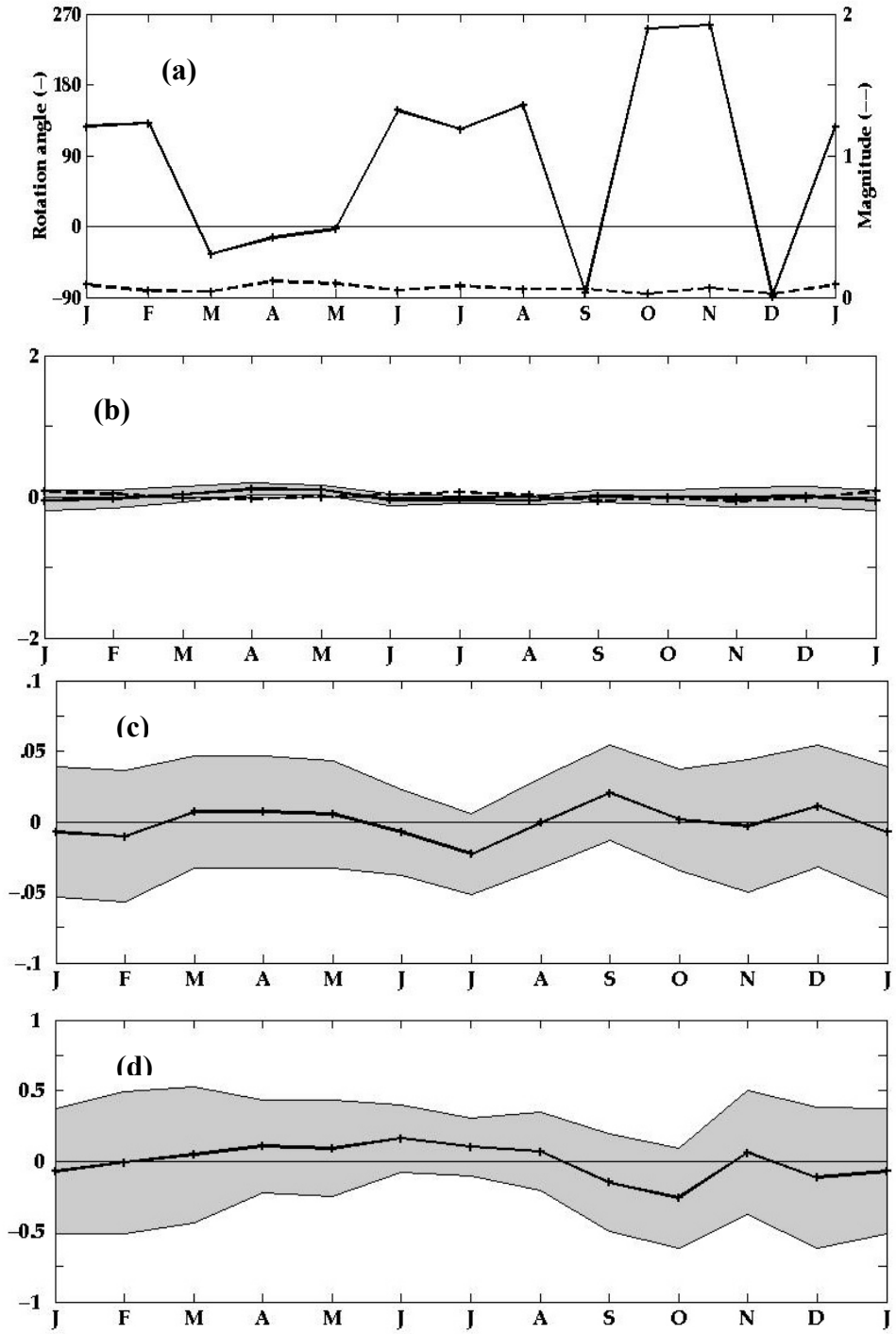


Seasonal Time Series of $PC^{X}_{10\overline{m}}$. (a) *rotation angle* $\left(PC^{\tau}_{10\overline{m}}\right)$ is the Solid Line and *magnitude* $\left(PC^{\tau}_{10\overline{m}}\right)$ is the Broken Line (b) $\mathrm{Re}\left(PC^{\tau}_{10\overline{m}}\right)$ is the Solid Line and $\mathrm{Im}\left(PC^{\tau}_{10\overline{m}}\right)$ is the Broken Line. (c) $PC^{w}_{10\overline{m}}$ (d) $PC^{\psi}_{10\overline{m}}$. Shaded Region is $\pm 1\sigma$.

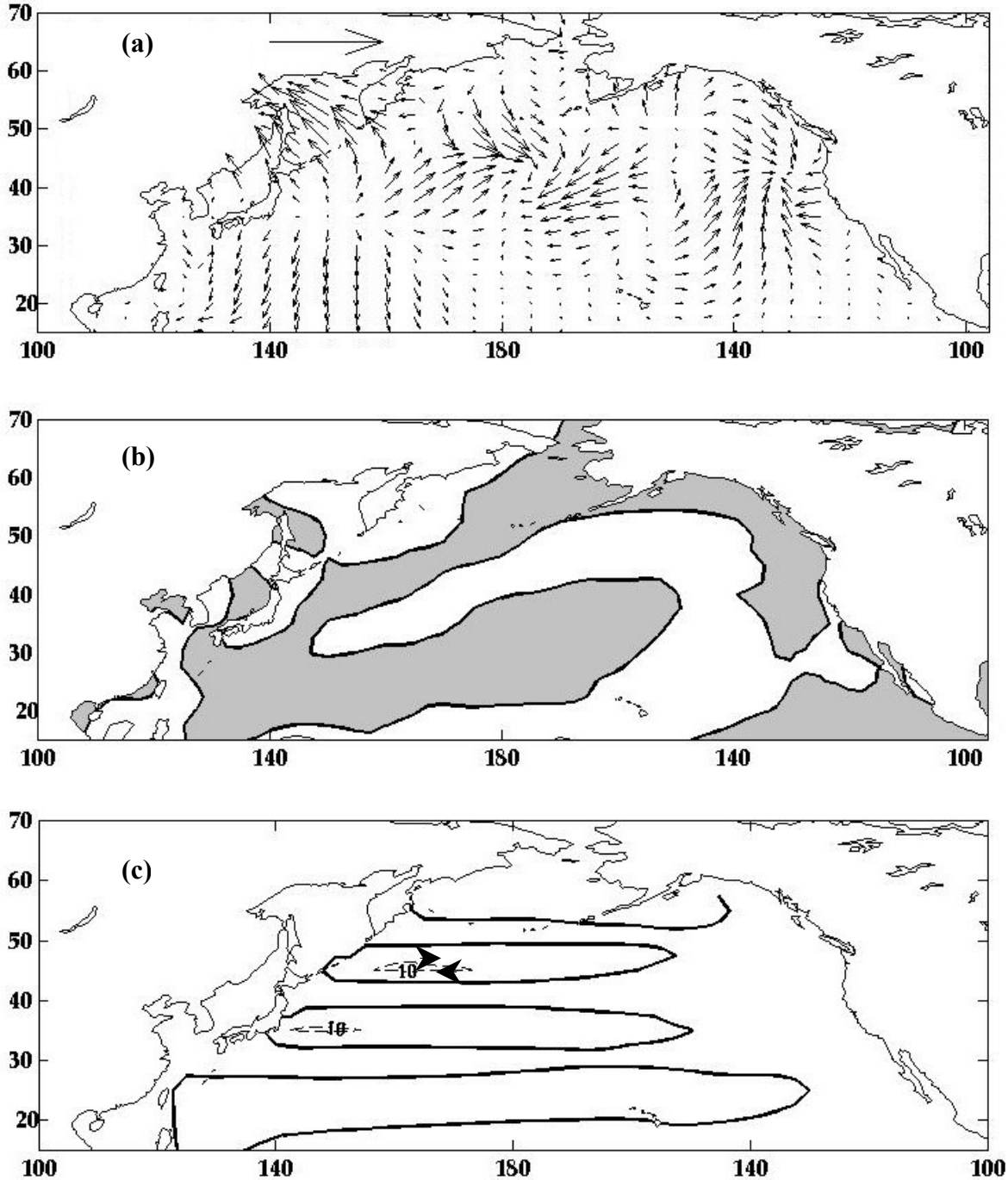


Eigenvector ( $E_{10}^{X}$ ) Plots. (a) $E_{10}^{\tau}$. Scaling Vector is 0.25 Pa. (b) $E_{10}^{w}$. Contour Interval is 100 cm day$^{-1}$. (c) $E_{10}^{\psi}$. Solid Lines Indicate Negative Values. Arrowheads Indicate Direction of Transport. Zero is bold.

THIS PAGE INTENTIONALLY LEFT BLANK

# APPENDIX E. WIND STRESS MONTHLY MEANS

The data shown in this appendix are monthly means of wind stress (Pa = kg $m^{-1}$ $s^{-2}$). The values were derived from NCEP daily averaged surface winds from 1948-1999. Monthly mean fields are computed as the arithmetic mean of each month over the entire time series. Scaling vector is 0.5 Pa.

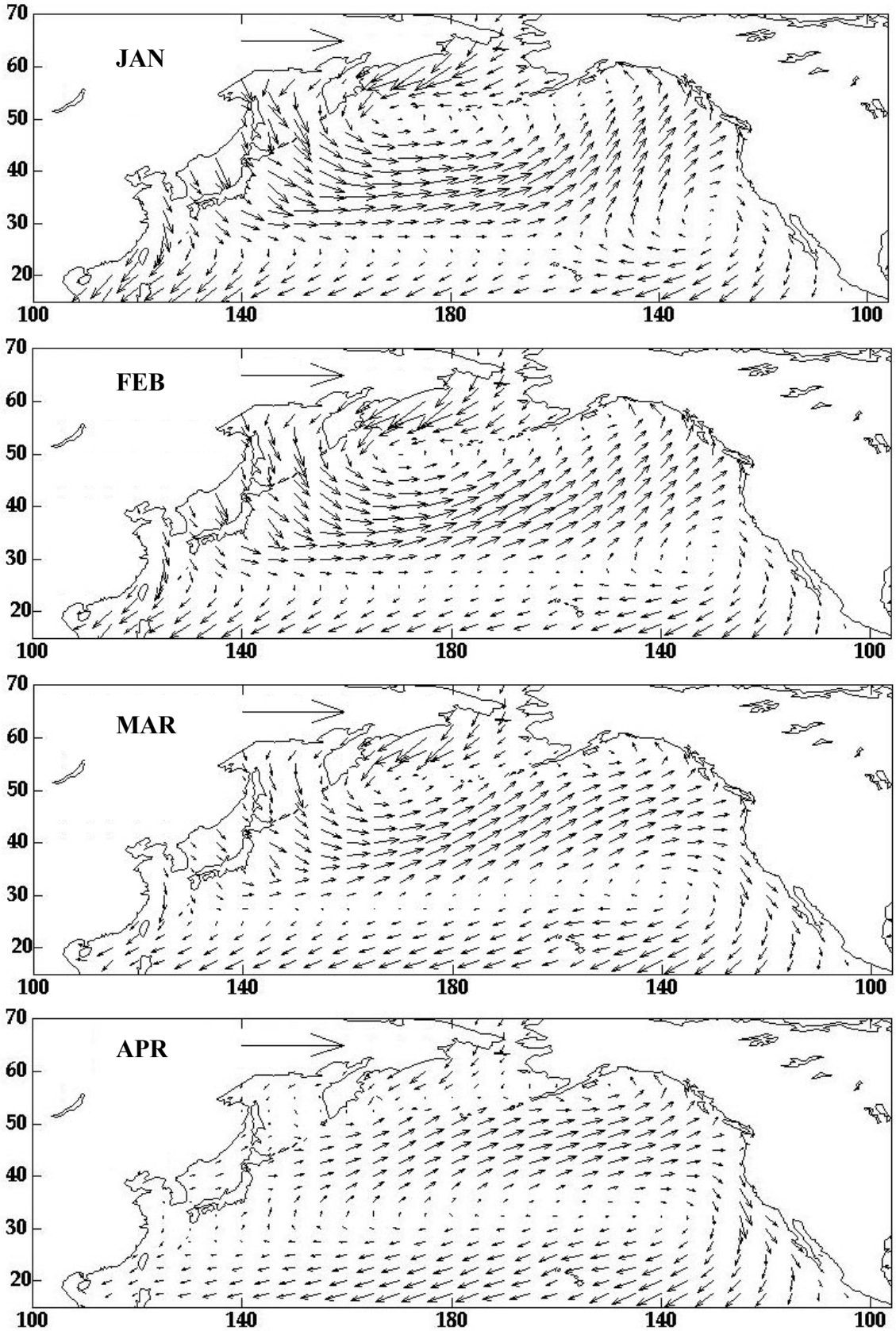
JAN
FEB
MAR
APR
70
60
50
40
30
20
100
140
180
140
100

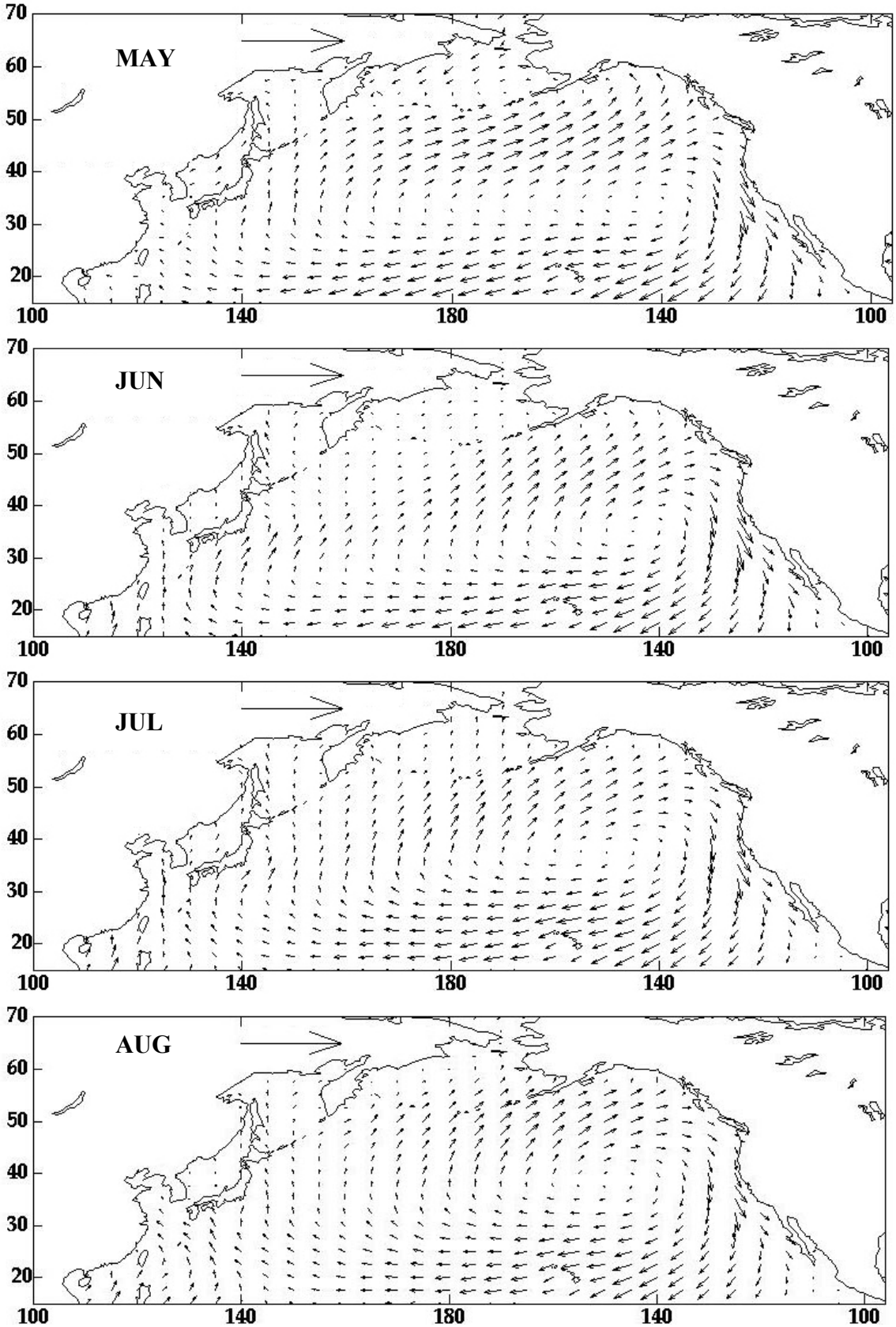
MAY
JUN
JUL
AUG
70
60
50
40
30
20
100
140
180
140
100

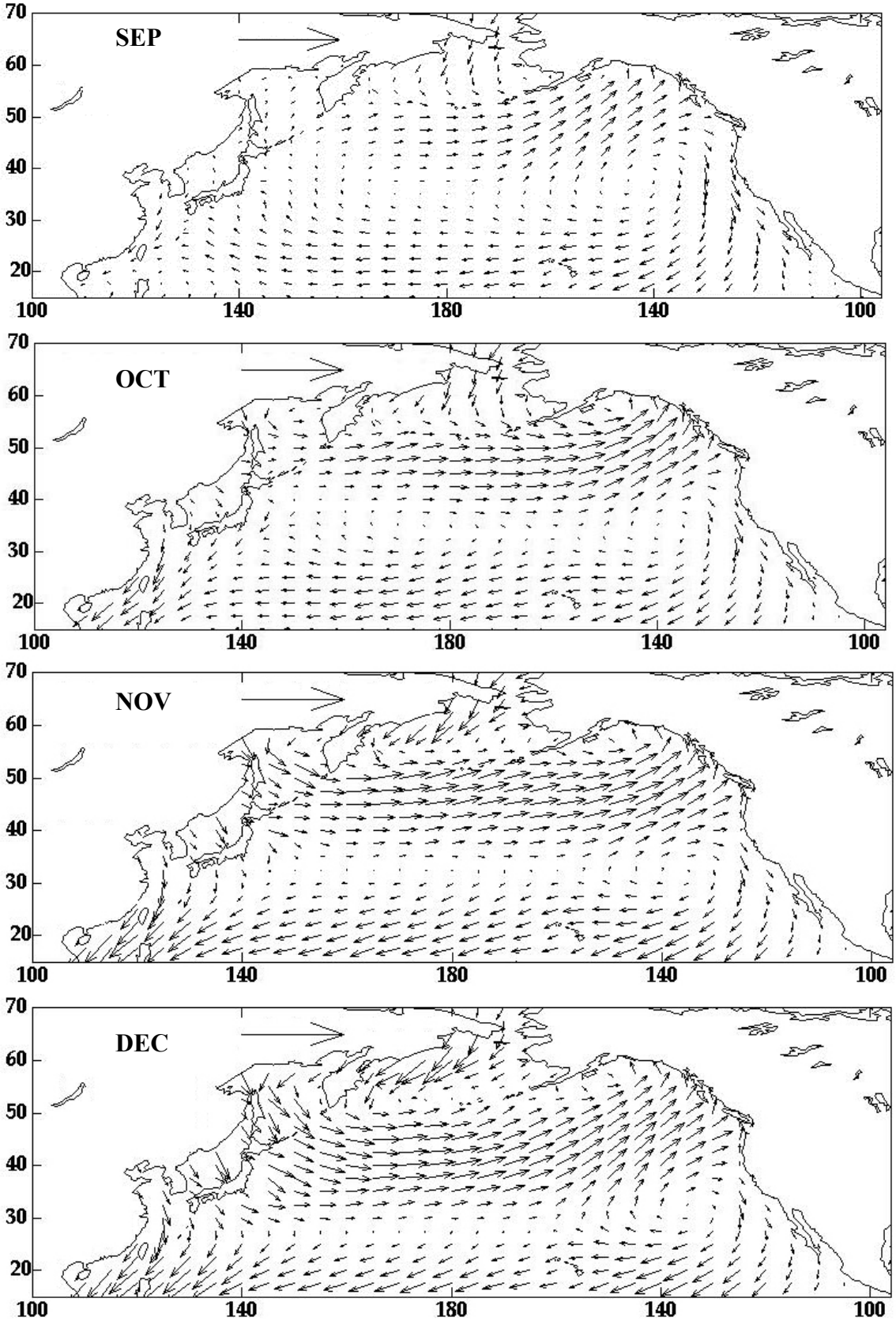
SEP
OCT
NOV
DEC
70
60
50
40
30
20
100
140
180
140
100

# APPENDIX F. EKMAN PUMPING MONTHLY MEAN

The data shown in this appendix are monthly means of Ekman pumping values. The values were derived from monthly averaged wind stress values from the NCEP subset values of daily wind stress. Climatology fields are computed as the arithmetic mean of each month over the entire time series. The zero isotach is bold. The contour interval is 5 $cm^{-1}$ day. Shaded regions indicate positive values (upwelling).

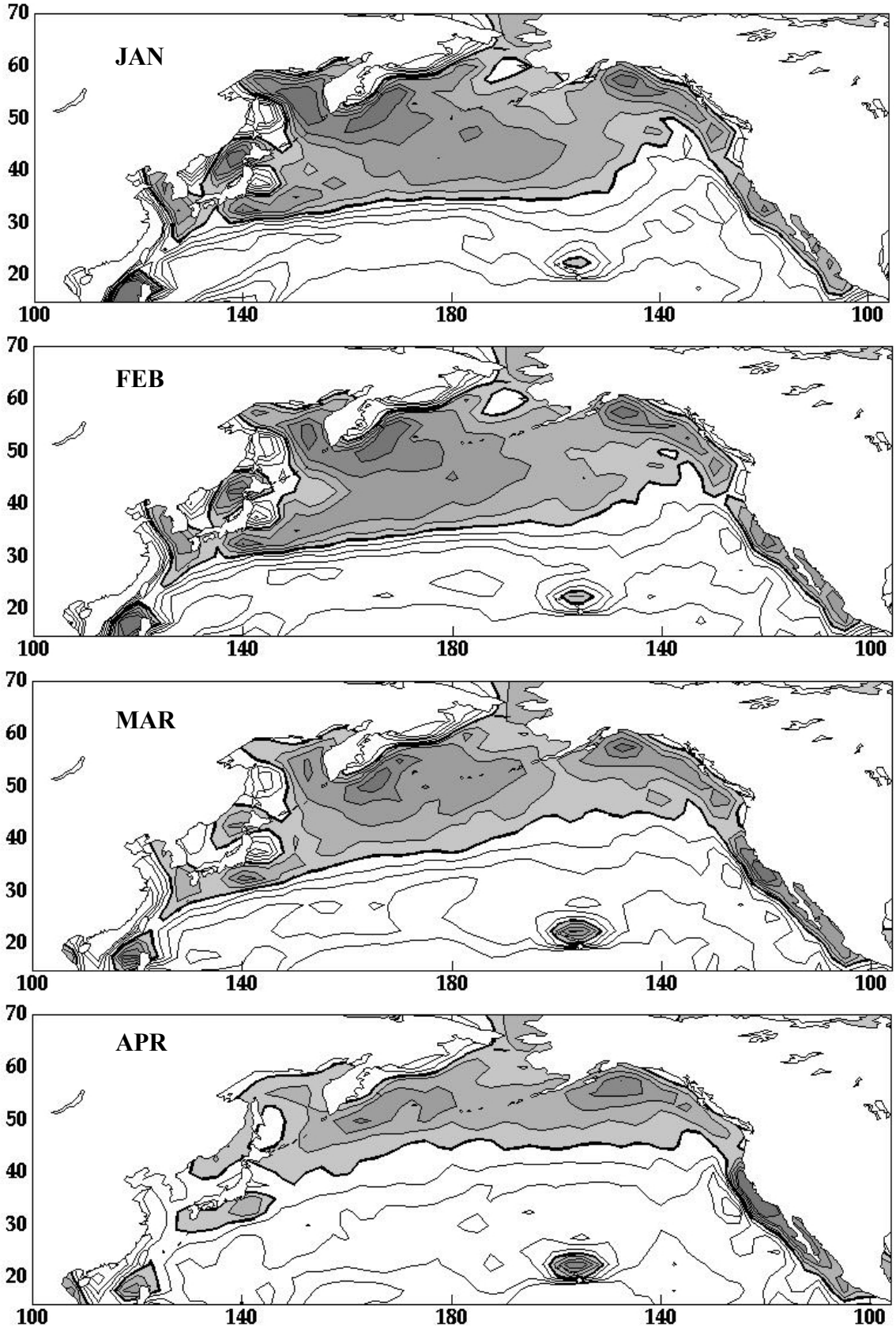
JAN
FEB
MAR
APR
70
60
50
40
30
20
100
140
180
140
100

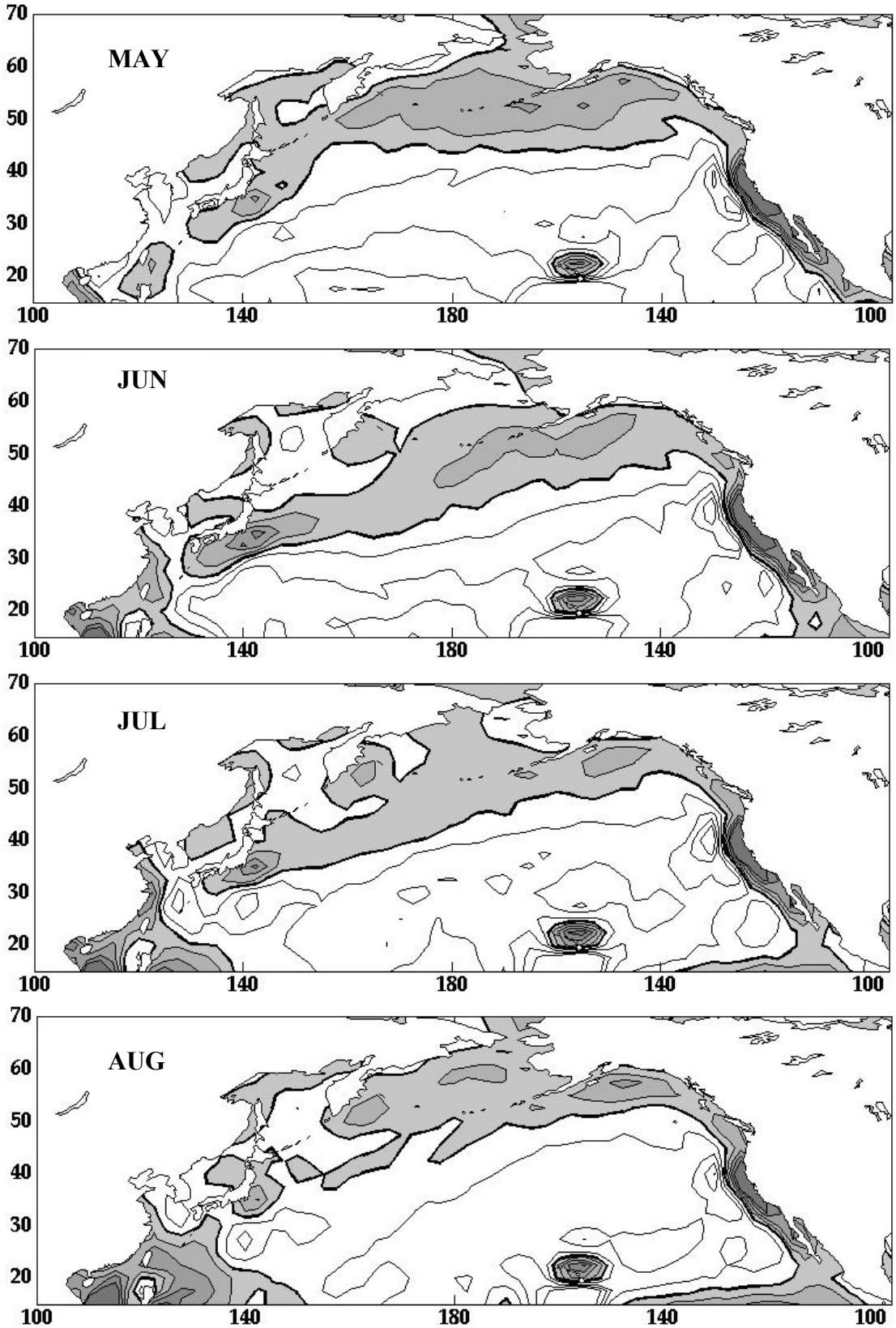
MAY
JUN
JUL
AUG
70
60
50
40
30
20
100
140
180
140
100

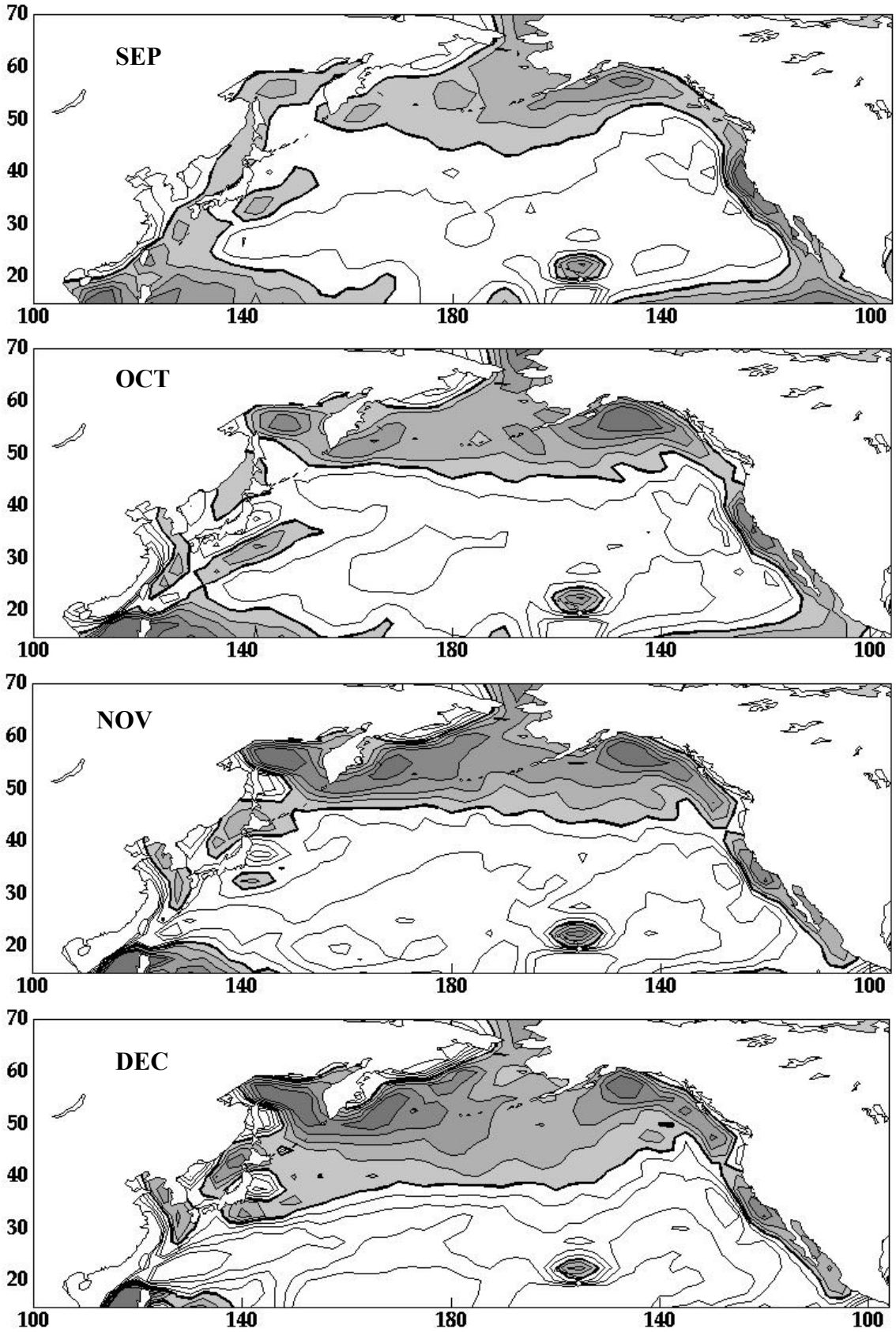
SEP
OCT
NOV
DEC
70
60
50
40
30
20
100
140
180
140
100

# APPENDIX G. SVERDRUP TRANSPORT MONTHLY MEANS

The data shown in this appendix are monthly means of Sverdrup transport values. The values were derived from monthly averaged wind stress values from the NCEP subset values of daily wind stress. Monthly mean fields are computed as the arithmetic mean of each month over the entire time series. The zero streamline is in bold. Streamline interval is 10 Sv (1 Sv $\equiv$ $10^6$ $m^3$ $s^{-1}$).

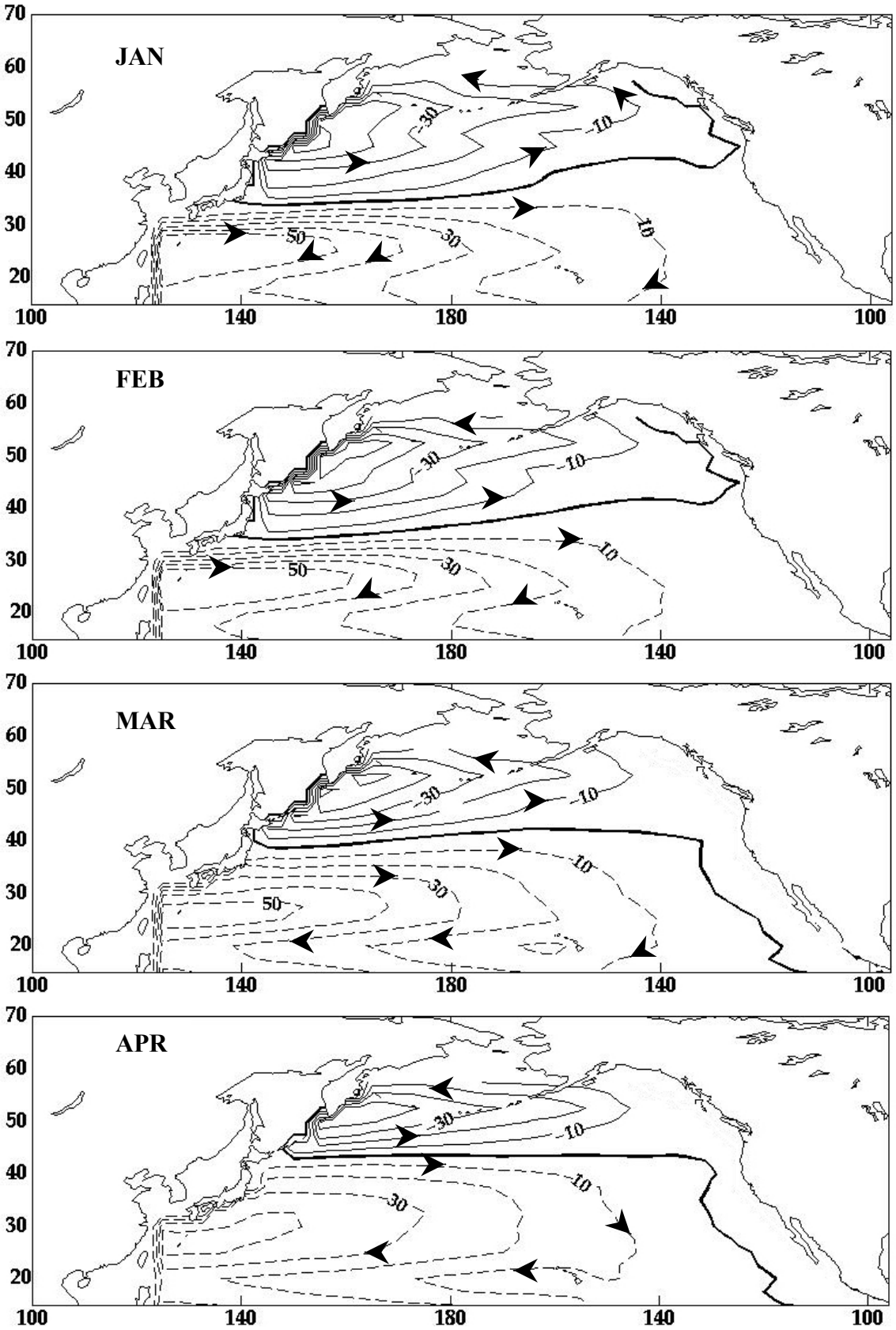
JAN
FEB
MAR
APR
70
60
50
40
30
20
100
140
180
140
100
30
10
50

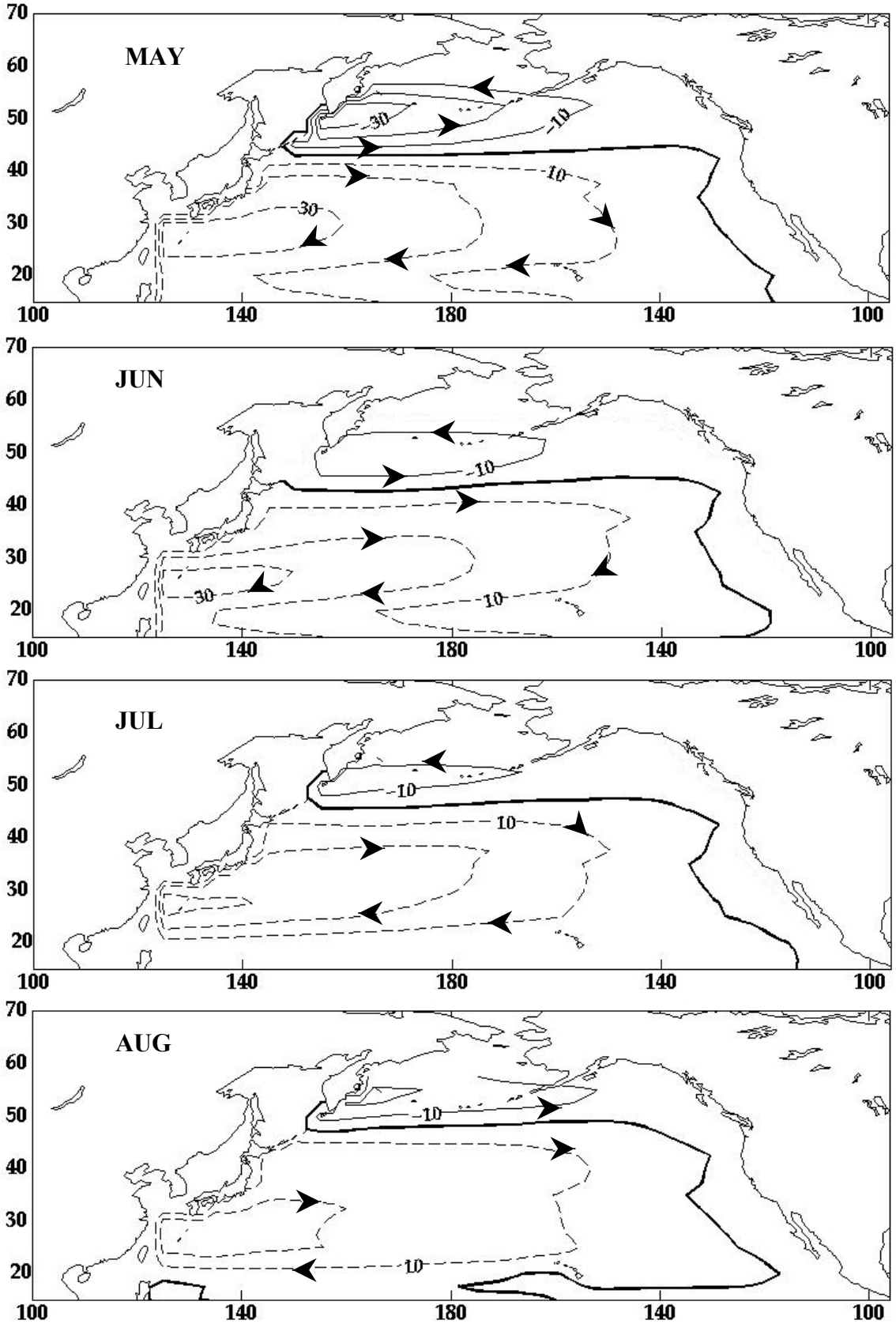
MAY
JUN
JUL
AUG
70
60
50
40
30
20
100
140
180
140
100
-30
-10
10
30

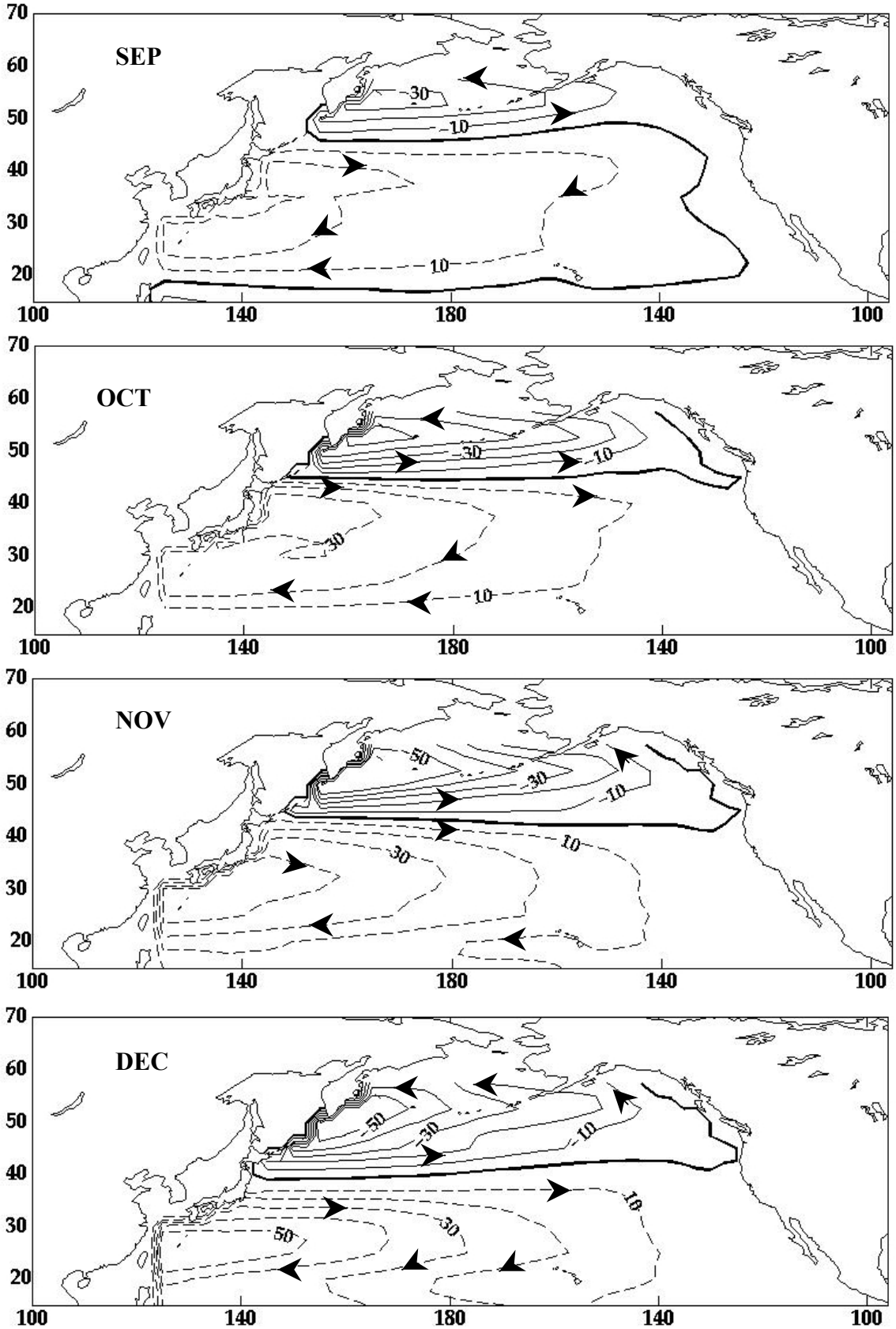
SEP
OCT
NOV
DEC
70
60
50
40
30
20
100
140
180
140
100
30
10
50

# APPENDIX H. COMPLEX EMPIRICAL ORTHOGONAL FUNCTION (EOF) MATLAB PROGRAM

```
% Wind Stress Vector Complex EOF calculation
%10/27/99
%-----------------------------------------------------------------------
%DEMEANING AND DETRENDING U&V INDIVIDUALLY THEN LEGLER

callstart   %clear all figures, variables

%-----------------------------------------------------------------------

%load u,v component monthly matrices (29,73,624)
%52 years of monthly averaged u (tau_x.mat) and v (tau_y.mat)(624)
%2.5 degree grid (29,73)

load tau_x.mat
load tau_y.mat

%-----------------------------------------------------------------------
%create empty matrix
      new_tau_x = zeros([23 73 624]);
      new_tau_y = zeros([23 73 624]);

%trim data from 0-70N to 15-70N
for n=1:624
  new_tau_x(:,:,n) = tau_x(1:23,:,n);
  new_tau_y(:,:,n) = tau_y(1:23,:,n);
  n
end
%-----------------------------------------------------------------------
%DETREND, DEMEAN U,V COMPONENTS
%create empty matrix
      transpose_tau_x = zeros([73 23 624]);
      transpose_tau_y = zeros([73 23 624]);
      reshape_tau_x     = zeros([624 1679]);
      reshape_tau_y     = zeros([624 1679]);

for n = 1:624
  transpose_tau_x(:,:,n) = transpose(new_tau_x(:,:,n));
      %TRANSPOSE
  transpose_tau_y(:,:,n) = transpose(new_tau_y(:,:,n));
      %TRANSPOSE
  reshape_tau_x(n,:)   =   reshape(transpose_tau_x(:,:,n),   1,   1679);
      %RESHAPE
  reshape_tau_y(n,:)   =   reshape(transpose_tau_y(:,:,n),   1,   1679);
%RESHAPE
end
%-----------------------------------------------------------------------
%create empty matrix
      dmn_reshape_x   = zeros([624 1679]);
      dmn_reshape_y   = zeros([624 1679]);
      dt_dmn_rs_x       = zeros([624 1679]);
      dt_dmn_rs_y       = zeros([624 1679]);
```

```
%-----------------------------------------------------------------------

%demean,detrend the position thru time
for n = 1:1679
  dmn_reshape_x(:,n) = reshape_tau_x(:,n)-mean(reshape_tau_x(:,n));
  dmn_reshape_y(:,n) = reshape_tau_y(:,n)-mean(reshape_tau_y(:,n));
  dt_dmn_rs_x(:,n) = detrend(dmn_reshape_x(:,n));
  dt_dmn_rs_y(:,n) = detrend(dmn_reshape_y(:,n));
n
end%
-----------------------------------------------------------------------
%create empty matrix
      rs_x        = zeros([73 23 624]);
      rs_y        = zeros([73 23 624]);
      new_x = zeros([23 73 624]);
      new_y = zeros([23 73 624]);

%unwrap   and   restore   to   original   matrix   now   that   it   is
detrended/demeaned
      for n = 1:624
      rs_x(:,:,n) = reshape(dt_dmn_rs_x(n,:), 73,23);
      rs_y(:,:,n) = reshape(dt_dmn_rs_y(n,:), 73,23);
      new_x(:,:,n) = transpose(rs_x(:,:,n));
      new_y(:,:,n) = transpose(rs_y(:,:,n));
      end

%FINISH (DETREND, DEMEAN U,V COMPONENTS)
%-----------------------------------------------------------------------
%make v complex
%-----------------------------------------------------------------------
%create empty matrix
      complex_tau_y = zeros([23 73 624]);

      for n=1:624
      complex_tau_y(:,:,n) = new_y(:,:,n)*1i;
      str=num2str(n);
      disp(['i ', str])
      end

%-----------------------------------------------------------------------
%add u+iv
%-----------------------------------------------------------------------
%create empty matrix
      complex_vector = zeros([23 73 624]);

      for n=1:624
      complex_vector(:,:,n) = complex_tau_y(:,:,n) + new_x(:,:,n);
      str=num2str(n);
      disp(['vector ', str])
      end
```

```
%-----------------------------------------------------------------------
% RESHAPE DATA FOR EOF ANALYSIS
%-----------------------------------------------------------------------
%create empty matrix
      transpose_cv = zeros([73 23 624]);
      reshape_cv = zeros([624 1679]);
      tr_reshape_cv = zeros([1679 624]);

%reshape
      for n = 1:624
      transpose_cv(:,:,n) = (complex_vector(:,:,n).');
%23x73x624->73x23x624
      reshape_cv(n,:) = reshape(transpose_cv(:,:,n), 1, 1679);
%73x23x624->624x1679
      tr_reshape_cv(:,n) = (reshape_cv(n,:).');
%624x1679 ->1679x624
      str=num2str(n);
      disp(['reshape ', str])
      end


%-----------------------------------------------------------------------
%create empty matrix for variance/covariance matrix
      H = zeros([1679 1679]);
      H(:,:) = ( (tr_reshape_cv*tr_reshape_cv')/624 );
%-----------------------------------------------------------------------
% EIG    Eigenvalues and eigenvectors.
%    E = EIG(X) is a vector containing the eigenvalues of a square
%    matrix X.

%    [V,D] = EIG(X) produces a diagonal matrix D of eigenvalues and a
%    full matrix V whose columns are the corresponding eigenvectors so
%    that X*V = V*D.

%-----------------------------------------------------------------------
%create the empty matrix for V and D
V = zeros([1679 1679]);
D = zeros([1679 1679]);
 [V,D] = eig(H);
%-----------------------------------------------------------------------
%create the empty matrix for the coefficients (PCs)
      C=zeros(1679,624);
%get the coefficients of the eigenvector for each pc of month m
% (so col 1 contains all the coefficients of eigenvector 1 (1679)etc.)

for m=1:624
  for n=1:1679
    C(n,m)=V(:,n)'*tr_reshape_cv(:,m);
  end %n
end   %m
%-----------------------------------------------------------------------
% PC(k) time series     k=1:1679
% PC1 = C1  Complex in the form a+ib

C1=C(1,:);
C1_1=real(C1);    %primary component
```

```
C1_2=imag(C1);    %secondary component

            % PC2 = C2  Complex in the form a+ib

            C2=C(2,:);
            C2_1=real(C1);    %primary component
            C2_2=imag(C1);    %secondary component
%Etc… … …
%-----------------------------------------------------------------------
%PLOT PC1 time series (PC1 for 624 months)
plot(1:624, C1_1, '-*k')
%-----------------------------------------------------------------------
%calculate phase time series
%create empty matrix
      phase_ts = zeros([624 1]);                      %1679x1679

      for n=1:624
      phase_ts(n) = [atan2( (imag(C(1,n))),(real(C(1,n))) )];
      deg_phase_ts(n) = rad2deg(phase_ts(n));
      end
%-----------------------------------------------------------------------
%calculate weighting factor time series
%create empty matrix
      weight_ts = zeros([624 1]);                     %1679x1679

for n=1:624
weight_ts(n)=[sqrt((real(C(1,n))*real(C(1,n)))+(imag(C(1,n))*imag(C(1,n
)) ))];
end
%-----------------------------------------------------------------------
% create the 1st eigenvector field
      V(:,1679);
      uV1=real(V(:,1));
      vV1=imag(V(:,1));

      tr_uV1 = uV1';
      rs_uV1 = reshape(tr_uV1,73,23);
      tr_rs_uV1 = rs_uV1';

      tr_vV1 = vV1';
      rs_vV1 = reshape(tr_vV1,73,23);
      tr_rs_vV1 = rs_vV1';
%-----------------------------------------------------------------------
%PLOT Eigenvector
%-----------------------------------------------------------------------
hold on
quiver(lonValues(1:2:73),        latValues,        tr_rs_uV1(:,1:2:73),
tr_rs_vV1(:,1:2:73))
```

```
%-----------------------------------------------------------------------
%variance calculation
      var=zeros(1679,1);
      var=real(diag(D))
      pc1var = (var(1)/(trace(H)))*100
      pc2var = (var(2)/(trace(H)))*100
      pc3var = (var(3)/(trace(H)))*100
      pc4var = (var(4)/(trace(H)))*100
      pc5var = (var(5)/(trace(H)))*100
      pc6var = (var(6)/(trace(H)))*100
%etc……
%-----------------------------------------------------------------------
```

# LIST OF REFERENCES


Bakun, A., and C. S. Nelson, 1991: The seasonal cycle of wind-stress curl in subtropical eastern boundary current regions. *J. Phys. Oceanogr*., **21**, 1815-1834.

Barnett, T. P., 1977: The principal time and space scales of the Pacific trade wind fields. *J. Atmos. Sci*, **34**, 221-236.

Beamish, R.J. and Bouillon, D. R., 1993: Pacific salmon production trends in relation to climate. *Can. J. Fish. Aquat. Sci*, **50**, 2270-2291.

Brodeur, R. D. and Ware, D. M., 1992: Long-term variability in zooplankton biomass in the subarctic Pacific Ocean. *Fish. Oceanogr*., **1**, 32-38.

Bryden, H. L., D. H. Roemmich, and J. A. Church, 1991: Ocean heat transport across 24°N in the Pacific. *Deep-Sea Res*., **38**, 297-324.

Cattell, R. B., 1966. The scree test for the number of factors. J. Multiv. Behav. Res. **1**, 245-276.

Chelton, D. B., and Davis, R. E., 1982: Monthly mean sea level variability along the western coast of North America. *J. Phys. Oceanogr*. **12**, 757-784.

Chelton, D. B., A. M. Mestas-Nuñez and M.H. Freilich, 1990: Global wind stress and Sverdrup circlation from the Seasat Scatterometer. *J. Phys. Oceanogr*., **20**, 1175-1205.

Craddock, J. M. and C. R. Flood, 1969: Eigenvectors for representing the 500 mb geopotential surface over the Northern Hemisphere. *Q .J .R. Met. Soc.* **95**, 576-593.

Ekman, V. W., 1905: On the influence of the earth's rotation on ocean currents, *Ark. Mat. Aston. Fys.,* ***2*(11)**, 1-53.

Hardy, D. M., and J .J. Walton, 1978: Principal components analysis of vector wind measurements. *J. Appl. Meteorol*., **17**, 1153-1162.

Hare, S. R., 1996: Low frequency climate variability and salmon production. Ph.D. dissertation, Univ. of Washington.

Harrison, D. E., 1989: On climatological monthly mean wind stress and wind stress curl fields over the World Ocean. *J. Climate*, **2**, 57-70.

Hautala, S. L., D. Roemmich and W. J. Schmitz, Jr., 1994. Is the North Pacific in Sverdrup balance along 24°N? *J. Geophys. Res.,* **99**: 16,041-16,052.

Hellerman, S., and M. Roesnstein, 1983: Normal monthly wind stress over the world ocean with error estimates. *J. Phys. Oceanogr*., **17**, 1093-1104.

Kalnay, E., M. Kanamitsu, R. Kistler, W. Collins, D. Deaven, L. Gandin, M. Iredell, S. Saha, G. White, J. Woollen, Y. Zhu, A. Leetmaa, R. Reynolds, M. Chelliah, W. Ebisuzaki, W. Higgins, J. Janowiak, K.C. Mo, C. Ropelewski, J. Wang, R. Jenne, D. Joseph, 1996: The NCEP/NCAR 40-Year Reanalysis Project. *Bull. Amer. Met. Soc*., March, 1996.

Kawabe, M., 1995: Variations of current path, velocity, and volume transport of the Kuroshio in relation with the large meander. *J. Phys. Oceanogr*., **25**, 3103-3117.

Kutsuwada, K., 1988: Interannual correlations between sea level difference at the south coast of Japan and wind stress over the North Pacific. *J. Oceanogr. Soc. Japan*, **44**, 68–80.

Kutzbach, J. E., 1967: Empirical eigenvectors of sea-level pressure, surface temperature and precipitation complexes over North America. *J. Appl. Meteorol*., **6**, 791-802.

Large, W., and S. Pond, 1981: Open Ocean momentum flux measurements in moderate to strong winds. *J. Phys. Oceanogr.,* **11**, 324-336.

Legler, D. M., 1983: Empirical Orthogonal Function Analysis of wind vectors over the tropical Pacific region. *Bull. Of the Am. Met. Soc.,* **64**, No. 3, 234-241.

Mizoguchi, K., S. D. Meyers, S. Basu, J. J. O'Brien, 1999: Multi- and quasi-decadal variations of sea surface temperature in the North Atlantic. *J. Phys. Oceanogr.,* **29**, 3133-3144.

Munk, W. H., 1950: On the wind-driven ocean circulation. *J. Meteorol.*, **7(2)**, 79-93.

Parrish, R. H., F. B. Schwing and R. Mendelssohn, 2000: Mid-latitude wind stress: the energy source for climatic shifts in the North Pacific Ocean. *Fish. Oceanogr*., **9**, 3,234-238.

Pedlosky, J., 1987: *Geophysical Fluid Dynamics.* Springer-Verlag, 710 pp.

Qiu, B. and T. M. Joyce, 1992: Interannual variability in the mid- and low-latitude western North Pacific. *J. Phys. Oceanogr.*, **22** 1062-1079.

Schwing, F. B., T. Murphree, and P. M. Green. 2002. The Northern Oscillation Index (NOI): A New Climate Index for the Northeast Pacific. *Prog. Oceanogr*., in press.

Sekine, Y. and K. Kutsuwada, 1994: A numerical experiment for the seasonal variation in volume transport of the Kuroshio south of Japan, *J. Phys. Oceanogr.*, **24(2)**, 261-272.

Stommel, H., 1948: The westward intensification of wind-driven ocean currents. *Trans. Amer. Geophys. Union*, **29(2)**, 202-206.

Sverdrup, H. U., 1947: Wind-driven currents in a baroclinic ocean; with application to the equatorial currents of the eastern Pacific. *Proc. Natl Acad. Sci. USA*., **33**, 318-326.

Trenberth, K. E., & J. W. Hurrell, 1994. Decadal atmospheric-ocean variations in the Pacific. *Climate Dynamics,* **9**, 303-319.

Trenberth, K. E., W. G. Large and J. G. Olson, 1990: The mean annual cycle in global ocean wind stress. *J. Phys. Oceanogr., **11**, 324-336.*

Wolter, K., & M. S. Timlin, (1998). Measuring the strength of ENSO– how does 1997/98 rank? *Weather,* **53**, 315-324.

Wyrtki, K., and G. Meyers, 1976: The trade wind field over the Pacific Ocean. *J. Appl. Meteorol*., **15**, 698-704.

Xie, L., and W. W. Hsieh, 1995: The global distribution of wind-induced upwelling. *Fish. Oceanogr*., **4:1**, 52-67.

THIS PAGE INTENTIONALLY LEFT BLANK

# INITIAL DISTRIBUTION LIST

1. Defense Technical Information Center
   Ft. Belvoir, Virginia

2. Dudley Knox Library
   Naval Postgraduate School
   Monterey, California

3. Mary L. Batteen
   Naval Postgraduate School
   Monterey, California

4. Curtis A. Collins
   Naval Postgraduate School
   Monterey, California

5. Franklin B. Schwing
   National Oceanic and Atmospheric Administration
   Pacific Fisheries Environmental Laboratory
   Pacific Grove, California

6. Christopher S. Moore
   National Oceanic and Atmospheric Administration
   Santa Cruz Laboratory
   Santa Cruz, California

7. George W. Boehlert
   National Oceanic and Atmospheric Administration
   Pacific Fisheries Environmental Laboratory
   Pacific Grove, California

8. Churchill B. Grimes
   National Oceanic and Atmospheric Administration
   Santa Cruz Laboratory
   Santa Cruz, California

9. Elizabeth C. Norton
   National Oceanic and Atmospheric Administration
   Santa Cruz Laboratory
   Santa Cruz, California

10. Richard A. Neal
National Oceanic and Atmospheric Administration
Southwest Fisheries Science Center
La Jolla, California

11. Rear Admiral Evelyn J. Fields, NOAA
National Oceanic and Atmospheric Administration
Office of Marine and Aviation Operations
Silver Springs, Maryland

12. Captain David H. Peterson, NOAA
National Oceanic and Atmospheric Administration
Office of Marine and Aviation Operations
Silver Springs, Maryland

13. Maureen A. Moore
Virginia Beach, Virginia

14. Joe Moore
Virginia Beach, Virginia

15. Dave Husby
National Oceanic and Atmospheric Administration
Pacific Grove, California

16. Commander Gary. P. Bulmer
National Oceanic and Atmospheric Administration
Office of Marine and Aviation Operations
Silver Springs, Maryland

17. Steve Ralston
National Oceanic and Atmospheric Administration
Santa Cruz, California

18. Pete Adams
National Oceanic and Atmospheric Administration
Santa Cruz, California

19. Rachel Johnson
National Oceanic and Atmospheric Administration
Santa Cruz, California

20. Phaedra Green Jessen
National Oceanic and Atmospheric Administration
Pacific Grove, California

21. Jerry Norton
National Oceanic and Atmospheric Administration
Pacific Grove, California

22. Lieutenant Commander Mark Pickett
National Oceanic and Atmospheric Administration
Pacific Grove, California

23. Paul Jessen
Naval Postgraduate School
Monterey, California

24. Julie McClean
Naval Postgraduate School
Monterey, California

25. Kathleen Bonner
Fredericksburg, Virginia

26. Dr. Patrick Moore, M.D.
Seattle, Washington

27. Mark Ferris
Burgettstown, Pennsylvania

28. Erwin Willis
Rancho Santa Fe, California

29. Noelle Norton
San Diego, California

30. Carol McPhee
San Luis Obispo, California

31. Ann Fitzgerald
San Luis Obispo, California

32. Marcie Folsom
Inverness, California

33. David VenTresca
Monterey, California

34. Pete Zell
Half Moon Bay, California